



UCGE Reports

Number 20322

**Department of Geomatics Engineering**

**Enhanced GNSS Signal Detection Performance Utilizing  
Polarization Diversity**

(URL: <http://www.geomatics.ucalgary.ca/graduatetheses>)

**by**

**Mohammadreza Zaheri**

January 2011



UNIVERSITY OF CALGARY

Enhanced GNSS Signal Detection Performance Utilizing  
Polarization Diversity

by

Mohammadreza Zaheri

A THESIS

SUBMITTED TO THE FACULTY OF GRADUATE STUDIES  
IN PARTIAL FULFILMENT OF THE REQUIREMENTS FOR THE  
DEGREE OF MASTER OF SCIENCE

GEOMATICS DEPARTMENT

CALGARY, ALBERTA

DECEMBER, 2010

© Mohammadreza Zaheri 2010

## Abstract

The detection of GNSS signals in indoor environments is a challenging problem since the signals suffer from attenuation due to propagation through building materials, which induce attenuation of up to 30 dB or more. In addition, the interference between multiple reflected signals causes fluctuations in the received signal's amplitude and phase which result in spatial and temporal multipath fading. In order to overcome the difficulties of positioning under weak GPS signal conditions, such as urban and indoor environments, various approaches including High-Sensitivity GPS (HSGPS), assisted GPS (AGPS), the use of the modernised GPS signals, and combining a diverse array of antenna elements have being developed and investigated.

GPS signal polarization changes upon reflection from right hand circular polarization (RHCP) to elliptical polarization, formed from both right and left hand polarization. In this work, the polarization diversity of received signals is investigated and utilized to improve GPS signal detection performance in indoor environments. The design of the detection algorithm is based on target values of the probability of detection and probability of false alarm metrics associated with each search hypothesis. This leads to either the Estimator Correlator (EC) or Equal Gain Combiner (EG) structure. The performance of these structures is thoroughly analyzed theoretically under different signal conditions in indoor areas.

To examine the proposed method practically, a large number of data sets in various indoor locations are collected using a commercial dual polarization antenna mounted on a linear motion table to produce motion. The complex correlation coefficient

is obtained for various space vehicles. In addition, the empirical ROC curves are derived to analyze the performance of the proposed approach. Considerable enhancement in performance based on the new designed detector can be observed. Besides, in order to compare the performance of the polarization diversity with spatial diversity using these structures, GPS signals were collected in various indoor areas and the results are analyzed and inter-compared.

## **Acknowledgements**

Foremost, I would like to express my sincere gratitude to my supervisor Professor Gérard Lachapelle for the continuous support during my study and research, for his patience, motivation, and immense knowledge. His guidance helped me in all the time of research and writing of this thesis. I will always remember his positive attitude and understanding which helped me to shape my professional career.

Thanks to my co-supervisor, Dr. Ali Broumandan, for his friendship, sharing his insights and assisting me in the theoretical work of this thesis. This research would have been much more challenging without his endeavours and support. Besides, I would like to thank Dr. Cillian O’Driscoll as my co-supervisor in the initial period of my study for his kind support, patience and valuable advices.

Special thanks to Somaieh, my lovely wife, for her support and for her constant love during my education. She was the reason of my happiness and peace. Also, special thank to my parents without whose support and unconditional love I would never have gotten this far. This dissertation would have been simply impossible without them. Besides, I would like to thank my siblings for their kind support during my study.

I thank my friends and colleagues Pejman Kazemi, Vahid Dehghanian, Mohammad Haris Afzal, Richard Ong, Nima Sadrieh, Hatef Keshvadi, Behnam Aminian and the rest of PLAN group members for their kindness and helpful suggestions in technical issues.

## **Dedication**

To my beloved parents Mahdi and Maryam and my lovely wife, Somaieh, and my kind siblings.

## Table of Contents

Abstract .....	ii
Acknowledgements .....	iv
Dedication .....	v
Table of Contents .....	vi
List of Figures and Illustrations .....	x
List of Symbols .....	xiv
List of Abbreviations .....	xv
CHAPTER ONE: INTRODUCTION .....	1
1.1 Indoor GNSS signal detection challenges .....	1
1.1.1 Signal attenuation .....	1
1.1.2 Multipath interference and fading .....	3
1.1.3 Diversity system benefits .....	4
1.2 Limitation of previous works .....	5
1.3 Objectives and novel contributions .....	8
1.4 Thesis Outline .....	12
CHAPTER TWO: FADING CHANNELS AND DIVERSITY SYSTEMS .....	14
2.1 Small-Scale Fading channel .....	14
2.1.1 Parameters of mobile multipath channel .....	15
2.1.1.1 Time dispersion Parameters .....	15
2.1.1.2 Coherence Bandwidth .....	16
2.1.1.3 Doppler spread .....	17
2.1.1.4 Coherence time .....	17
2.1.2 Types of signal fading .....	18
2.1.2.1 Flat fading due to multipath time delay spread .....	18
2.1.2.2 Frequency selective fading due to multipath time delay spread .....	19
2.1.2.3 Fast and slow fading due to Doppler spread .....	19
2.2 Diversity systems .....	19
2.2.1 Spatial diversity .....	22
2.2.2 Polarization diversity .....	23
2.3 GPS signal model .....	25
2.3.1 GPS signal architecture .....	25
2.3.2 Baseband signal processing .....	25
2.3.3 Single antenna signal detection procedure .....	27
2.4 Combining methods .....	28
2.4.1 Selection combining .....	29
2.4.2 Maximum ratio combining .....	30
2.4.3 Likelihood ratio test (LRT) .....	33
2.5 Signal distribution description .....	35
2.5.1 Gaussian distribution .....	35
2.5.2 Rayleigh distribution .....	36

2.5.3 Rician Distribution .....	37
2.5.4 Chi-squared distribution .....	39
2.6 Summary .....	41
<b>CHAPTER THREE: GPS SIGNAL POLARIZATION .....</b>	<b>42</b>
3.1 Electromagnetic wave polarization.....	42
3.2 Polarization mismatch loss .....	45
3.2.1 Circular antenna polarization mismatch loss.....	46
3.2.2 Linear antenna polarization mismatch loss .....	49
3.3 Indoor signal model .....	52
3.3.1 GNSS signal polarization analysis in multipath environments .....	52
3.3.2 Characterizing fading channel .....	54
3.4 Summary .....	56
<b>CHAPTER FOUR: DIVERSITY SYSTEMS PERFORMANCE EVALUATION.....</b>	<b>57</b>
4.1 Likelihood ratio test (LRT) function .....	57
4.2 Diversity gain.....	60
4.3 Two antenna detection procedure .....	61
4.3.1 Performance evaluation .....	64
4.4 Theoretical analysis of indoor environment .....	67
4.4.1 Single Antenna .....	67
4.4.2 Uncorrelated equal power signals .....	69
4.4.3 Correlated equal power signals .....	71
respectively, where .....	72
4.4.3.1 Comparison of estimator correlator and equal gain combiner.....	75
4.4.4 Uncorrelated and unequal power inputs .....	79
4.4.5 Correlated unequal power inputs.....	83
4.5 Summary.....	87
<b>CHAPTER FIVE: TEST SETUP AND EXPERIMENTAL RESULTS.....</b>	<b>89</b>
5.1 Circular polarization diversity .....	89
5.1.1 Test Setup .....	89
5.1.2 Coherent integration time selection.....	97
5.1.2.1 Channel coherence time.....	97
5.1.2.2 Channel phase rate .....	97
5.1.3 Developed software .....	99
5.1.4 Results .....	101
5.1.4.1 Channel Measurement: .....	101
5.1.4.2 Correlation Coefficient .....	103
5.1.4.3 Empirical ROC curve.....	106
5.1.4.4 Fading mitigation .....	109
5.1.4.5 LCR and AFD analysis .....	110
5.1.4.6 Diversity Gain.....	114
5.2 Comparison of polarization and spatial diversity .....	115

5.2.1 Test setup.....	115
5.2.2 Experimental results .....	120
5.2.2.1 Channel Measurement .....	120
5.2.2.2 Correlation Coefficient .....	122
5.2.2.3 Average input SNR:.....	123
5.2.2.4 Detection performance.....	125
5.2.2.5 LCR and AFD analysis .....	127
5.2.2.6 Diversity Gain.....	128
5.3 Summary.....	129
<b>CHAPTER SIX: CONCLUSION AND FUTURE WORKS .....</b>	<b>131</b>
6.1 Conclusions.....	131
6.2 Limitations and future works.....	133
6.2.1 More analysis under various wireless channel assumptions .....	133
6.2.2 Combining with other diversity structures .....	134
6.2.3 Implementation of the diversity system in parameter estimation level .....	134
<b>REFERENCES .....</b>	<b>135</b>

## List of Tables

Table 5.1: Data sets and selected vehicle satellites for each set .....	96
Table 5.2: $K$ factor measurements for received signals in different indoor environments.....	103
Table 5.3: Measured correlation coefficient between received signals .....	105
Table 5.4: Probability of detection for a specific probability of false alarm (0.01) .....	108
Table 5.5: Data sets and selected satellites .....	116
Table 5.6: $K$ factors for received signals in indoor situation.....	122

## List of Figures and Illustrations

Figure 2.1: SNR of two independent antennas experiencing deep fades.....	21
Figure 2.2: Antenna Diversity Scheme.....	21
Figure 2.3: Spatial correlation coefficient for various angle of spread.....	23
Figure 2.4: GPS signal Doppler removal and code correlation .....	27
Figure 2.5: Despreading procedure to estimate the navigation data.....	28
Figure 2.6: Selection combining scheme .....	29
Figure 2.7: Maximum ratio combining method.....	30
Figure 2.8: SNR cumulative distribution function of maximum ratio combining.....	32
Figure 2.9: LRT function schematic .....	35
Figure 2.10 Rayleigh probability distribution function .....	37
Figure 2.11: Rician distributions for various $K$ factors (Blaunstein & Andersen 2002) ..	39
Figure 3.1: Different signal polarization schemes: (a) elliptical polarization (b) circular polarization (c) linear polarization.....	44
Figure 3.2: (a) Right-Hand Circularly Polarized (RHCP) signal (b) Left-Hand Circularly Polarized (LHCP) signals .....	44
Figure 3.3: Projection of an RHCP signal on antenna surface .....	46
Figure 3.4: RHCP and LHCP signal loss received by an RHCP antenna .....	48
Figure 3.5: Receiving an elliptical wave by a linear antenna .....	49
Figure 3.6: Total loss in receiving RHCP wave by a linear antenna for $\varphi = 0^\circ$ .....	51
Figure 3.7: Total loss in receiving RHCP wave by a linear antenna for $\theta = 60^\circ$ .....	51
Figure 3.8: Total loss in receiving RHCP wave by s linear antenna for $\theta = 30^\circ$ .....	51
Figure 3.9: Incoming EM signal to a reflector.....	52
Figure 3.10: GNSS signal polarization after reflection (Yang & Porter 2005) .....	53

Figure 3.11: Cumulative probability of received signals and fitted Rician and Rayleigh distributions .....	55
Figure 4.1: Binary hypothesis probabilities .....	59
Figure 4.2: ROC curve for two types of detector.....	59
Figure 4.3: LRT detector scheme for two antennas .....	64
Figure 4.4: Equal gain (EG) combiner scheme.....	70
Figure 4.5: Estimator correlator probability of detection as a function of input SNR and signal cross correlation coefficient ( $P_{FA}=0.01$ ) .....	73
Figure 4.6: Estimator correlator diversity gain as a function of probability of detection and cross correlation coefficient between input signals ( $P_{FA}=0.01$ ) .....	73
Figure 4.7: ROC curves for EC and EG with a correlated input signals, SNR = 10 dB ..	76
Figure 4.8: Probability of detection difference between EG and EC combiners for uncorrelated inputs ( $P_{FA}=0.001$ ).....	76
Figure 4.9: Required input SNR vs. probability of detection for $P_{FA}=0.001$ .....	77
Figure 4.10: Diversity gain versus correlation coefficient for $P_{FA}=0.01$ .....	78
Figure 4.11: Diversity gain difference of EG and EC ( $P_{FA}=0.01$ ).....	78
Figure 4.12: Combining two unequal power input signals .....	79
Figure 4.13: Probability of detection for unequal power and uncorrelated inputs .....	81
Figure 4.14: Diversity gain for unequal power and uncorrelated inputs .....	81
Figure 4.15: EC and EG diversity gain difference for unequal power and uncorrelated inputs.....	83
Figure 4.16: The probability of detection for a fixed probability of false alarm ( $P_{FA} = 0.01$ ) for the general condition.....	85
Figure 4.17: The diversity gain for the general condition as a function of signals cross correlation coefficient and input power difference .....	86
Figure 4.18: EC and EG diversity gain difference for the general condition as a function of signal cross correlation coefficient and input power difference.....	87

Figure 5.1: Antenna and associated hardware used in the data collections .....	90
Figure 5.2: Dual polarized antenna mounted on the linear motion table in NavLab, CCIT building .....	91
Figure 5.3: Corresponding sky plot for the data set collected on 19 January 2009 .....	92
Figure 5.4: Room 326 in CCIT building .....	93
Figure 5.5: Sky plots for collected data on 6 March 2009 .....	93
Figure 5.6: Energy High Bay in CCIT building, University of Calgary .....	94
Figure 5.7: MacEwan Hall in University of Calgary .....	94
Figure 5.8: Sky plots for data sets 4 .....	95
Figure 5.9: Sky plots for data sets 5 .....	95
Figure 5.10: Post-SNR output in a diversity system .....	96
Figure 5.11: The instantaneous frequency PDF for GPS L1 frequency and an antenna speed of 2.5 cm/s .....	99
Figure 5.12: Correlator output under $H_1$ and $H_0$ conditions .....	100
Figure 5.13: Cumulative probability of received signals and fitted Rician Rayleigh distribution .....	102
Figure 5.14: Empirical ROC curves for two selected satellites: (a) PRN 23 from data set 4 (b) PRN 32 from data set 2 .....	107
Figure 5.15: Probability of detection for a specific design point ( $P_{FA}=0.01$ ) .....	108
Figure 5.16: Signal fading mitigation at the output of EG combiner .....	110
Figure 5.17: An example for illustration of definition of LCR and AFD .....	111
Figure 5.18: The LCR for PRN 22, set 1 .....	112
Figure 5.19: The AFD for PRN 22, set 1 .....	113
Figure 5.20: AFD and LCR for all satellites for a threshold of 10 dB less than each signal rms .....	113
Figure 5.21: Diversity gain of proposed circular polarization diversity system .....	114

Figure 5.22: Antenna mounts on linear moving table.....	117
Figure 5.23: Energy High Bay, CCIT building, University of Calgary.....	118
Figure 5.24: ICT corridor, spatial diversity structure .....	118
Figure 5.25: Test sky plots - Polarization versus spatial diversity comparison.....	120
Figure 5.26: Cumulative probability of received signals and fitted Rician Rayleigh distribution .....	121
Figure 5.27: Correlation coefficients between received signals .....	123
Figure 5.28: Average input SNR .....	125
Figure 5.29: Probability of detection for various diversity schemes in $P_{FA}=0.01$ .....	126
Figure 5.30: LCR analysis for -10 dB lower than signal rms .....	127
Figure 5.31: AFD analysis for -10 dB lower than signal rms .....	128
Figure 5.32: Diversity gain for various diversity schemes .....	129

## List of Symbols

$\bar{\tau}$	Mean excess delay
$\sigma_{\tau}$	Delay spread
$B_D$	Doppler spread
$B_C$	Coherence Bandwidth
$T_c$	Coherence time for channel
$T_s$	Coherence time for signal
$\chi_v^2$	Chi-squared distribution with $v$ degrees of freedom
$\lambda$	Carrier wavelength
$\Psi_B$	Brewster angle
$\theta_g$	grazing angle
$x_I$	In-phase component of signal
$x_Q$	Quadrature component of signal
$x_e$	Envelope of received signal
$\Theta$	Average input SNR
$K$	K factor
$p(x)$	Probability function
$p(x, H_i)$	Probability function of $x$ under $H_i$ condition
$Pr(H_i; H_j)$	The probability of deciding $H_i$ while $H_j$ is true
$P_{FA}$	Probability of false alarm
$P_D$	Probability of detection
$\gamma$	Threshold in LRT detector
$C_s$	Signal covariance matrix
$C_w$	Additive noise covariance matrix
$\sigma_w^2$	Additive noise variance
$\sigma_s^2$	Signal variance
$E(\bullet)$	Expected value operator
$V$	Modal matrix
$\lambda_s$	Signal covariance matrix eigenvalue
$\mathbf{E}$	Electric field intensity vector
$E_h$	Horizontal component of electric field intensity vector
$E_v$	Vertical component of electric field intensity vector
$\hat{\rho}_a$	Antenna unit vector
$\hat{\rho}_w$	Wave unit vector

## List of Abbreviations

ADC	Digital to Analog Converter
AFD	Average Fade Duration
AGPS	Assisted GPS
AoA	Angle Of Arrival
BPSK	Binary Phase Shift Keying
C/A	Coarse/Acquisition
C/No	Carrier-to-Noise Ratio
CCW	Counter Clockwise
CDF	Cumulative Distribution Function
CDMA	Code Division Multiple Access
CL	Civilian Long
CM	Civilian Moderate
CN	Circular Normal
CP	Circular Polarization
CW	Clockwise
DOF	Degree Of Freedom
DS-CDMA	Direct Sequence-Code Division Multiple Access
EC	Estimator Correlator
EG	Equal Gain
EM	Electromagnetic Wave
erf	Error Function
FFT	Fast Fourier Transform
GNSS	Global Navigation Satellite System
GPS	Global Positioning System
HSGPS	High-Sensitivity GPS
IID	Independent and Identically Distributed
ISI	Inter-Symbol Interference
LCR	Level Crossing Rate
LHCP	Left Hand Circular Polarized
LHEP	Left Hand Elliptically Polarized
LOS	Line Of Sight
LRT	Likelihood Ratio Test
MMSE	Minimum Mean Square Error
NCCD	Non-Coherent Combining Detector
NP	Neyman-Pearson
PDF	Probability Distribution Function
PLF	Polarization Loss Factor
PRN	Pseudo-Random Noise
PSNR	Post-correlation SNR
rms	root mean squared
RF	Radio Frequency

RHCP	Right Hand Circular Polarized
RHEP	Right Hand Elliptically Polarized
ROC	Receiver Operating Characteristics
SNR	Signal-to-Noise Ratio
TOA	Time Of Arrival

## **Chapter One: Introduction**

Since the Global Positioning System (GPS) became fully operational in 1995, it has been widely used to aid localization and navigation worldwide with accuracy ranging from metre to centimetre given the condition, measurements, and adopted methods.

The detection of GNSS signals in indoor environments is a challenging problem since the signal suffers from attenuation and fading due to propagation through building materials including attenuation up to 30 dB, or even more, on the line of sight (LOS) signals. The amount of signal attenuation depends on the signal frequency, obstacle materials and even the angle of incidence. In addition, the interference between multiple reflected signals causes fluctuations in the received signal's amplitude and phase which results in spatial and temporal multipath fading. This thesis proposes techniques to deal with the problem of multipath fading in indoor GNSS applications. The main tenet of the fading mitigation is established based on utilizing diversity systems. In particular polarization diversity is being investigated thoroughly herein.

This chapter introduces the topic, provides a review of work done in this area, describes the specific objectives and tasks to be accomplished, and presents an outline of the thesis.

### **1.1 Indoor GNSS signal detection challenges**

#### ***1.1.1 Signal attenuation***

The nominal L1 civilian GPS signal strength under open sky condition is about -130 dBm. Under normal conditions, the thermal noise at room temperature in a bandwidth of 2 MHz is about -111 dBm. Hence, the equivalent signal-to-noise ratio (SNR) is approximately -19 dB measured at the surface of the Earth (Misra & Enge

2006). Another common way to quantify the signal power is Carrier-to-Noise Ratio ( $C/N_0$ ), which is referenced to 1 Hz bandwidth. In this case, the thermal noise power becomes -174 dBm-Hz. Hence, the  $C/N_0$  value in nominal outdoor environments becomes 44 dB-Hz. Although the GPS signal can be easily processed using common receivers at such signal strength, propagation of radio waves in urban and indoor areas results in signal deviation due to diffraction, reflection and refraction by the obstacles. In indoor environments the signal attenuates more due to penetration losses by building construction materials (Hu 2006).

Horikoshi et al (1986) have measured the penetration losses of a concrete wall or floor for 1.2 GHz band radiowave where 8.5-10 dB attenuation per each wall or floor occurs. In addition, they have investigated the propagation losses through different types of windows and frames in terms of angle of arrival. They have concluded that the signal attenuation increases almost linearly by increasing the angle of arrival defined as the departure angle from the perpendicular direction and it can reach up to 36.6 dB in case of parallel propagation direction to the window surface.

Signal frequency is another crucial factor in signal attenuation and deviation. Stavrou & Saunders (2003) reported that penetration losses increase as the frequency increases. In addition, Aguirre et al (1994) examine the penetration losses for radiowaves conducted at 912, 1920 and 5990 MHz and conclude that higher frequencies lead to higher penetration loss. In contrast, Tanis & Pailato (1993) examine the penetration characteristics of 880 MHz and 1922 MHz wave using four buildings with different characteristics. According to their results, the average shadowing loss at 1922 MHz is less than at 880 MHz.

Klukas et al (2004) focus on the building material effect on the GPS L1 signal attenuation, with a frequency of 1.575 GHz, using a GPS pseudo-satellite transmitter. They examine walls made of plywood, gyprock and cinder blocks leading to 0.5 dB, 2.4 dB and 23 dB attenuation, respectively. Moreover, they show this attenuation results in up to a few metres error in range derived from pseudorange.

### ***1.1.2 Multipath interference and fading***

In a multipath GNSS propagation channel, an electromagnetic wave passes through different paths and thus a receiver obtains the reflected signals with different time delays. At the receiver side, arrived signals are combined vectorially at any given frequency and this leads to a random variation in the received signal amplitude called fading effect which is characterized by the distribution of phases among incoming component waves (Blaunstein & Andersen 2002).

The signal level variation in multipath environments causes three sorts of attenuation and fading (Blaunstein & Andersen 2002). The first one is the path loss as the overall attenuation in signal power density due to propagating in the space. The second one is shadowing or slow fading which results in slow random variation in signal amplitude caused by diffractions, scattering and multiple reflections. The third one is known as fast fading which is caused by the mutual interference of the incoming wave components. According to the spatial scale of the fading, the slow and fast fading are known as large-scale and small-scale fading since they result in up to tens of wavelengths and a few wavelength fading, respectively.

The small-scale fading is categorized as various types of fadings based on the channel properties and signal characteristics such as flat fading and frequency selective

fading (Rappaport 2002). The flat fading results from the received signal amplitude variation over time due to fluctuation in the gain of the channel by multipath and leads to deep fading in the received signal amplitude.

In reality, especially in the case of a handheld GPS receiver used in urban or indoor areas, the signal encounters the dynamic multipath situation resulting in high rate deep fading due to the interference between multiple reflected signals. The fading effect along with the attenuation in received signal causes difficulties in detection and tracking of the GPS signal in indoor environments.

### ***1.1.3 Diversity system benefits***

In order to overcome the fading and attenuation difficulties, one of the approaches is receiving signal from different sources and combining them and establishing a *diversity system*. In order to receive a reasonable processing gain and fading mitigation, the diversity sources need to be independent or highly uncorrelated (Rappaport 2002). Different types of diversity systems can be launched including time, frequency and antenna diversity. Antenna diversity which is the main subject of this thesis is categorized into spatial, polarization and pattern diversity. The main objective of this work is to perform a feasibility study that consists of implementing polarization diversity and analyzing the empirical results to quantify the improvement in indoor signal detectability. Compared to spatial diversity, a compact dual polarized antenna can be utilized to create a polarization diversity structure. In fact in this approach the receiver antennas are not required to be physically spaced apart (in comparison with the spatial diversity) to receive independent signals which are practically more suitable for handheld and small GNSS devices.

In order to implement a polarization diversity system the received signal need to be composed of two perpendicular polarized signals. In GNSS applications, the line of sight (LOS) transmitted GNSS signals are right hand circularly polarized signals (RHCP). Since the signal polarization changes upon reflection, the reflected waves are elliptically polarized signals which include a left hand circularly polarized (LHCP) component in addition to the RHCP element (Yang & Porter 2005). In indoor environments, since the signal is highly likely to be subject to reflections, the final received signal can be assumed to be elliptically polarized and, hence, includes both RHCP and LHCP components. In this work, using a dual polarized antenna in indoor areas, the received RHCP and LHCP signals are captured and a polarization diversity structure is established in order to investigate such an approach for GNSS applications as a novel method for enhancing GNSS signal detectability.

## **1.2 Limitation of previous works**

In order to overcome the difficulties of positioning under weak GPS signal conditions, such as urban and indoor environments, various approaches have been developed and investigated such as High-sensitivity GPS (HSGPS), assisted GPS (AGPS), using the modernised GPS signals, and combining a diverse array of antenna elements.

HSGPS receivers generally rely on increasing the integration time to enhance the acquisition and tracking sensitivity; however, the maximum coherent integration time in a GPS receiver is limited by the data navigation period (20 ms). Shanmugam (2008) reports the problems of high sensitivity acquisition under weak GPS signal conditions. In addition, the performance of HSGPS receivers under degraded signal environments are

discussed by MacGougan (2003), Cannon et al (2003), and Lachapelle et al (2003). Assisted GPS can be used to improve the performance of HSGPS in indoor environments. Gao & Lachapelle (2008) and Bancroft et al (2008) propose using an inertial measurement unit (IMU) to aid HSGPS in environments where LOS is not readily available, e.g., urban areas, indoors and dense forests. However, such architectures require to be initialized outdoors and lead to significant error in indoor environments where the absolute position cannot be updated through GPS signals. Watson et al (2006) use a reference antenna to wipe off the navigation data bit and raise the coherent integration time up to 10 s. Increasing coherent integration time under weak received signal for both assisted and stand alone schemes is compared in Kazemi & O'Driscoll (2008) and it is shown that their proposed differential phase lock loop (DPLL) can maintain the phase lock down to 10 dB-Hz for attenuated real GPS signals. However, such results are not trustworthy for indoor situations where the GPS signal is subjected to fading. Moreover, using a reference antenna or aiding from other networks generates dependency to another station. To eliminate such issues, and by introducing the modernized GPS signals, new approaches are examined by taking the advantages of pilot signals. For example, Psiaki (2004) proposes an FFT based block processing acquisition method for L2 civilian moderate (CM) and civilian long (CL) signals under weak signal conditions. Lim et al (2006) estimate the L2 CM code phase and carrier Doppler by developing a fast acquisition scheme on L1 signal. Ioannides et al (2007) show the improvement in the acquisition and tracking performance by combining energies at the L1, L2 and L5 bands for both data and pilot signals.

In addition, a diverse array of approaches has been investigated in order to improve post-correlation SNR (PSNR) and overcome signal detection problems in indoor situations by spatial combining of multiple antenna elements. Mahfuz (2008) proposes an optimum spatial post-correlation signal processing and detection algorithm for multiple-antenna array GPS receivers. Nielsen et al (2008) analyze theoretically and experimentally the processing gain achievable through spatial combining of a pair of antennas. Broumandan (2009) has proposed a new approach based on the synthetic array concept to enhance the detectability of GPS signal in indoor locations. Although the application of diversity schemes to GNSS appears to be new, it has been used broadly in the communication systems (Lee 1998). Spatial diversity is thoroughly discussed in Haykin (2000). Colburn et al (1998) evaluate the spatial diversity performance of three different antenna configurations for the indoor 902-928 MHz propagation channel. They show that the indoor propagation channel has either Rician or Rayleigh models and the fading distribution characteristics are discussed. Their experimental results indicate that the three proposed antenna configuration achieve sufficient decorrelation to use in a diversity system. Time and phase diversity is studied in Bolcskei et al (2006) and Hyeon et al (2008), respectively. Narayanan et al (2004) extensively analyse the polarization diversity and channel characteristics at 1800 MHz which is close to the L1 frequency (1575.42 MHz). The effect of correlation between two channels on diversity gain has been discussed in this research. In addition, they evaluate the performance of polarization diversity using different antenna configurations in both Rayleigh and Rician environments. In addition, Narayanan et al (2004) quantify both complex and envelope correlation coefficient and concludes that the value of complex correlation coefficients is

constant from run to run and hence it is a more reliable metric. Lemieux et al (1991) compare space, frequency and polarization diversity in the indoor environment experimentally for frequency of 900 MHz. In addition, Singer (1998) compares the spatial diversity and polarization diversity and discusses their pros and cons individually and concludes that polarization diversity is a useful and optimized technique in the high multipath environments.

### **1.3 Objectives and novel contributions**

Given the lack of research directed towards analyzing GNSS RHCP and LHCP signals and taking advantage of their combination, the objective of this thesis is to characterize and utilize these signals in indoor locations to enhance GNSS signal detection in indoor environments. Polarization diversity is widely used in communication systems. Although this method has been employed to mitigate the multipath effect in GNSS applications (e.g., Izadpanah (2009) and references therein), using a dual polarized antenna and diversity schemes to improve the detectability of the GNSS signals in indoor environments is a novel technique for the case of GNSS. The main contribution of this work is the circular polarization diversity consisting of two RHCP and LHCP antennas as diversity branches. However, in addition to the circular polarization diversity, spatial diversity and linear polarization diversity structures are implemented in order to compare their performance under identical conditions.

The utilized spatial diversity branches are two RHCP antennas spaced apart in order to capture independent signals. Unlike the polarization diversity systems, in spatial diversity systems the antennas are required to be physically spaced apart to receive

independent signals, which are not practically suitable for handheld and small GNSS devices.

Linear polarization diversity structure is created from two linear polarized antennas placed perpendicularly corresponding to each other and called vertical and horizontal antennas. Since the amplitude and phase of vertical and horizontal components of electric field of electromagnetic waves are varying independently, the vertical and horizontal components of the captured signals in high multipath environments may fluctuate independently (Rappaport 2002). Therefore, a diversity system consists of two perpendicular linear polarized antennas capturing independent signal in its branches.

In order to achieve the above objectives the following tasks are performed:

- 1. Characterizing the received signals:** In the first step, the characteristics of both GNSS RHCP and LHCP signals in indoor and high multipath environments are analyzed and investigated in order to measure multipath channel statistics and determine channel correlation between RHCP and LHCP antennas. According to the probability density function of the channel phase rate for a given carrier frequency (Jakes 1974), the sampling rate and rover speed should guarantee that almost whole of the sampled signal remains free for aliases or within the Nyquist interval. This will be determined based on the probability density function of the channel phase rate discussed in Chapter 4. Considering these conditions, the final received signal envelope can be either Rayleigh or Rician distributed depending on the mean of the received Gaussian signals. In the case of zero mean Gaussian components, the signal envelope has a Rayleigh distribution; otherwise it is distributed

according to the Rician distribution. Herein, utilizing live GPS signals gathered in various indoor locations, the probability distribution functions of the received signals are examined and compared with the theorem.

- 2. Quantifying the correlation coefficient:** In order to achieve an adequate diversity gain from combining a diverse array of branches, the correlation between received signals should be sufficiently low (Narayanan et al 2004). The correlation coefficient between two received signals can be characterized by using either the envelope or complex forms of the input signals. Assuming that the received signals have a Rayleigh distributed envelope and uniformly distributed phase, the envelope and complex correlation coefficient are associated with each other as explained in Gao (2007). However, in this project the complex correlation coefficient between the received RHCP and LHCP signals is evaluated.
- 3. Exploring combining approaches:** Once the GNSS signals are received via multiple branches, the next step is to combine the output of these branches to improve detection performance. The received signals from different branches can be combined using various techniques to alleviate the signal fading such as selection combining, maximum ratio combining and the likelihood ratio test (Mahfuz 2008). Selecting the combining method is connected with the probability distribution function of the input signals and the correlation between them. The indoor propagation channel is usually modeled by Rayleigh fading in which there is no well defined line of sight signal component (Broumandan 2009). Hence, the In-phase and Quadrature

components of received signals are Gaussian and consequently the likelihood ratio test lead to the Estimator Correlator (EC). In the case of uncorrelated input signals, EC can be simplified to the Equal Gain (EG) and it can be considered as an optimum detector (Kay 1998). In addition, it can be shown that in the case of a correlation coefficient of less than 0.5 between the input signals at each diversity branch, the performance of both EG and EC combining schemes is substantially similar (Zaheri et al 2009). However, the performance of the EC combining surpasses that of the EC when the correlation coefficient is higher.

- 4. Empirical data analysis:** In order to investigate the validity of the theoretical findings, a large number of data sets are collected in various indoor locations using a commercial active dual polarized antenna mounted on a linear motion table to characterize the indoor GNSS channel. In addition to circular polarization diversity, some data sets with linear polarization diversity and spatial diversity structures are collected. In order to establish an optimum combiner for received signals, the probability distribution functions (PDF) of received signals are analyzed to model the channel characteristics. In addition, the cross correlation coefficient of received signals in diversity structures is quantified. Then, the collected signals are combined using an appropriate and optimum combiner. In order to evaluate the performance of the proposed method, the receiver operating characteristics (ROC) curve for combined signals in different diversity structures are derived and compared with the single antenna curves. In the next stage, the diversity gain for various satellite

vehicles in different indoor environments is quantified. According to the provided results, it is shown that there is a low cross correlation coefficient between received signals in the proposed polarization diversity system. In addition, the overall detection performance in indoor areas using the proposed approach is quantified.

#### **1.4 Thesis Outline**

Chapter 2 describes the wireless communication properties and explains fading channel models including flat and frequency selective and their characteristics. In addition, it discusses different techniques to improve the signal detection performance in fading environments. It also describes different diversity systems that are used to mitigate the received signal fluctuation. The polarization and spatial diversity systems are described in details as the main objectives of this work. Moreover the combining methods used in the literature to combine received signals in the diversity branches are reviewed in this chapter.

Chapter 3 is assigned to the fundamental electromagnetic signal characteristics, especially GNSS signals and the polarization fluctuations due to reflections. The detection procedure for both single and multiple antennas are then described. In addition, the combining methods used in this work are explained in detail.

In Chapter 4, the evaluation methods for different detection approaches are discussed and the performance of combining methods explained in Chapter 3 are compared for various input signal configuration in terms of correlation coefficient and input power.

Chapter 5 deals with the experimental result analysis and proposed method performance evaluation. It explains the test setup for live GPS data collection and the correlator design and developed program for combining captured signals. The cross correlation coefficient is quantified and the received signals in diversity branches are compared in terms of input power. Circular polarization diversity performance is quantified in terms of diversity gain. In addition, the performance of circular polarization diversity is compared with the spatial and linear polarization diversity structures.

Chapter 6 presents conclusions and limitations of the proposed methods and recommendations for future work.

## Chapter Two: Fading Channels and Diversity Systems

Since the GNSS signal detection in indoor fading environments is the main focus of this work, the fading channels and their characteristics are discussed in this chapter. Small-scale fading is introduced and the flat fading resulting from combination of multiple reflected signals is defined. The approaches for improving the signal detection performance are explained and the diversity systems and their properties are discussed in details. The GPS signal architecture and detection procedure in order to extract the navigation data and signal transmitted time are discussed and signal combining methods are described.

Since this work deals with statistical signal processing along with the analyzing received signal characteristics, different signal distribution models which the signal in indoor environments faces are defined and their properties are also discussed. The materials presented in this chapter can be found in more details in textbooks such as Rappaport (2002) and Blaunstein & Andersen (2002).

### 2.1 Small-Scale Fading channel

The *small-scale fading* or simply *fading* term describes the rapid fluctuations of the received signal amplitude over a short period of time or travel distance (Rappaport 2002). By this definition, path loss effects are ignored and are not considered as fading. The fading phenomenon results from interference between multiple versions of the transmitted signals which arrive at the receiver at slightly different times due to signal reflection from various reflectors and received at the receiver antenna from different paths. These multiple waves, denoted as multipath propagation, combine vectorially at the receiver antenna and result in various fading types as a function of many physical

factors such as transmitted signal bandwidth, speed of mobile antenna and surrounding objects and multipath propagation channel. In this chapter, the various types of fading channels and their parameters will be discussed.

### ***2.1.1 Parameters of mobile multipath channel***

Many parameters of a multipath channel can be derived using the power delay profile of a channel. The power delay profile represents the relative received power as a function of excess delay with respect to a fixed time delay reference ( $t_0$ ). It can be derived by averaging the instantaneous power delay profile measurements over a local area (Rappaport 2002) and it can be shown as

$$|r(t)|^2 = \sum_{k=0}^{N-1} a_k^2(t), \quad 2-1$$

where  $a_k(t)$  is the real amplitude of the  $k$  th multipath component at time  $t$  and  $N$  is the total number of possible equally spaced multipath components which carry similar delay time.

#### **2.1.1.1 Time dispersion Parameters**

In order to develop general design guidelines for a wireless channel, parameters which grossly quantify the multipath channel should be determined. The time dispersive properties of a small scale multipath channel are commonly evaluated by its mean excess delay ( $\bar{\tau}$ ) and root mean square (rms) delay spread ( $\sigma_{\tau}$ ) and these can be quantified using a power delay profile as (Rappaport 2002)

$$\bar{\tau} = \frac{\sum_k a_k^2 \tau_k}{\sum_k a_k^2} = \frac{\sum_k P(\tau_k) \tau_k}{\sum_k P(\tau_k)} \quad 2-2$$

and

$$\sigma_{\tau} = \sqrt{\langle \tau^2 \rangle - (\bar{\tau})^2} \quad 2-3$$

respectively, where

$$\langle \tau^2 \rangle = \frac{\sum_k a_k^2 \tau_k^2}{\sum_k a_k^2} = \frac{\sum_k P(\tau_k) \tau_k^2}{\sum_k P(\tau_k)}. \quad 2-4$$

These delays are measured relative to the first detectable received signal at  $t_0 = 0$  and are derived from a single power delay profile defined by averaging over consecutive impulse response measurements of the channel. The rms delay spread is derived for various channels in the literature and Rappaport (2002) has tabulated some of them. For example in terrestrial based wireless, the typical measured values for rms delay spread for indoor area are on the order of nanoseconds and of the order of microseconds in outdoor radio channels (Rappaport 2002).

#### 2.1.1.2 Coherence Bandwidth

The coherence bandwidth ( $B_c$ ) is a statistical range of frequencies over which the channel can be considered as “flat”. In other words, the amplitude of two frequency components in the range of coherence bandwidth is highly correlated since the channel passes all components among the coherence bandwidth with approximately equal gain and linear phase.

The coherence bandwidth can be defined approximately proportional to the inverse of rms delay spread. The coherence bandwidth can be defined over which the frequency correlation function is above 0.5 as (Rappaport 2002)

$$B_c \approx \frac{1}{5\sigma_\tau}. \quad 2-5$$

### 2.1.1.3 Doppler spread

The Doppler spread and coherence time illustrate the time varying nature of the channel caused by relative motion of the mobile and satellite, or by wireless channel object movement. The Doppler spread  $B_D$  is defined as the range of frequencies over which the received Doppler spectrum is non-zero (Rappaport 2002). The Doppler spectrum of a transmitted pure sinusoidal tone of frequency  $f_c$ , has components in the range of  $f_c+f_d$  and  $f_c-f_d$ , where  $f_d$  is the Doppler shift for the transmitted signal and is a function of the relative motion of the receiver and the transmitter ( $v$ ) and the carrier wavelength ( $\lambda$ ).

### 2.1.1.4 Coherence time

The coherence time  $T_c$  is defined as a statistical measure of the time duration over which the channel impulse response is essentially invariant and evaluate the similarity of channel behaviour at different time (Rappaport 2002). In other words, coherence time for a channel is the maximum time duration over which two received signals are highly correlated. The Doppler spread and coherence time are inversely proportional to one another and a common rule of thumb for modern communication is defined by Rappaport (2002) as

$$T_c = \frac{0.423}{f_m}. \quad 2-6$$

The term  $f_m$  is the Doppler spread and defined as the maximum Doppler shift given by  $f_m = v / \lambda$ . According to the definition of the coherence time for a channel, a

conservative value for coherent integration time can be evaluated. For example, a GPS receiver in indoor areas receives signals from various scatters and reflectors. Assuming that the average relative velocity of the GPS antenna and the scatters is 2 cm/s, the Doppler spread for the GPS L1C/A code will be quantified as 0.1 Hz and the maximum recommended coherent integration time according to the Eq. 2-6 is 4 seconds. This implies that two signals arriving through this channel with a time delay greater than 4 seconds are affected differently by the channel.

### ***2.1.2 Types of signal fading***

Depending on the relation between the signal parameters and the channel characteristics, the transmitted signal will be faced with different types of fading. The time and frequency dispersion (resulting from different frequencies propagating at different speeds) of a mobile radio channel lead to two independent propagation mechanisms. The multipath delay spread results in *flat fading (time dispersion)* or *frequency selective fading* while the Doppler spread leads to *fast fading (frequency dispersion)* or *time selective fading* (Rappaport 2002).

#### **2.1.2.1 Flat fading due to multipath time delay spread**

If a mobile radio channel carries a constant gain and a bandwidth greater than the transmitted signal bandwidth, the received signal will undergo flat fading. It is worthwhile to emphasize that although the channel gain is constant for a spread of frequencies, the received signal amplitude changes over time due to fluctuation in the gain of the channel by multipath and it leads to deep fading in the received signal amplitude.

### 2.1.2.2 Frequency selective fading due to multipath time delay spread

If a radio channel possesses a constant gain and a linear phase response along with a bandwidth smaller than the transmitted signal bandwidth, the received signal will be affected with the frequency selective fading. Under such conditions, the received signal includes multiple copies of attenuated and delayed versions of the transmitted signal. Viewed in the frequency domain, different frequency components of the transmitted signal are faced with different gains since the channel spectrum does not have a constant gain for all components.

### 2.1.2.3 Fast and slow fading due to Doppler spread

Depending on the transmitted baseband signal change rate compared to the change of channel the signal may be either fast or slow fading. In a fast fading channel, in contrast to a slow fading one, the channel impulse response varies rapidly compared to the transmitted signal change rate. The speed of receiver or objects in the channel and the base band signal rate determine whether a signal will be affected by either fast or slow fading.

It should be noted that the channel fading characteristics due to time delay spread is totally independent from channel fading due to frequency spread. In other words, a flat fading channel can be categorized as fast or slow fading depending on the relative variation rate of the channel impulse responses and the transmitted signal.

## **2.2 Diversity systems**

In order to improve the signal quality in the receiver, different approaches depending on the fading channel properties including equalization, diversity and channel coding can be applied. The channel coding is to detect or correct the errors caused by the

wireless channel by adding extra bits to the transmitted message. Equalization is used to alleviate intersymbol interference (ISI) created in the channels in which the modulation bandwidth exceeds the coherence bandwidth of the radio channel resulting in frequency-selective fading. Diversity systems are employed to reduce the depth and duration of fades on signals in a flat fading (narrowband) channel (Rappaport 2002). As mentioned, the received GPS signal in a multipath environment suffers from deep fades. A diversity system can improve the signal quality by incorporating another independent (or highly uncorrelated) signal path with higher signal strength. There are different types of diversity systems which can be used to alleviate the fading effect and which can be divided in three main categories, namely: time, frequency and antenna diversities (Parsons 2000).

The main idea in antenna diversity systems is based on the fact that at the moment where the fading affects the output of a diversity branch, another branch may have a reasonable SNR. In Figure 2.1, the SNR outputs of two spatially separated antennas located in an indoor environment are plotted. As shown in this figure, while antenna 1 is faded, the other one carry a strong signal and vice versa. Therefore, combining independent copies of transmitted signals received by diversity branches leads to less fading and higher overall SNR which improves the detection procedure.

In antenna diversity systems, the receiver uses multiple antennas with different characteristics to collect statistically independent signals to establish a diversity system (Figure 2.2). These antennas can be different in terms of pattern, polarization or location, resulting in diversity systems known as pattern, polarization and spatial diversity,

respectively. The polarization and spatial diversities are widely used in practice and will be discussed in more details in the following sections.

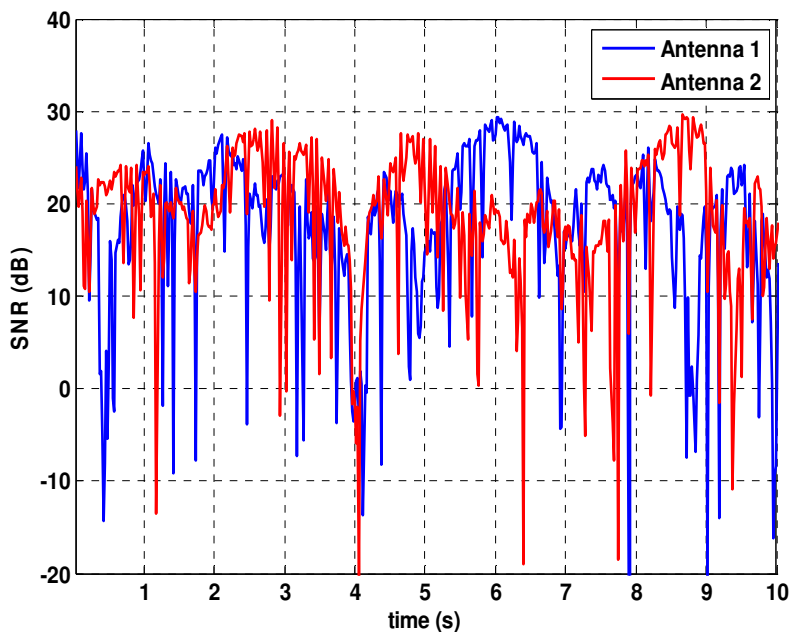


**Figure 2.1: SNR of two independent antennas experiencing deep fades**

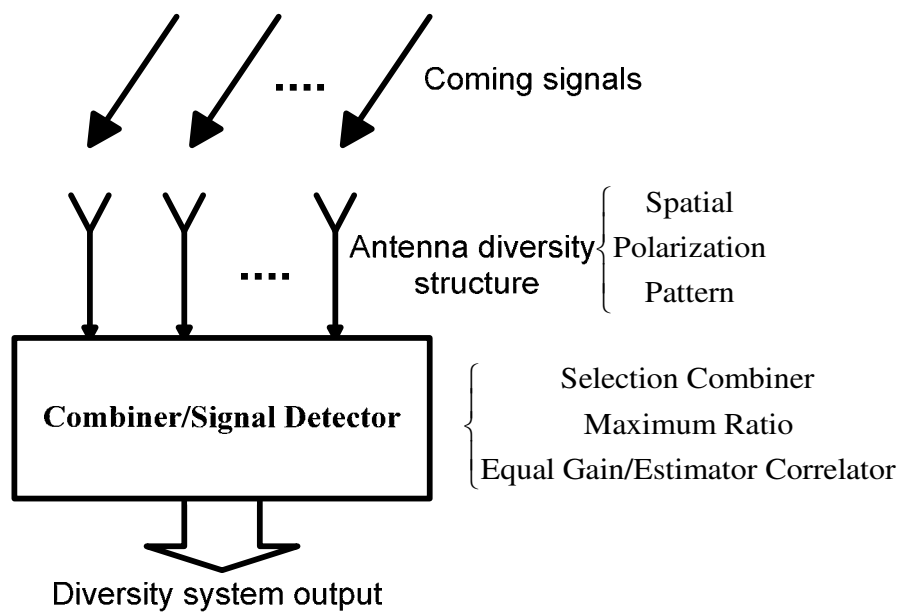


**Figure 2.2: Antenna Diversity Scheme**

### 2.2.1 Spatial diversity

The main concept in spatial diversity is that in a multipath environment, fading is a random function of antenna location (Rappaport 2002). Therefore, according to this fact, in a spatial diversity system, an array of spaced apart antennas is utilized to achieve independent fading paths.

The arrangement of multiple antennas to receive multiple signals with uncorrelated fading is the most important issue in spatial diversity, since the spatial correlation and signal Angle of Arrival (AoA) statistics are strongly related. The statistics of how the electromagnetic waves arrive from different directions on antennas are defined as AoA statistics. According to Jakes (1977), the antennas need to be separated with a minimum required distance depending on different fading environments in order to achieve sufficient decorrelation between received signals. In fact, the spatial signal covariance matrix is a function of both the array geometry and AoA statistics of the incoming signals and assumptions of different signal distributions result in different correlation values (Park & Min 2005). The AoA distribution mostly is considered as a uniformly distributed function in indoor environments (Naguib 1996, Salz & Winters 1994, Clarke 1968, Broumandan 2009).

Broumandan (2009) has quantified the spatial correlation coefficients as a function of the antenna separation over wavelength ( $\Delta D / \lambda$ ) for a uniform AoA distribution with an angle of spread of  $\varphi$ , as shown in Figure 2.3, where  $\theta$  is the mean of incident signal direction. It is assumed that the scatters and the antenna array are located in the same plane. According to this graph, it is obvious that the correlation coefficient between received signals in spatial diversity systems depends on the reflector

angle spread and environment specifications. Figure 2.3 shows that when the signal is approaching the antenna through a small sector of  $\varphi = 15^\circ$ , the antenna separation must be more than four wavelengths. On the other hand, when the reflected signals are arriving from all directions ( $\varphi = 360^\circ$ ), almost half wavelength separation will result in a sufficiently low correlation coefficient. This condition, known as ring of scatters model, is generally considered as the indoor channel model in the literature (Parsons 2000, Rappaport 2002).

### 2.2.2 Polarization diversity

In the polarization diversity system, antennas with orthogonal polarization are employed to form a diversity system (Rappaport 2002). Compared to spatial diversity, a compact dual polarized antenna can be utilized to create a polarization diversity structure.

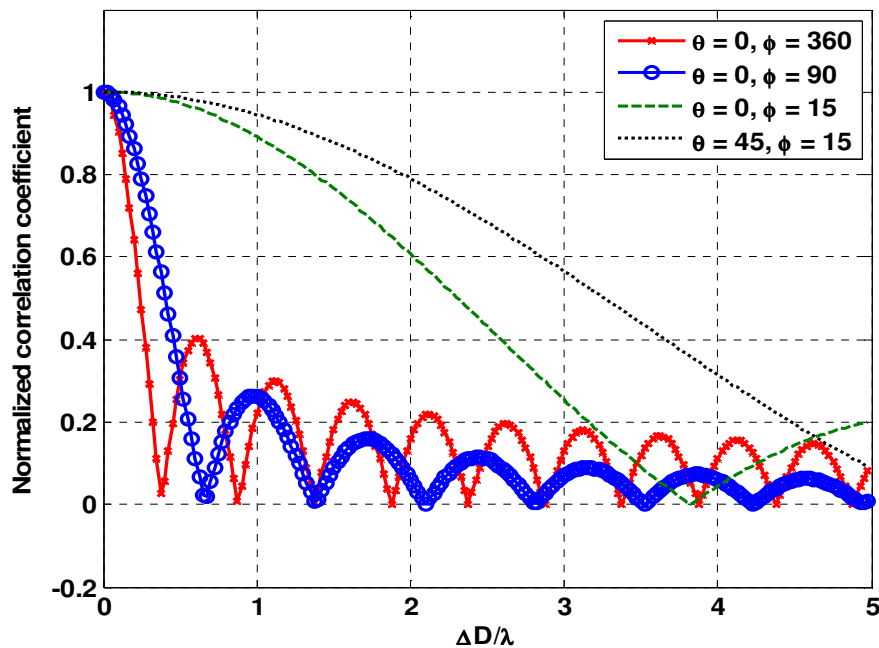


Figure 2.3: Spatial correlation coefficient for various angle of spread

In fact in this approach the receiver antennas are not required to be physically spaced apart to receive independent signals which are practically more suitable for handheld and small GNSS devices.

Using polarization diversity in indoor locations is based on the concept that in high multipath environments the signal polarization is subject to change due to diffraction, refraction and reflection. In this work both combination of RHCP-LHCP and Vertical-Horizontal antennas are examined.

As mentioned before, GNSS signals in indoor environments are not pure RHCP signals and they consist of Right Hand Elliptically Polarized (RHEP) and Left Hand Elliptically Polarized (LHEP) components which can be decomposed to RHCP and LHCP signals. However, the received signals components in the orthogonal antennas should be adequately discriminated to achieve a sufficiently low correlation coefficient between received signals. To accomplish this, the port-to-port isolation of the antennas should be -30 dB and their cross-polarization ratio, the antenna gain for the undesirable component (opposite polarization), should be less than -20 dB (Singer 1998).

Another employed structure for polarization diversity is the combination of received signals from linear polarized antennas. This is based on the fact that the amplitude and the phase of vertical and horizontal components in reflected GNSS signals are varying independently since the parallel and perpendicular components of reflection coefficients for any reflector are independent (Rappaport 2002). These antennas are simpler in term of design and implementation which leads to lower overall cost of mobile devices. However, lower average SNR is expected in this structure since the orthogonal

components of a circular polarization signal carry almost 3 dB less power than the original wave.

## **2.3 GPS signal model**

### ***2.3.1 GPS signal architecture***

In terms of signal modulation, a GPS signal uses a Direct Sequence-Code Division Multiple Access (DS-CDMA)-based technique to allow all satellites transmit their information at the same frequency and time using different pseudo-random noise (PRN) codes. Each satellite uses a unique PRN code known to the receivers with a low cross-correlation between different PRNs. The receiver correlates the captured signal with a replica of the locally generated PRN code to extract both the transmitted information and estimate the signal transmission time. The length of the civilian GPS signal code is 1023 chips and is derived from the Gold codes family known as Coarse/Acquisition (C/A) codes. The chipping rate is 1.023 MHz resulting in a code repetition of 1 ms. The PRN code is combined with the navigation data bits which are transmitted at 50 Hz leading to 20 PRN code period. The navigation data contains information such as satellite clock, ephemeris data and almanac components. Finally, the signal is Binary Phase Shift Keying (BPSK) modulated on a carrier wave prior to transmission. The carrier frequency is 1575.42 MHz for L1 GPS signal.

### ***2.3.2 Baseband signal processing***

Having passed through the low noise amplifier and band pass filter, the RF signal captured by the antenna is down-converted into digital samples through the down-conversion process. In the down converter, the RF signal is multiplied by a locally generated signal with frequency equal to  $f_L - f_{IF}$ , where  $f_L$  is the GPS signal carrier

frequency and  $f_{IF}$  is the intermediate frequency. The resulting signal is filtered by a band pass filter blocking all signals but the one close to the intermediate frequency. The down converted signal is sampled and digitized by a Digital to Analog Convertor (ADC). The digitized signal is saved for baseband processing.

The complex GNSS signal in the intermediate frequency can be denoted as

$$r(t) = h(t)s_0(t)\exp(j2\pi f_{IF}t) + w(t), \quad 2-7$$

where  $h(t)$  is the complex channel gain as a function of time  $t$  and  $w(t)$  is complex additive white Gaussian noise and  $s_0(t)$  is the transmitted signal from satellite, where

$$s_0(t) = d(t - \tau)c(t - \tau)\exp\{j(2\pi f_D t + \psi)\}, \quad 2-8$$

and  $d(t)$  is the navigation data modulation,  $c(t)$  is PRN code,  $\tau$  represents the code phase,  $\Delta f$  stands for the carrier frequency offset (due to the Doppler effect and frequency offset of the receiver local oscillator),  $\psi$  is the initial phase offset. The  $s_0(t)$  parameters are known to the receiver except for the navigation data, the code phase, the carrier frequency offset and the initial phase offset.

The IF signal passes through the signal acquisition procedure as an initial operation dealing with the detection and coarse estimation of Doppler and code phase offset. A two dimensional search is applied on the signal to roughly estimate the Doppler frequency and code phase offset. For the GPS L1 frequency, the Doppler shift due to satellite motion is typically of the order of  $\pm 5$  kHz. However, the frequency error of the local oscillator and user motion (small in comparison) typically adds another uncertainty and may increase the Doppler search up to  $\pm 10$  kHz in exceptional cases. On the other hand, the code phase can be any value and since the code repeats any 1 ms, the search is

applied within 1 ms of signal duration. After a coarse estimation of Doppler frequency and code phase, a tracking algorithm is implemented for their fine estimation. Having estimated the Doppler shift and code phase, these can be removed from the received signal in order to estimate and extract the navigation data bits. For more details, the reader is referred to Misra & Enge (2006) and Kaplan & Hegarty (2006).

### 2.3.3 Single antenna signal detection procedure

As mentioned previously, a two dimensional search on the Doppler frequency and the code phase is required to despread the BPSK GPS signal and extract the navigation data. This procedure is illustrated in Figure 2.4. Such a procedure should be applied on each code phase ( $\tau$ ) and Doppler frequency difference ( $f_D$ ) in the search space. In the first stage the frequency offset is removed and then the locally generated PRN code is correlated with the signal. Here,  $N_{coh}$  is the total number of samples pertaining to coherent integration period. The output signal strength can be amplified by increasing the integration time. However, there is a limitation on increasing the coherent integration time due to the navigation data modulation on the signal and it can be increased up to 20 ms if the navigation data bit transition is already detected (Misra & Enge 2006).

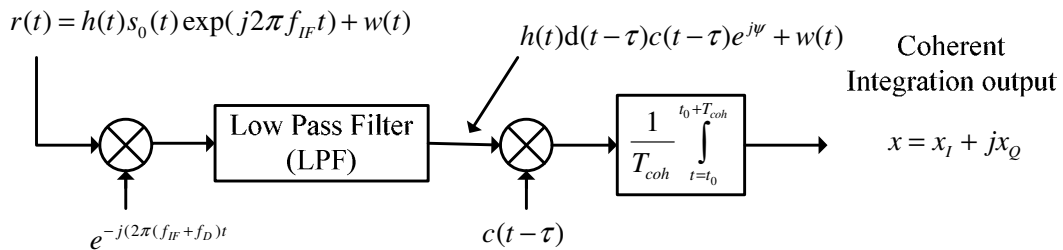


**Figure 2.4: GPS signal Doppler removal and code correlation**

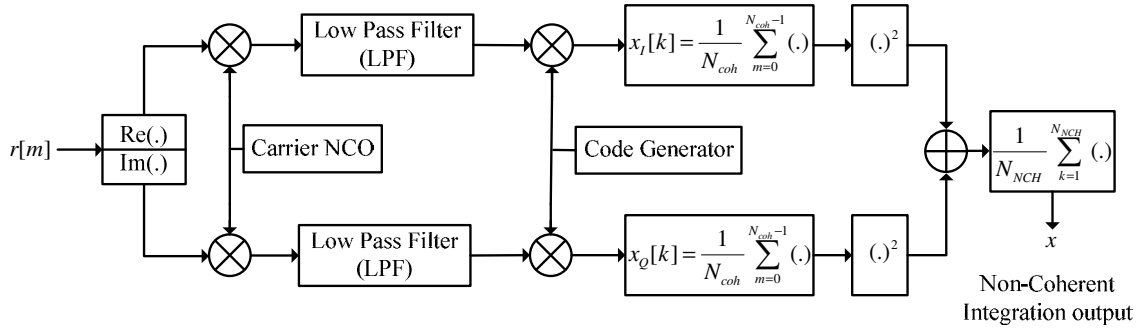


**Figure 2.5: Despreading procedure to estimate the navigation data**

In order to improve the detectability of the signal, a non-coherent combining detector (NCCD) technique can be used in order to increase the integration time without any concern about the navigation data bits. This procedure is shown in Figure 2.5. The NCCD is a standard detection technique that can be used for GPS signals in poor signal conditions. The NCCD accumulate a number of  $N_{NCH}$  outputs from coherent averaging of  $N_{coh}$  samples. However, there is SNR degradation due to envelope detection in the non-coherent combining procedure (Kaplan & Hegarty 2006).

The complex despread signal components, i.e.  $x_I$  and  $x_Q$ , are known as In-phase and Quadrature components of the received signal, respectively. The received signal and the communication channel characteristics can be analyzed using these components and they will be used for indoor signal analysis in this work.

## 2.4 Combining methods

Having collected the RF signal by the diversity branches, the received signals should be combined using an efficient combiner. There are different combiners introduced in the literature (Rappaport 2002, Kay 1998) including selection combining, maximum ratio combining and likelihood ratio test. These combiners are discussed and

analyzed in this section in order to select the most efficient one for this work by comparing them analytically.

### 2.4.1 Selection combining

In this technique, the output of the combiner is chosen as the output of that branch with the highest SNR at any time. In fact, the SNR of each branch is observed using one individual processing module. In this approach  $M$  processing modules are used for a diversity scheme including  $M$  branches. However, due to difficulties to accurately estimate the SNR, a practical selection combiner cannot function on a truly instantaneous basis (Rappaport 2002). In addition, since at any time only one of the branches is used, this technique is not called an efficient combiner. Figure 2.6 represents the schematic of selection combining method.

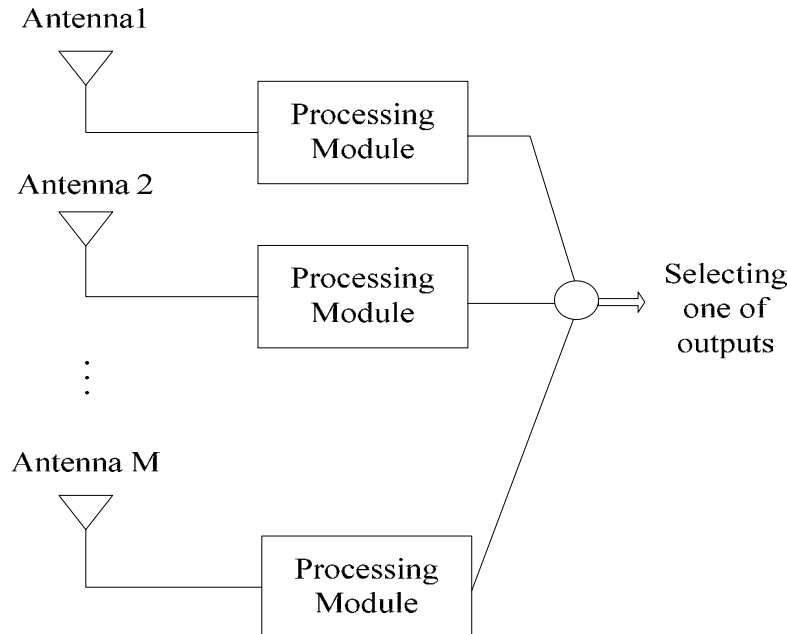


**Figure 2.6: Selection combining scheme**

### 2.4.2 Maximum ratio combining

In this method, each branch is weighted using a complex value to co-phase the input signals and combine them coherently (Figure 2.7). Subsequently, the output is treated as a single signal and the detector and test statistic function are applied on it.

Considering each co-phased received signal excluding the noise as  $x_m$ , the total output can be written as

$$X_T = \sum_{m=1}^M a_m x_m \quad 2-9$$

and the total noise power of combined signal can be shown as

$$\sigma_T^2 = N_{avg} \sum_{m=1}^M |a_m|^2, \quad 2-10$$

where  $N_{avg}$  is the average noise power in each channel.

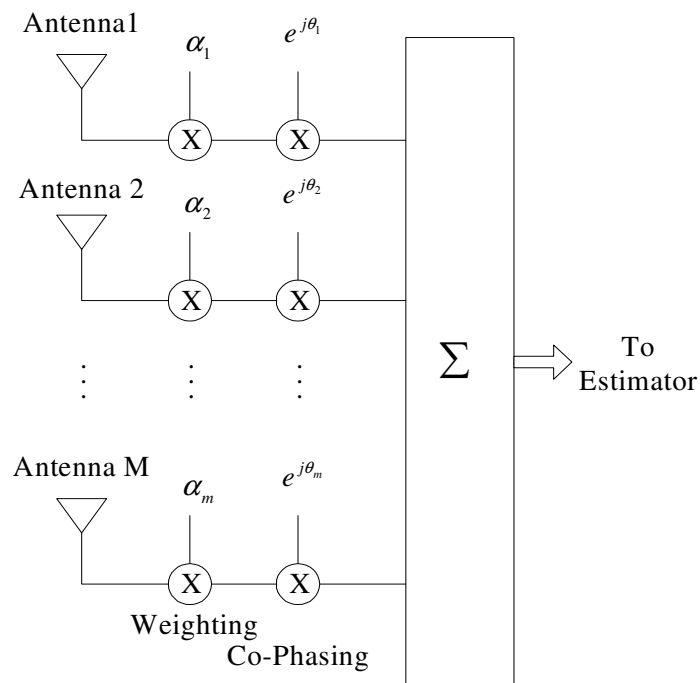


**Figure 2.7: Maximum ratio combining method**

In order to achieve the maximum SNR at the output of this approach, each branch should be weighted according to its individual SNR (Rappaport 2002). If the weighting values are chosen as  $a_m = \frac{x_m^*}{N_{avg}}$ , the total SNR applied to the detector will be maximum,

which is the summation of all input SNRs and is given as

$$\begin{aligned}
 SNR_{total} &= \frac{(Z_T / \sqrt{2})^2}{\sigma_T} = \frac{(\sum_{m=1}^M a_m x_m)^2}{2N_{avg} \sum_{m=1}^M |a_m|^2} \\
 &= \frac{1 / N_{avg}^2 (\sum_{m=1}^M |x_m|^2)^2}{2 / N_{avg} \sum_{m=1}^M |x_m|^2} \\
 &= \sum_{m=1}^M \frac{|x_m|^2}{2N_{avg}} = \sum_{m=1}^M snr_m.
 \end{aligned} \tag{2-11}$$

As mentioned before, the received signal envelope in a wireless channel is the sum of the squares of two independent Gaussian random variables, In-phase ( $x_I$ ) and Quadrature ( $x_Q$ ), which are zero mean in Rayleigh fading channels. That is,

$$x_m = x_I + jx_Q \Rightarrow |x_m|^2 = x_I^2 + x_Q^2. \tag{2-12}$$

Since

$$snr_m = \frac{|x_m|^2}{2N_{avg}}, \tag{2-13}$$

the  $snr_m$  is a Chi-square random variable with two degrees of freedom (DOF). As a result, the total SNR,  $\zeta$ , becomes a Chi-square distribution with  $2M$  degrees of freedom with

variance  $\sigma^2 / (2N_{avg}) = \Gamma / 2$  ( Rappaport 2002). Its probability distribution function (PDF) under the above mentioned condition can be written as

$$p(\zeta) = \begin{cases} \frac{\zeta^{M-1} e^{-\frac{\zeta}{\Gamma}}}{\Gamma^M (M-1)!} & \gamma \geq 0 \\ 0 & \gamma < 0 \end{cases} . \quad 2-14$$

In addition, its cumulative distribution function (CDF) can be derived as

$$\begin{aligned} P(\zeta) &= p(\zeta \leq l) = \int_0^l p(\zeta) d\gamma \\ &= 1 - e^{-l/\Gamma} \sum_{k=1}^M \frac{(l/\Gamma)^{k-1}}{(k-1)!} . \end{aligned} \quad 2-15$$

The CDF for the total output SNR is depicted in Figure 2.8. It shows that increasing the number of branches reduces the probability of fading for a given SNR threshold.

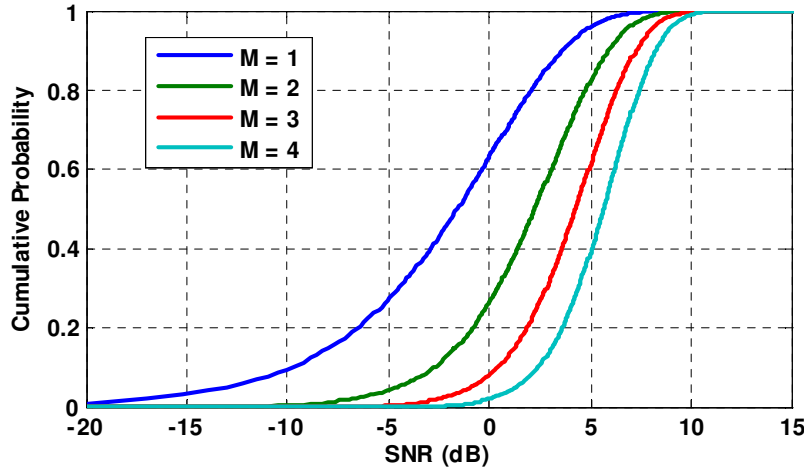


**Figure 2.8: SNR cumulative distribution function of maximum ratio combining**

### 2.4.3 Likelihood ratio test (LRT)

Consider the detection problem of a random signal embedded in a White Gaussian Noise (WGN). The detection problem is to distinguish between the following conditions of  $H_1$  and  $H_0$  expressed as

$$\begin{aligned} H_0 : x[m] &= w[m] & m = 0, 1, 2, 3, \dots, M-1 \\ H_1 : x[m] &= s[m] + w[m] & m = 0, 1, 2, 3, \dots, M-1 \end{aligned} \quad 2-16$$

where  $s[m]$  is the sample of desired deterministic signal received at the antenna excluding the noise with a zero mean circular normal distribution and the covariance matrix of  $C_s$ , the  $w[m]$  is the embedded zero mean white complex Gaussian noise with a covariance matrix of  $C_w$  and  $M$  is the number of samples that the detector uses to take the final decision. Therefore,

$$\begin{aligned} x &\sim \begin{cases} CN(0, C_w) & \text{under } H_0 \\ CN(0, C_s + C_w) & \text{under } H_1 \end{cases} \\ C_w &= \sigma_w^2 \mathbf{I}_M \end{aligned} \quad 2-17$$

where  $\sim$  indicate the PDF of the left hand side variable,  $CN(a, b)$  signifies a complex normal distribution with mean of  $a$ , and the variance of  $b$  and  $\rho$  is the correlation coefficient between received signals and  $\mathbf{I}_M$  is an  $M \times M$  identity matrix.

According to the Neyman-Pearson (NP) criterion, the detector objective is to maximize the probability of detection ( $P_D$ ) subject to a constraint on the probability of false alarm ( $P_{FA}$ ). The NP detector chooses  $H_1$  if the likelihood ratio test ( $L(x)$ ) exceed a threshold ( $\gamma$ ) as (Kay 1998)

$$L(x) = \frac{p(\mathbf{x}; H_1)}{p(\mathbf{x}; H_0)} > \gamma \quad 2-18$$

where  $\mathbf{x} = [x[0], x[1], x[2], \dots, x[M-1]]^T$  is the received signal vector and the threshold is chosen to meet the probability of false alarm criteria ( $P_{FA}=a$ ). For the conditions in Equation 2-17,  $p(\mathbf{x}; H_1)$  and  $p(\mathbf{x}; H_0)$  are expressed as

$$p(\mathbf{x}; H_1) = \frac{1}{\pi^M \det(\mathbf{C}_s + \sigma_w^2 \mathbf{I}_M)} \exp\left[-\mathbf{x}^H (\mathbf{C}_s + \sigma_w^2 \mathbf{I}_M)^{-1} \mathbf{x}\right] \quad 2-19$$

and

$$p(\mathbf{x}; H_0) = \frac{1}{\pi^M \sigma_w^{2M}} \exp\left[-\frac{1}{\sigma_w^2} \mathbf{x}^H \mathbf{x}\right] \quad 2-20$$

respectively, where  $(\bullet)^H$  stands for a complex conjugate transpose operator and  $\det(\bullet)$  is the matrix determinant operator. Therefore, the likelihood ratio test is expressed as

$$L(\mathbf{x}) = \frac{\sigma_w^{2M}}{\det(\mathbf{C}_s + \sigma_w^2 \mathbf{I}_M)} \exp\left[-\mathbf{x}^H (\mathbf{C}_s + \sigma_w^2 \mathbf{I}_M)^{-1} \mathbf{x} + \frac{1}{\sigma_w^2} \mathbf{x}^H \mathbf{x}\right] > \gamma. \quad 2-21$$

After some manipulation, the final test statistic becomes (Kay 1998)

$$T(\mathbf{x}) = \mathbf{x}^H \mathbf{C}_s (\mathbf{C}_s + \sigma_w^2 \mathbf{I}_M)^{-1} \mathbf{x} = \mathbf{x}^H \hat{S} > \gamma'. \quad 2-22$$

Here,  $\hat{S} = \mathbf{C}_s (\mathbf{C}_s + \sigma_w^2 \mathbf{I}_M)^{-1} \mathbf{x}$  is the Minimum Mean Square Error (MMSE) estimator of  $s$  (Kay 1998). The final test statistic function in Equation 2-22 can be considered as two parts: firstly estimating the transmitted signal using the received one, which is  $\hat{S} = \mathbf{C}_s (\mathbf{C}_s + \sigma_w^2 \mathbf{I}_M)^{-1} \mathbf{x}$ , and then multiplying it by the conjugated received signal. Its schematic diagram is shown in Figure 2.9.

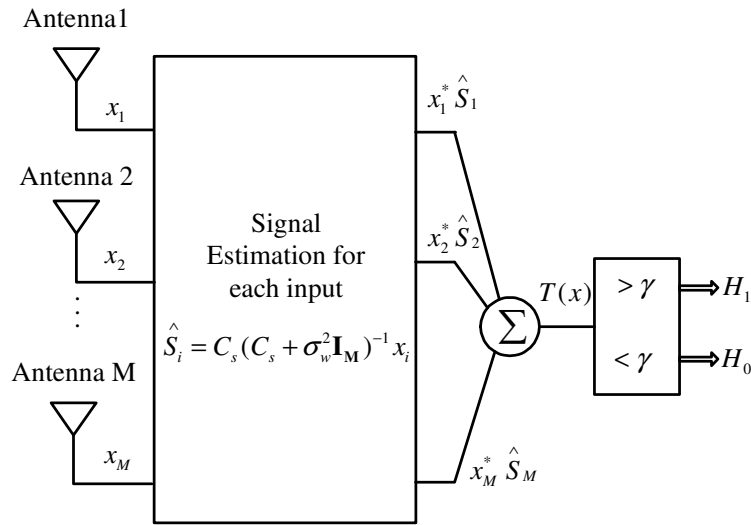


**Figure 2.9: LRT function schematic**

## 2.5 Signal distribution description

This thesis deals with the statistical signal processing in which the received signal distribution is analysed and the different detectors are optimized according to the received signal characteristics. In this section, the statistical functions called upon throughout the thesis are described.

### 2.5.1 Gaussian distribution

A Gaussian or normal random variable can be shown as  $x \sim N(\bar{x}, \sigma^2)$  where its probability distribution function (PDF) is defined as

$$p(x) = \frac{1}{\sqrt{2\pi\sigma^2}} \exp\left(-\frac{(x-\bar{x})^2}{2\sigma^2}\right). \quad 2-23$$

Here,  $\bar{x}$  and  $\sigma^2$  are the mean and variance of the received signal level, respectively. The cumulative distribution function (CDF) for a random variable describes the probability of the event that  $x$  does not exceed a specific value  $X$  and, for Gaussian distribution, is defined as

$$\begin{aligned}\Phi(X) &= \Pr(x \leq X) = \int_{-\infty}^x p(x) dx \\ &= \frac{1}{2} + \frac{1}{2} \operatorname{erf}\left(\frac{X - \bar{x}}{\sqrt{2\sigma^2}}\right)\end{aligned}\quad 2-24$$

where the error function (erf) is defined as

$$\operatorname{erf}(w) = \frac{2}{\pi} \int_0^w \exp(-y^2) dy. \quad 2-25$$

### 2.5.2 Rayleigh distribution

The Rayleigh distribution can be obtained mathematically as the PDF of  $x = \sqrt{x_1^2 + x_2^2}$ , where  $x_1$  and  $x_2$  are two independent zero mean Gaussian distributed signals with the variance of  $\sigma^2$ . Its PDF can be shown as

$$p(x) = \begin{cases} \frac{x}{\sigma^2} \exp\left(-\frac{x^2}{2\sigma^2}\right) & \text{for } x > 0 \\ 0 & \text{for } x < 0 \end{cases}. \quad 2-26$$

The PDF of a Rayleigh distribution is plotted in Figure 2.10. Here, the maximum value of the PDF corresponds to  $x = \sigma$  and it is equal to  $\exp(-0.5)/\sigma = 0.6065/\sigma$ . The mean value of a Rayleigh distributed signal can be quantified as

$$\bar{x} = E[x] = \int_0^{\infty} xp(x) dx = \sqrt{\frac{\pi\sigma^2}{2}} \approx 1.25\sigma. \quad 2-27$$

It can be shown that the variance or the average power of the received signal can be determined by (Blaunstein & Andersen 2002)

$$\sigma_x^2 = \sigma^2 \left(2 - \frac{\pi}{2}\right) \approx 0.429\sigma^2. \quad 2-28$$

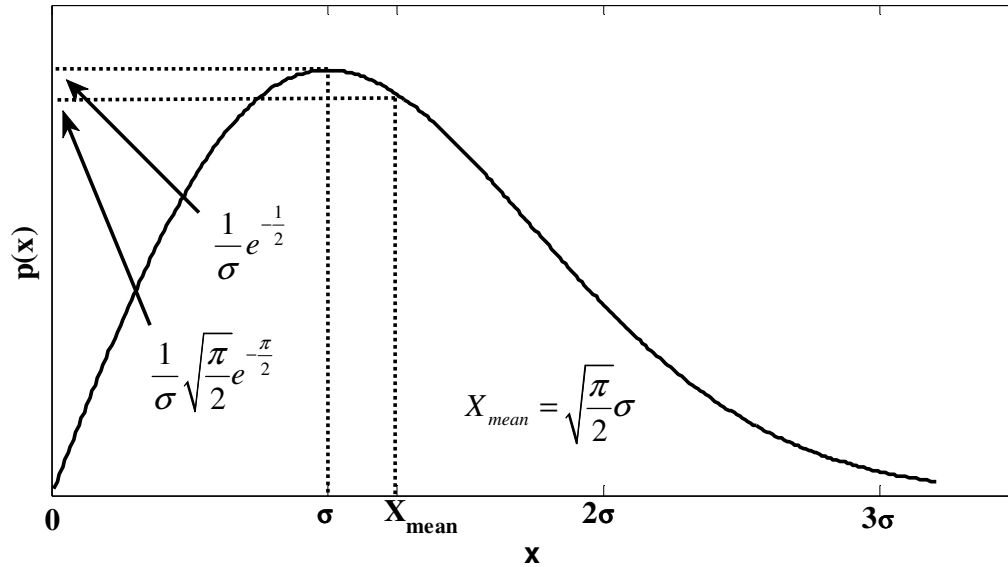


**Figure 2.10 Rayleigh probability distribution function**

Hence, the rms value of a Rayleigh distributed signal  $x$  defined as the square root of  $2\sigma_x^2$  is

$$rms = \sqrt{2}\sigma \approx 1.414\sigma . \quad 2-29$$

These parameters are shown in the Figure 2.10.

From the central limit theorem, when the number of scatters in a fading channel is large, the real and imaginary parts of the received baseband signal approaches a Gaussian distribution (Lee 1998). Practically, in wireless channels, the Rayleigh distribution is commonly used to describe the envelope of the sum of two quadrature zero mean Gaussian signals received in a small scale fading (Blaunstein & Andersen 2002).

### 2.5.3 Rician Distribution

Usually, in a wireless channel, the line of sight (LOS) signal arrives to the antenna along with the multipath components. The LOS component as a dominant part of the

received signal significantly changes the final received signal distribution. In this case two quadrature components of the received signal are no longer zero mean and the resultant envelope carries a Rician distribution.

Mathematically, the Rician distribution is the PDF of  $x = \sqrt{x_1^2 + x_2^2}$ , where  $x_1 \sim N(\mu_1, \sigma^2)$  and  $x_2 \sim N(\mu_2, \sigma^2)$  are two independent signals. Its PDF can be formulated as

$$p(x) = \begin{cases} \frac{x}{\sigma^2} \exp\left(-\frac{x^2 + \mu^2}{2\sigma^2}\right) I_0\left(\frac{\mu x}{\sigma^2}\right) & \text{for } x > 0 \\ 0 & \text{for } x < 0 \end{cases}, \quad 2-30$$

where  $\mu^2 = \mu_1^2 + \mu_2^2$  and  $I_0(\cdot)$  is the modified Bessel function of the first kind and zero order, formulated as (Kay 1998)

$$I_0(u) = \int_0^{2\pi} \exp(u \cos \theta) \frac{d\theta}{2\pi}. \quad 2-31$$

To estimate the contribution of each dominant and multipath component in the final distribution, the  $K$  factor is introduced as (Colburn et al 1998)

$$K = \frac{\text{LOS component power}}{\text{Multipath component power}} = \frac{\mu^2}{2\sigma^2}. \quad 2-32$$

It should be noted that the Rayleigh distribution is a special case of the Rician one when no dominant component is available, that is  $K=0$ . In Figure 2.11, the Rician distributions for various  $K$  factors are depicted. For lower  $K$  factors the fades with a high probability are deep, whereas for higher  $K$  values the fades are shallow and the PDF leads to a Gaussian distribution.

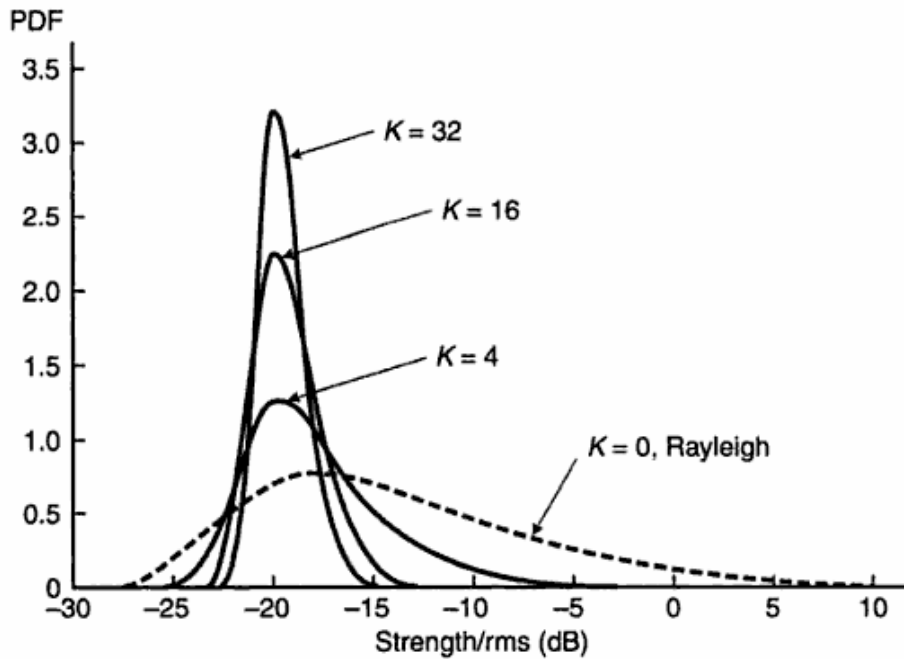


**Figure 2.11: Rician distributions for various  $K$  factors (Blaunstein & Andersen 2002)**

#### **2.5.4 Chi-squared distribution**

The chi-squared distribution is defined here since it is going to be referred in this thesis frequently. The chi-squared distribution with  $\nu$  degrees of freedom denoted as  $\chi^2_\nu$  arises as the distribution of a sum of the squares of  $\nu$  independent and identically distributed Gaussian random variables. The *central* chi-squared distribution with  $\nu$  degrees of freedom resulting from  $\nu$  independent and identically distributed (IID) standard zero mean Gaussian random variables with unit standard deviation is defined mathematically as

$$p(x) = \begin{cases} \frac{1}{2^{v/2} \Gamma(v/2)} x^{\frac{v}{2}-1} \exp\left(-\frac{x}{2}\right) & x > 0 \\ 0 & x < 0 \end{cases}. \quad 2-33$$

The  $\Gamma(u)$  is Gamma Function defined as

$$\Gamma(u) = \int_0^{\infty} t^{u-1} \exp(-t) dt. \quad 2-34$$

A *non-central* chi-squared distribution is as a result of summing the squares of independent nonzero mean Gaussian random variables. That is, if  $x = \sum_{i=1}^v x_i^2$  where  $x_i \sim N(\mu_i, 1)$ , the  $x$  carries non-central chi-squared distribution with  $v$  degrees of freedom and non-centrality parameter  $\lambda = \sum_{i=1}^v \mu_i^2$ . Its PDF can be formulated as

$$p(x) = \begin{cases} \frac{1}{2} \left(\frac{x}{\lambda}\right)^{\frac{v-2}{4}} \exp\left(-\frac{1}{2}(x+\lambda)\right) I_{\frac{v}{2}-1}(\sqrt{\lambda x}) & x > 0 \\ 0 & x < 0 \end{cases}. \quad 2-35$$

where  $I_r(u)$  is the  $r$ th modified Bessel function of the first kind.

Practically, the square of the envelope of the received signal carries a chi-squared distribution with two degrees of freedom, if the quadrature components carry a Gaussian distribution. For zero mean Gaussian received signals, it can be denoted as (Kay 1998)

$$x \sim CN(0, \sigma^2) \Rightarrow |x|^2 \sim \frac{1}{\sigma^2} \chi_2^2\left(\frac{x}{\sigma^2}\right). \quad 2-36$$

There are some more special distributions that are as a result of the combination of defined distributions that are not discussed here. For more information, the reader can refer to Blaunstein & Andersen (2002) and Rappaport (2002).

## **2.6 Summary**

In this chapter, the indoor fading channel characteristics were discussed and it was shown that diversity systems can improve the overall signal detectability and reduce fade margins. The properties of two diversity systems for indoor fading mitigation named polarization and spatial diversity systems were investigated. The polarization diversity structure as the main objective of this thesis has been discussed in details. The spatial diversity was introduced as well and its structure and properties were compared with these of the polarization diversity. The GPS signal architecture was introduced and the well-known combining methods structure for combining captured signals through diversity branches was defined. Finally, different distributions that signals in indoor environments experience were introduced.

### Chapter Three: GPS signal polarization

The GPS signals are transmitted in the form of radio frequency (RF) electromagnetic (EM) waves with right hand circularly polarization and can be fully characterized by their amplitude, phase and frequency. In this chapter, the electromagnetic wave polarization definition and the GPS signal model are explained. The power loss for a transmitted RHCP signal due to antenna misalignment is formulated for different types of antennas. In addition, the GNSS signal behaviour and characteristics in indoor environments are discussed in details and it is shown that the GPS signal is reformed by reflection in high multipath areas and its polarization changes.

#### 3.1 Electromagnetic wave polarization

According to the “IEEE standard definitions of terms for antennas”, the polarization of a radiated signal is defined as “that property of a radiated electromagnetic wave describing the time varying direction and relative magnitude of the electric field vector.” Generally, all electromagnetic (EM) waves can be formulated as an elliptically polarized signal (Balanis 2001). A signal is defined as elliptically polarized if the tip of the electric field intensity vector ( $\mathbf{E}$ ) traces out an ellipse in space. An elliptically polarized wave with an angular frequency of  $\omega$  and a wavenumber of  $k$ , which is propagating along with the  $z$  direction, can be formulated as

$$E(z, t) = \hat{a}_x E_x(z, t) + \hat{a}_y E_y(z, t) \quad 3-1$$

where

$$\begin{aligned} E_x(z, t) &= E_{x0} \cos(\omega t - kz + \phi_x) \\ E_y(z, t) &= E_{y0} \cos(\omega t - kz + \phi_y) \end{aligned} \quad 3-2$$

and  $\hat{a}_x$  and  $\hat{a}_y$  are unit vectors of Cartesian coordinate system,  $E_{x0}$  and  $E_{y0}$  are the amplitude of perpendicular electric field vector components of the signal in the  $y$  and  $x$  direction and the  $\phi_x$  and  $\phi_y$  are their phase characteristic, respectively. In this equation, the total energy of the wave is shown in two orthogonal linear components with different magnitude and phase.

The linear and circular polarization waves can be considered as special cases of an elliptical wave. The signal is said to be linearly polarized if the electric field intensity vector ( $\mathbf{E}$ ) is oriented in a fixed direction perpendicular to the magnetic field intensity vector ( $\mathbf{H}$ ) and the propagation direction of  $z$ . In the Equations 3-1 and 3-2, the signal is linearly polarized if

$$d\phi = \phi_x - \phi_y = n\pi, \quad n = 0, 1, 2, \dots \quad 3-3$$

The wave is defined as circularly polarized when the tip of  $\mathbf{E}$  traces out a circle in the space. Theoretical speaking, according to the Equations 3-1 and 3-2, the sufficient and necessary conditions for circular polarized signals are

$$\begin{aligned} E_{x0} &= E_{y0} \neq 0 \\ |d\phi| &= |\phi_x - \phi_y| = \left(\frac{1}{2} + 2n\right)\pi, \quad n = 0, 1, 2, \dots \end{aligned} \quad 3-4$$

Figure 3.1 shows different signal polarization schemes.

Another property of the circular and elliptical electromagnetic waves is the electric field vector rotation direction. Depending on the phase difference of electric field components ( $E_x$  and  $E_y$ ), the sense of rotation is determined as either clockwise (CW) ( $d\phi > 0$ ) or counter-clockwise (CCW) ( $d\phi < 0$ ) viewed as the way travels away from the observer. Hence, the circular polarized signals can be divided in two categories:

clockwise or Right-Hand Circularly Polarized (RHCP) and counter-clockwise or Left-Hand Circularly Polarized (LHCP) signals as shown in Figure 3.2.

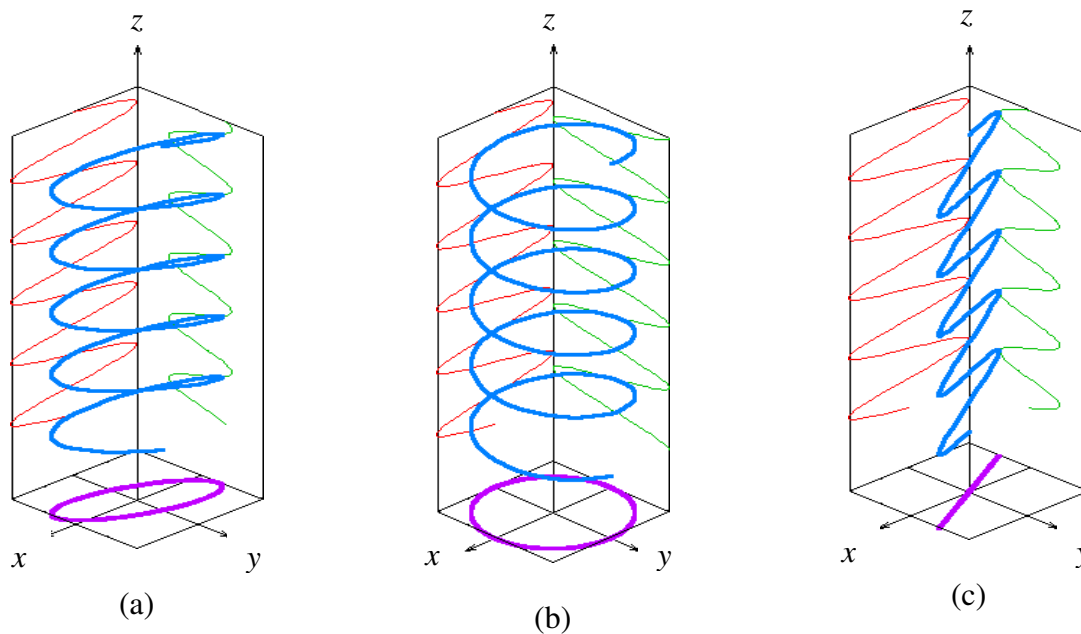


**Figure 3.1: Different signal polarization schemes: (a) elliptical polarization (b) circular polarization (c) linear polarization**

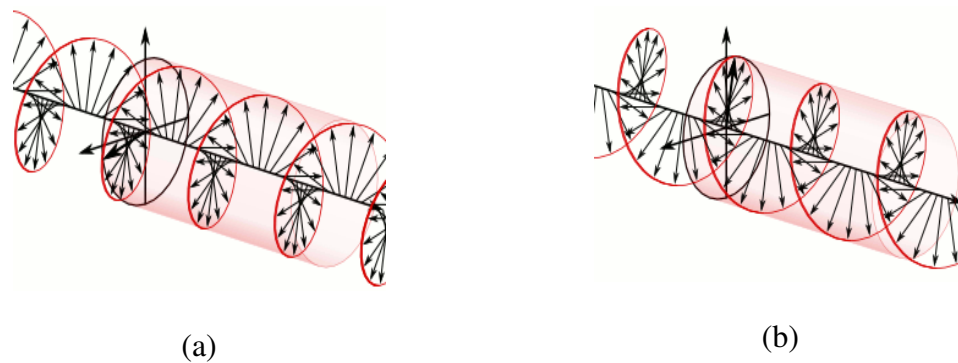


**Figure 3.2: (a) Right-Hand Circularly Polarized (RHCP) signal (b) Left-Hand Circularly Polarized (LHCP) signals**

Balanis (2001) shows that an elliptical polarized signal can be written as a combination of two RHCP and LHCP waves. He concludes that the tilted elliptical polarized signal of Equation 3-1 can be represented by RHCP and LHCP signal parameters as

$$\begin{aligned}
 d\phi = \phi_x - \phi_y & \begin{cases} \geq 0 & \left\{ \begin{array}{l} \text{for CW if } E_R > E_L \\ \text{for CCW if } E_R < E_L \end{array} \right. \\ \leq 0 & \left\{ \begin{array}{l} \text{for CW if } E_R < E_L \\ \text{for CCW if } E_R > E_L \end{array} \right. \end{cases} \\
 E_{x0} &= E_R + E_L \\
 E_{y0} &= E_R - E_L
 \end{aligned} \tag{3-5}$$

where  $E_R$  and  $E_L$  are the amplitude of RHCP and LHCP signals.

In satellite communications, and in GNSS applications, using the circular polarization is desirable since the position and orientation of the receivers' antenna on the earth varies with respect to the satellite and to deal with the effect of the ionosphere. However, the antenna misalignment may results in some loss that will discussed in the following section.

### 3.2 Polarization mismatch loss

When the polarization of the receiving antenna differs from the incoming wave, the maximum power of the incoming wave cannot be extracted by the antenna which leads to a polarization loss. This is called polarization mismatch loss.

The Polarization Loss Factor (PLF) can be quantified based on the antenna and wave unit vectors noted as  $\hat{\rho}_a$  and  $\hat{\rho}_w$ , respectively, as (Balanis 1989)

$$PLF = |\hat{\rho}_w \cdot \hat{\rho}_a|^2. \tag{3-6}$$

The transmitted GPS signals are right hand circularly polarized (RHCP). Let consider the arriving wave as a perfect RHCP wave with the following unit vector (Balanis 1989)

$$\hat{\rho}_{w,RC} = \frac{\hat{a}_x + j\hat{a}_y}{\sqrt{2}}, \quad 3-7$$

where the *RC* subscription stands for the right hand circular wave.

In order to analyze the polarization mismatch loss in GPS applications, losses due to receiving this signal by both circular and linear antennas are analyzed.

### 3.2.1 Circular antenna polarization mismatch loss

An RHCP antenna unit vector can be written as (Balanis 1989)

$$\hat{\rho}_{a,RC} = \frac{\hat{a}_x - j\hat{a}_y}{\sqrt{2}}. \quad 3-8$$

Let assume the incident signal is a perfect circular polarization and is radiated from a transmitter with the elevation angle of  $\theta$  (the angle of the arrived signal with the z-axis) as shown in Figure 3.3.

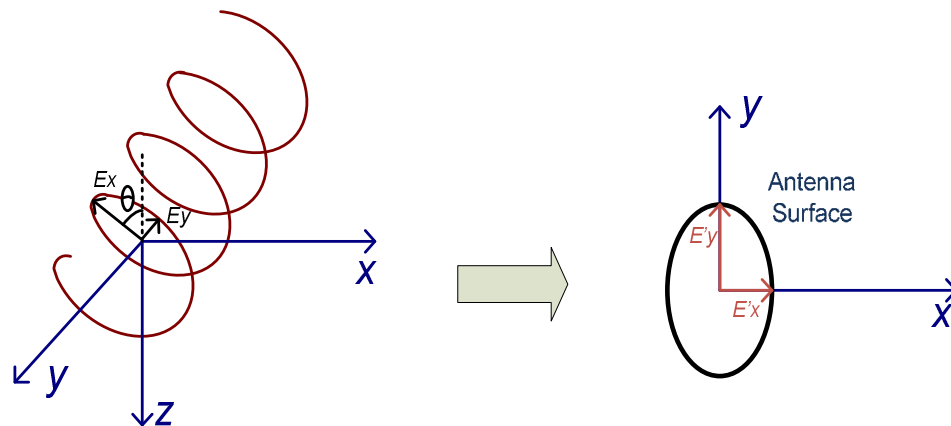


**Figure 3.3: Projection of an RHCP signal on antenna surface**

In this figure, the  $E_x$  and  $E_y$  are the electric field components of the radiated signal and  $E'_x$  and  $E'_y$  are the electric field components of the projected signal on the antenna surface. According to this figure and our assumption for the defined Cartesian coordinate system on the antenna surface, the  $E_y$  coincides with the  $y$ -axis and  $E_x$  makes the angle of  $90 - \theta$  degree with the  $x$ -axis. Therefore, they can be expressed as

$$E'_x = E_x \sin(\theta) \quad 3-9$$

and

$$E'_y = E_y \cdot \quad 3-10$$

It should be noted that there is a loss due to the projection of the signal on the antenna surface which can be expressed as the ratio of the projected signal ( $P_{Pr}$ ) magnitude to that of the original signal ( $P_{Os}$ ) as

$$L_{Pr} = \frac{P_{Pr}}{P_{Os}} = \frac{|\hat{a}_x \sin \theta + j\hat{a}_y|^2}{|\hat{a}_x + j\hat{a}_y|^2} = \frac{\sin^2 \theta + 1}{2} \quad 3-11$$

where  $P_{Pr}$  and  $P_{Os}$  stand for the projected wave and original signal respectively.

This loss is due to signal projection and will be considered in the total loss calculation. In addition to this, the projected signal is no longer RHCP and its unit wave vector can be expressed as

$$\hat{\rho}_{w,Pr} = \frac{\hat{a}_x \sin \theta + j\hat{a}_y}{\sqrt{1 + \sin^2 \theta}} \cdot \quad 3-12$$

Therefore, the final polarization mismatch loss for a projected RHCP signal which is radiated from a transmitter with an elevation angle of  $\theta$  and is received by an RHCP antenna, shown in Figure 3.3, can be expressed as

$$PLF_{RC} = \left| \hat{\rho}_{w,Pr} \cdot \hat{\rho}_{a,RC} \right|^2 = \frac{(\sin \theta + 1)^2}{2(1 + \sin^2 \theta)} \quad 3-13$$

and the total loss can be quantified as

$$L_{T,RC} = 10 \log(PLF_{RC} \times L_{Pr}) = 10 \log \frac{(\sin \theta + 1)^2}{4} \text{ dB}. \quad 3-14$$

According to this equation and as it was expected, when the signal is coming from overhead, 90 degree elevation angle, it will be encountered with 0 dB loss; however, up to 6 dB loss is expected for lower elevation angles.

Now, let assume that an LHCP signal is used to collect the received signal. The unit vector for an LHCP antenna can be written as

$$\hat{\rho}_{a,LC} = \frac{\hat{a}_x + j\hat{a}_y}{\sqrt{2}}. \quad 3-15$$

In a similar way, the total loss for an LHCP antenna can be formulated as

$$L_{T,LC} = 10 \log(PLF_{LC} \times L_{Pr}) = 10 \log \frac{(1 - \sin \theta)^2}{4} \text{ dB}. \quad 3-16$$

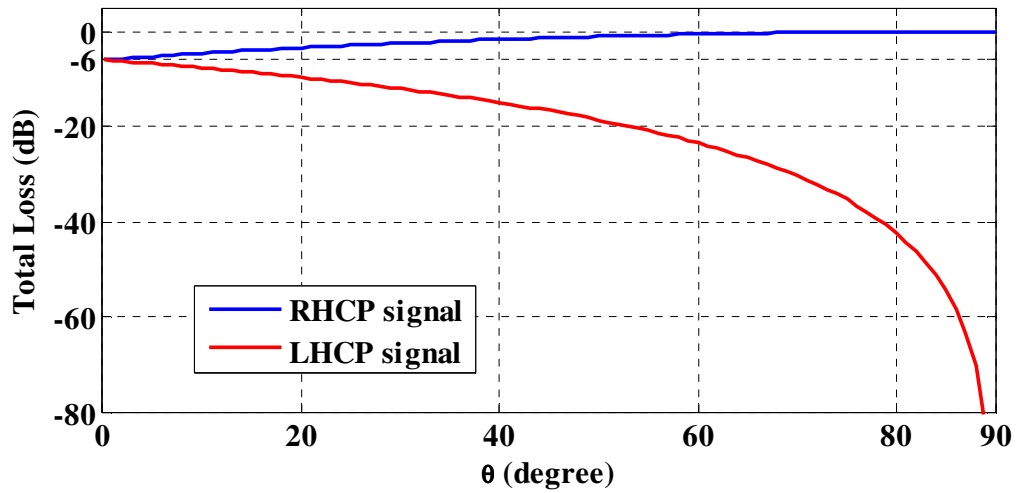


Figure 3.4: RHCP and LHCP signal loss received by an RHCP antenna

In this case, the perfect RHCP signal coming from overhead is not received by the LHCP antenna. In lower elevation angles, since the projected signal is no longer a pure RHCP signal, it faces lower resistance and loss. The results are depicted in Figure 3.4 for both RHCP and LHCP antennas.

### 3.2.2 Linear antenna polarization mismatch loss

Now consider another case in which the circularly polarized signals are received by a linear antenna. In this case, the spatial alignment of the antenna with respect to the signal direction of arrival plays a crucial role. In fact, while the polarization loss in a circular polarized antenna is independent of the azimuth angle, the latter is an important factor for linearly polarized antennas.

Let  $\varphi$  be the angle between the antenna and the projection of  $E_x$  on the antenna surface (Figure 3.5), the unit vector for a linear antenna,  $\hat{\rho}_{a,L}$ , can be written as

$$\hat{\rho}_{a,L} = \hat{a}_x \cos \varphi + \hat{a}_y \sin \varphi . \quad 3-17$$

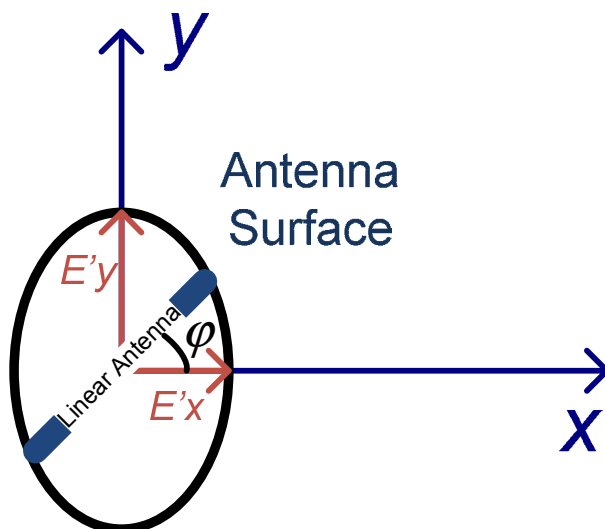


**Figure 3.5: Receiving an elliptical wave by a linear antenna**

Hence, the final polarization mismatch loss for a projected RHCP signal radiating from a transmitter with the elevation angle of  $\theta$  and azimuth angle of  $\varphi$  and received by a linear antenna can be quantified as

$$PLF_L = \left| \hat{\rho}_{w,Pr} \cdot \hat{\rho}_{a,L} \right|^2 = \frac{\cos^2 \varphi \sin^2 \theta + \sin^2 \varphi}{1 + \sin^2 \theta}. \quad 3-18$$

Therefore, the total loss due to both spatial misalignment and polarization mismatch for a linear antenna can be written as

$$L_{T,L} = PLF_L \times L_{Pr} = \frac{\cos^2 \varphi \sin^2 \theta + \sin^2 \varphi}{2}. \quad 3-19$$

The commercial dual polarized linear antennas for GNSS applications include two linear antennas mounted perpendicularly on the antenna surface and are called the horizontal and vertical antennas. Under open sky conditions, by assuming a static linear antenna directed toward north and placed on the horizon, the  $\varphi$  and  $\theta$  can be considered as the GNSS satellite azimuth and elevation angle, respectively.

The potential total loss between a pure RHCP signal and three sorts of described antennas including RHCP and linearly polarized antennas (both horizontal ( $\varphi = 0$ ) and vertical ( $\varphi = 90$ ) antennas) as a function of the angle of arrival are depicted in Figure 3.6 to Figure 3.8. Figure 3.6 shows that the linear antenna can receive more power than a circular one under some circumstances. In Figure 3.7 and Figure 3.8, the total loss for a specific  $\theta$  is shown. Here, the sine wave shape variation in the total loss as a function of changes in the satellite azimuth ( $\varphi$ ) is presented.

In this work, linear polarized antennas are used to build a linear polarization diversity structure. This structure can be called pattern diversity structure as well since two utilized linear antennas are placed on the horizon, perpendicular to each other. More

details regarding the effect of antenna misalignment and polarization mismatch loss will be discussed in the fifth chapter.

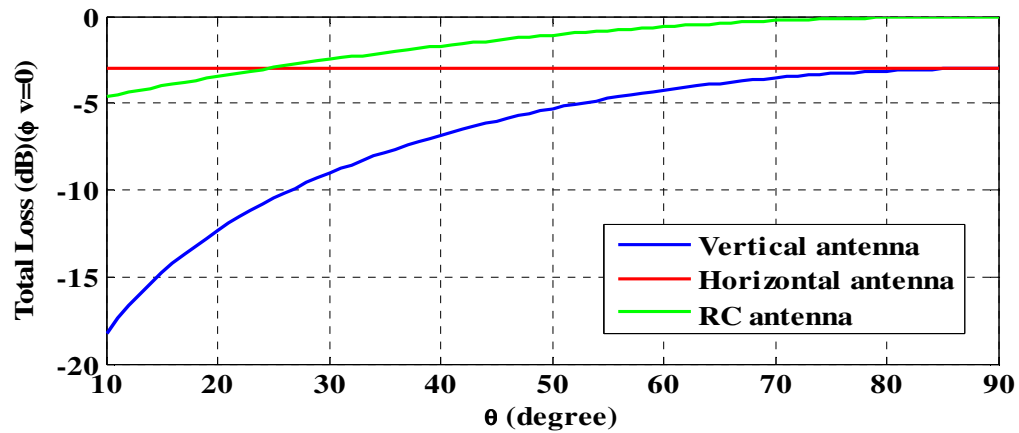


Figure 3.6: Total loss in receiving RHCP wave by a linear antenna for  $\phi = 0^\circ$

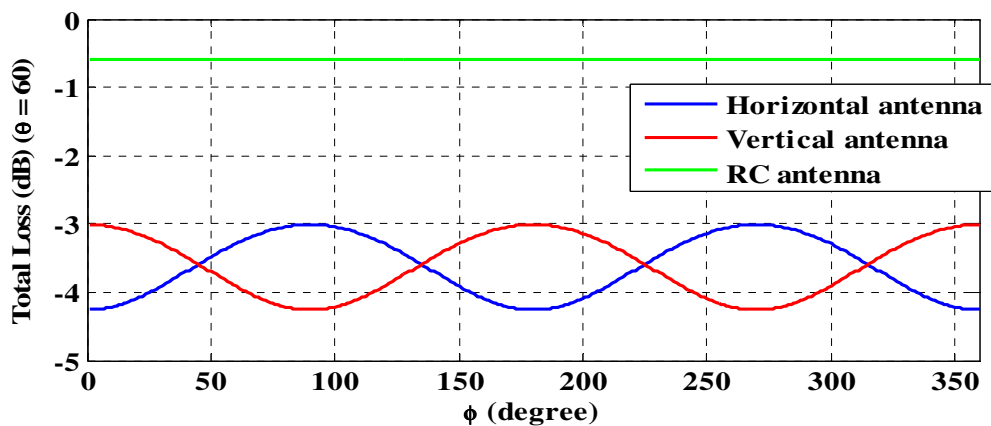


Figure 3.7: Total loss in receiving RHCP wave by a linear antenna for  $\theta = 60^\circ$

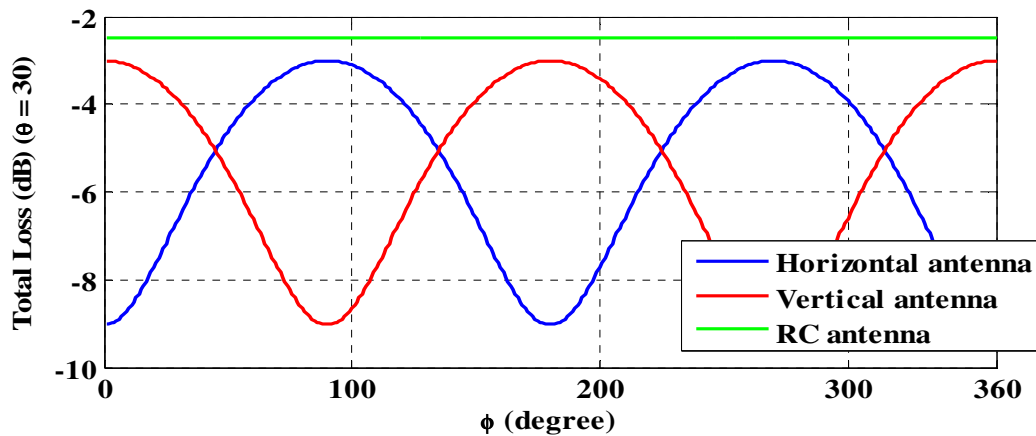


Figure 3.8: Total loss in receiving RHCP wave by a linear antenna for  $\theta = 30^\circ$

### 3.3 Indoor signal model

#### 3.3.1 GNSS signal polarization analysis in multipath environments

As mentioned, the GPS signals are right hand circularly polarized. However, the reflected signal polarization changes depending on the reflector type and the grazing angle (the angle at which the signal impinges on the reflector).

Let assume that a right hand circularly polarized GPS signal reaches the reflector with a grazing angle of  $\theta_g$ , as shown in Figure 3.9.

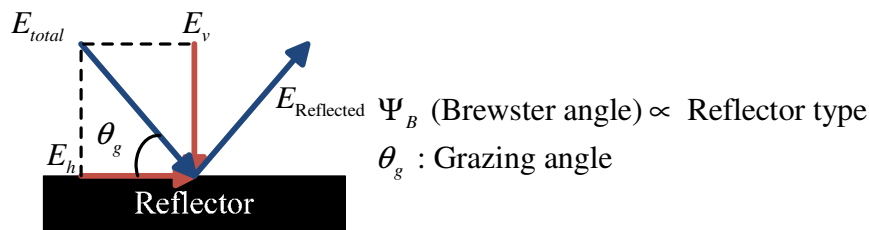


**Figure 3.9: Incoming EM signal to a reflector**

As described before, for a circularly polarized signal, the  $E$  vector is decomposed in to two orthogonal components,  $E_x$  and  $E_y$ , called horizontal ( $E_h$ ) and vertical ( $E_v$ ) components with the same absolute values. Since the parallel and perpendicular components of the reflection coefficient of the reflector are not equal (Rappaport 2002), the absolute value of the  $E$  field components in the reflected signal changes independently. Therefore, the circular polarity of the reflected GPS signal changes to elliptical. In addition to magnitude, the phase of each component changes depending on the Brewster angle,  $\Psi_B$ , (known as the polarization angle as well) as a property of the reflectors. After reflection, the phase of the horizontal component ( $E_h$ ) always changes by 180 degrees; however, that of the vertical component ( $E_v$ ) may change either by 0 or 180 degrees depending on whether the grazing angle is below or above the Brewster angle (Yang & Porter 2005). If the grazing angle is higher than the Brewster angle, the vertical

component phase changes by 180 degrees and the reflected signal carries right hand polarization. On the other hand, if the grazing angle is lower than the Brewster angle, the reflected signal has left hand polarization. Hence, the reflected wave may carry either left or right hand elliptical polarization based on the impinging angle. Yang & Porter (2005) has depicted the final signal polarization of a reflected signal for various grazing angle and specific Brewster angle (Figure 3.10). According to their analysis, the reflected waves have elliptical polarization including both RHCP and LHCP components. If the grazing angle of the signal is less than Brewster angle, which is defined as a property of the reflector type, the RHCP component of the reflected signal is stronger, whereas, if the grazing angle of LOS signal is greater than the Brewster angle, the LHCP component of the reflected signal will be stronger.

In indoor environments, since the signal is highly likely to be subject to reflections, the final received signals can be assumed to be elliptically polarized and, hence, include both RHCP and LHCP components.

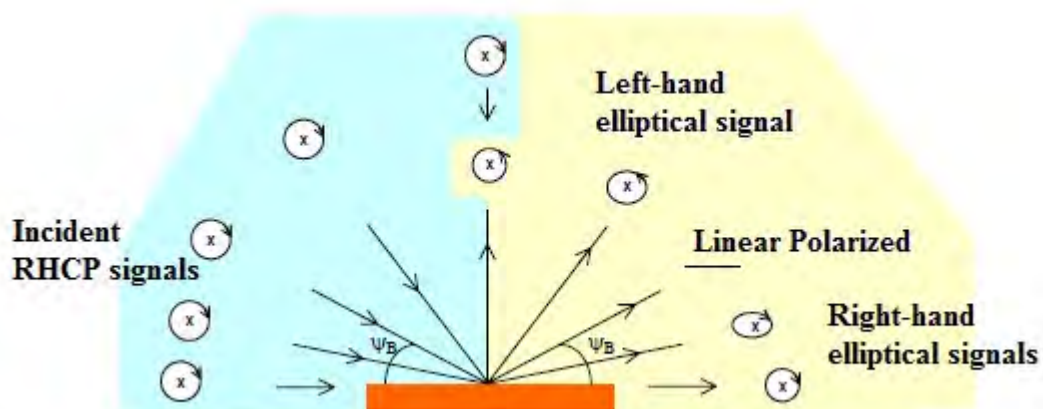


**Figure 3.10: GNSS signal polarization after reflection (Yang & Porter 2005)**

### 3.3.2 Characterizing fading channel

For indoor GNSS applications it can be shown that  $s_o(t)$  is sufficiently narrowband such that a flat fading model can be assumed (Rappaport 2002). It is also assumed that during signal snapshots  $T$ , the channel is temporally static in which case coherent integration results in processing gain.

From the central limit theorem, when the number of scatters in a fading channel is large, the distribution of the In-phase and Quadrature components of the received signal approaches a Gaussian distribution (Lee 1998). Blaunstein & Andersen (2002) explain that the received signal strength carries the Gaussian distribution only as a result of the random interference of a large number of incident signals with randomly distributed amplitude and phase. If the phase of incident signals are uniformly distributed over  $[0 \ 2\pi]$ , the received random signal may lead to a zero mean Gaussian random variable (Blaunstein & Andersen 2002).

In indoor environments, the receiver antenna receives signals from many reflectors. Therefore, the received signal is a complex sum of the signals reflected from various obstacles with different amplitude and phase characteristics. Since the phasor components of the incoming waves can be assumed statistically independent, the final envelope has either a Rayleigh or a Rician distribution depending on the mean of the received Gaussian signals, as described in Section 2.5. A Rayleigh scenario happens when the line-of-sight (LOS) signal does not exist or is attenuated significantly and no dominant signal is seen by the receiver. In this case the In-phase ( $x_I$ ) and Quadrature ( $x_Q$ ) components of processed signal have zero mean Gaussian distribution with a variance of  $\sigma^2$ . Therefore, the envelope of the received signal  $x_e$  is Rayleigh-distributed with a Probability Density Function (PDF) of

$$p(x_e) = \frac{x_e}{\sigma^2} \exp\left(-\frac{x_e^2}{2\sigma^2}\right). \quad 3-20$$

The Rician situation exists when there is a dominant component such as a LOS signal among the incoming waves. In this case, the components of the de-spread signal (In-phase and Quadrature ones) are no longer zero mean and the LOS signal as a dominant component power makes its PDF similar to a Rician one formulated as

$$p(x_e) = \frac{x_e}{\sigma^2} \exp\left(-\frac{x_e^2 + x_s^2}{2\sigma^2}\right) I_0\left(\frac{x_e x_s}{\sigma^2}\right). \quad 3-21$$

Here,  $x_s^2/2$  is the dominant component power. As explained in Section 2.5.3, the dominant to multipath signal power ratio for a Rician distribution known as the  $K$ -factor is normally used to quantify the Rician fading as (Colburn et al 1998)

$$K = 10 \log \frac{x_s^2}{2\sigma^2} \text{ dB}. \quad 3-22$$

Plotting the cumulative distribution function (CDF) of the Rician and Rayleigh functions illustrates that for small  $K$  factors, roughly less than 0 dB, the Rician distribution overlaps with the Rayleigh one (Figure 3.11). In other words, for small  $K$  factors, the propagation channel can be considered as a Rayleigh fading channel.

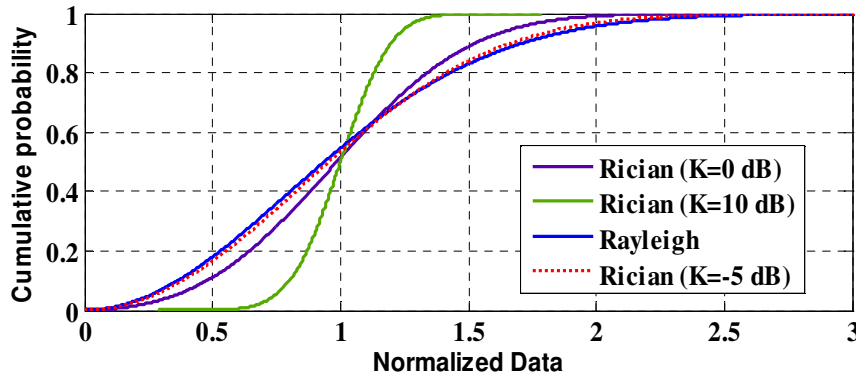


**Figure 3.11: Cumulative probability of received signals and fitted Rician and Rayleigh distributions**

### **3.4 Summary**

In this chapter, the electromagnetic wave polarization has been described and the losses due to antenna misalignments and orientation discussed. The GPS signals are right hand circularly polarized. Here, the losses due to antenna misalignment focused on RHCP signals received by different sorts of antennas including RHCP, LHCP and linear antennas. Since in this work a diversity structure using linear antennas are analyzed, the received signal power variation as a function of elevation angle and azimuth was depicted in this chapter. In addition, the GPS signal behaviour in high multipath environments is discussed here and it was shown that the GPS signals in indoor environments are no longer pure RHCP signals and that they are elliptically polarized which is a combination of both RHCP and LHCP ones.

## Chapter Four: Diversity Systems Performance Evaluation

The main focus of this work is to combine the received signal through two antennas with relatively orthogonal polarization in order to improve the signal detection performance in dense multipath environments. In the previous chapters the polarization diversity and indoor signal model were described. Herein the signal detection performance utilizing a diversity system is considered. The likelihood Ratio Test (LRT) for a diversity system with two input branches is explained in detail and its performance under various signal conditions in indoor environments is quantified theoretically. In order to assess the performance of the proposed method, some metrics including diversity gain, cross correlation between diversity branches and average SNR are introduced and studied.

### 4.1 Likelihood ratio test (LRT) function

Assume a *binary hypothesis test* that includes two hypotheses, namely the *null hypothesis* and the *alternative hypothesis*, referred as  $H_0$  and  $H_1$  respectively. The input signal probability function vary under different conditions of  $H_1$  and  $H_0$  noted as  $p(x;H_1)$  and  $p(x;H_0)$  respectively. The notation  $p(x;H_i)$  stands for the probability function of  $x$  under  $H_i$  condition. The detection problem is to distinguish between these two conditions. According to Kay (1998), two types of errors may happen in the detector: deciding  $H_1$  while  $H_0$  is true (type I error: noted as  $Pr(H_1;H_0)$ ) and deciding  $H_0$  while  $H_1$  is true (type II error: noted as  $Pr(H_0;H_1)$ ). The notation  $Pr(H_i;H_j)$  indicates the probability of deciding  $H_i$  while  $H_j$  is true. The type I error is called a false alarm and its probability is known as the probability of false alarm ( $P_{FA}$ ). It is not possible to reduce both error probabilities and the approach in order to design an optimum detector is to keep the probability of false

alarm fixed and reduce the other one (Kay 1998). Minimizing the type II error ( $Pr(H_0;H_1)$ ) is equivalent to maximizing the  $Pr(H_1;H_1)$  defined as

$$Pr(H_1;H_1) = 1 - Pr(H_0;H_1). \quad 4-1$$

This probability is called probability of detection denoted as  $P_D$ . The  $P_{FA}$  and  $P_D$  can be quantified as (Kay 1998)

$$P_{FA}(\gamma) = \int_{x=\gamma}^{\infty} p(x;H_0)dx \quad 4-2$$

and

$$P_D(\gamma) = \int_{x=\gamma}^{\infty} p(x;H_1)dx \quad 4-3$$

respectively. Here,  $\gamma$  is known as a threshold for the detector in order to achieve the maximum efficiency. In Figure 4.1, as an example, the signal PDF under  $H_1$  and  $H_0$  for a DC signal with amplitude 2 in a Gaussian noise is depicted. For a given  $\gamma$  the probabilities of detection and false alarm are highlighted in the figure. In summary, it is desired to maximize the probability of detection subject to the constraint  $P_{FA} = \alpha$ . Therefore, the detection performance of a receiver can be evaluated by the probability of false alarm and the probability of detection. To accomplish this evaluation, the probability of detection is quantified for various constraints on the probability of false alarm. Hence,  $P_D$  is plotted as a function of  $P_{FA}$ . This is called a *Receiver Operating Characteristics* (ROC) curve. Figure 4.2 shows a ROC curve for two different detector structures. For a given design point of  $P_{FA}$  two different receivers provide different values for  $P_D$  denoted as  $P_{D(1)}$  and  $P_{D(2)}$ . As shown, the first detector carries the higher detection probability and results in a higher detection performance.

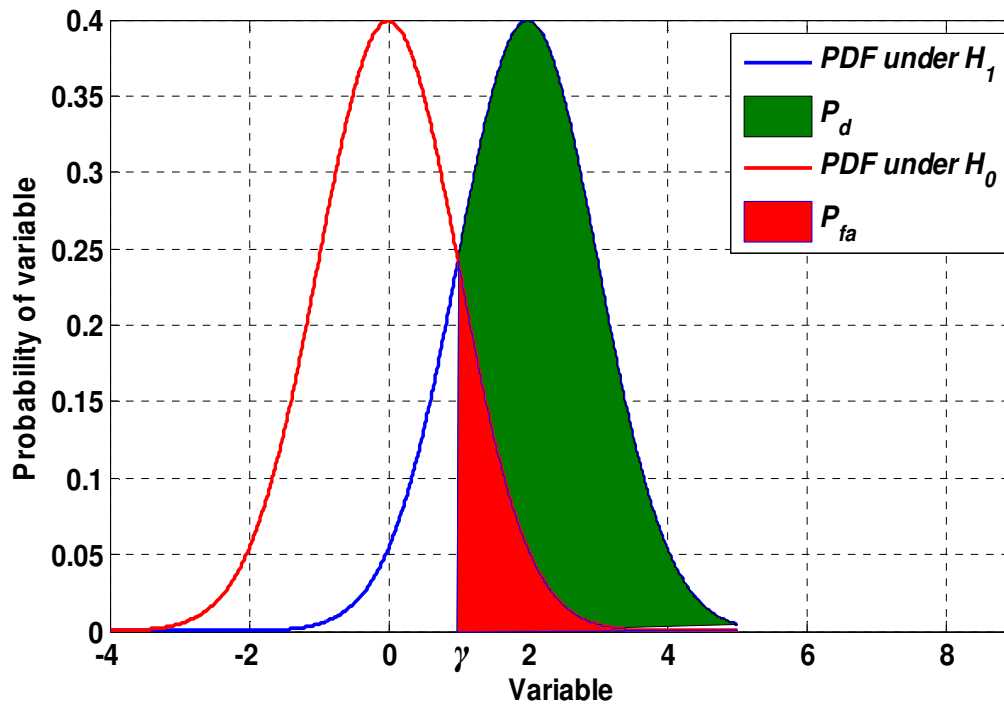


Figure 4.1: Binary hypothesis probabilities

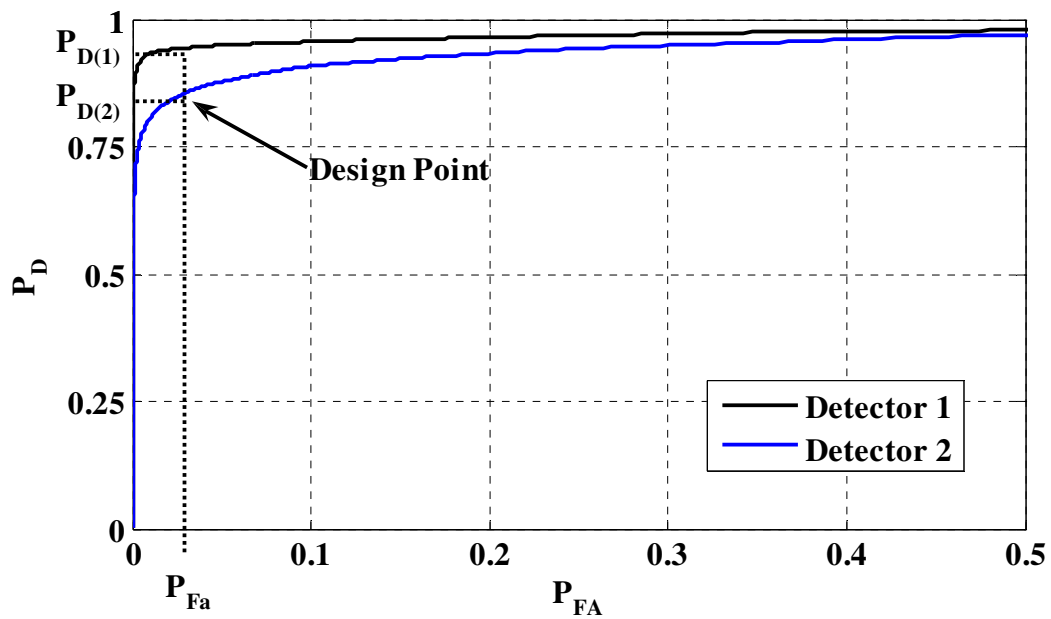


Figure 4.2: ROC curve for two types of detector

The *Neyman-Pearson* theorem is defined to maximize the probability of detection for a given  $P_{FA} = \alpha$ , decide  $H_1$  if (Kay 1998)

$$L(x) = \frac{p(x; H_1)}{p(x; H_0)} > \gamma \quad 4-4$$

where the threshold  $\gamma$  is found from Equation 4-2. This function (Equation 4-4) is known as the *Likelihood Ratio Test* (LRT) function.

## 4.2 Diversity gain

The effectiveness of a diversity system is usually evaluated by a quantity known as the diversity gain. The diversity gain is defined as the excess in the required input SNR for a single antenna scheme to achieve the same probability of detection as the combining scheme for a specific probability of false alarm. The most significant factor which characterizes the performance of each diversity structure is the correlation coefficient between the received signals in different diversity branches. In fact, the efficiency of a diversity technique depends on the independent occurrence of deep fading in diversity branches (Narayanan et al 2004). Another important factor is the average Signal-to-Noise Ratio (SNR) in each diversity branch. Schwartz et al (1966) show that the imbalance power in diversity branches leads to a lower overall diversity gain. Another important factor is the method by which the signals in the diversity branches are combined. A wide and comprehensive analysis of different diversity schemes including selection, equal gain and maximal ratio is presented by Turkmani et al (2004) using 924 measurements in various locations. They derive experimental equations for diversity gain of various combiners as a function of the input power difference and signals cross correlation. According to their results, the maximum ratio method catches the highest diversity gain

and the selection combining method leads to the lowest diversity gain among the analyzed methods.

As defined, diversity gain is the required input SNR for a single antenna scheme to achieve the same probability of detection as the combining scheme for a specific probability of false alarm as a design point. Assume two detectors, where the first one uses only a single antenna as input and the second one selects the test statistics based on the combination of the two independent input branches. For a given target detection performance in terms of the probability of false alarm and detection, the diversity gain of the combiner relative to the processed single signal is quantified as

$$G = \frac{SNR_s}{SNR_{Combiner}}, \quad 4-5$$

where  $SNR_s$  and  $SNR_{Combiner}$  signify the SNR output of these detector with the same design point; hence a specific design point should be determined from empirical data in advance, as shown in Figure 4.2.

### 4.3 Two antenna detection procedure

According to Figure 4.1 to increase the probability of detection for a given set of input signals, one can increase the distance between  $p(x;H_0)$  and  $p(x;H_1)$  by increasing the average SNR or change its probability function which can be accomplished by using a diversity system. In this work, the main idea is to combine two independent signals received from two perpendicular polarized antennas, (e.g. RHCP and LHCP). In order to combine the input branches (two antennas) and implement a detector for the received GPS signals, the LRT test function is utilized in this work. As described briefly in Chapter 2, the detection problem is to find a moment in each code and Doppler search

where the incoming signal and the locally generated one are synchronized. Two hypotheses  $H_1$  and  $H_0$  are defined as

$$\begin{aligned} H_0 : x[m] &= w[m] & m = 0, 1, 2, 3, \dots, M-1 \\ H_1 : x[m] &= s[m] + w[m] & m = 0, 1, 2, 3, \dots, M-1 \end{aligned} \quad 4-6$$

Here,  $x[m]$  is the correlator output for  $T$  second coherent integration process,  $s[m]$  is the desired signal in which the code phase and Doppler of the incoming signal and the locally generated one are synchronized,  $w[m]$  is the embedded zero mean white complex Gaussian noise with a covariance matrix of  $C_w = \sigma_w^2 \mathbf{I}_M$  and  $M$  is the number of diversity branches. In a Rayleigh faded channel, the desired signal received at the antenna is a zero mean circular normal distribution with a covariance matrix of  $C_s$ . Therefore, the input signal probability function under different conditions of  $H_1$  and  $H_0$  is formulated as

$$\begin{aligned} p(x; H_0) &\sim CN(0, C_w) \\ p(x; H_1) &\sim CN(0, C_s + C_w) \end{aligned} \quad 4-7$$

Under these conditions, as mentioned in Chapter 2, the final test statistic becomes (Kay 1998)

$$T(\mathbf{x}) = \mathbf{x}^H C_s (C_s + \sigma_w^2 \mathbf{I}_M)^{-1} \mathbf{x}. \quad 4-8$$

In the dual polarized diversity system a general scenario for the received signal covariance matrix can be defined as

$$C_s = \begin{bmatrix} \sigma_{s_1}^2 & E(x_1 x_2^*) \\ E(x_2 x_1^*) & \sigma_{s_2}^2 \end{bmatrix}, \quad 4-9$$

where  $x_1$  and  $x_2$  are the correlator (despreader) output of input branches, the  $\sigma_{s_m}^2$  is the variance of  $x_m$  signal under  $H_1$  condition,  $(\bullet)^*$  is conjugate operator and  $E(x_1 x_2^*) = E(x_2 x_1^*)$ .

In order to simplify the final test statistic represented in Equation 4-8, the modal matrix  $V$ , a  $2 \times 2$  matrix formed with the eigenvectors of  $C_s$ , will be used to decorrelate the input signals with  $\mathbf{y} = V^T \mathbf{x}$ . Since the  $V$  matrix is composed of eigenvectors of  $C_s$ , there is  $V^H C_s V = \Lambda_s$ , where  $\Lambda_s$  is a matrix of eigenvalues of  $C_s$  and is formed as

$$\Lambda_s = \begin{bmatrix} \lambda_{s0} & 0 \\ 0 & \lambda_{s1} \end{bmatrix}, \quad 4-10$$

Therefore, the covariance matrix of  $\mathbf{y}$  becomes

$$\begin{aligned} C_y &= E[\mathbf{y}\mathbf{y}^H] = V^H C_x V \\ &= V^H (C_s + \sigma_w^2 I_2) V \\ &= V^H C_s V + \sigma_w^2 V^H V \\ &= \Lambda_s + \sigma_w^2 I_2 \end{aligned} \quad 4-11$$

By using the aforementioned equations and considering  $VV^H = 1$ , the final test statistic leads to the following function:

$$\begin{aligned} T(x) &= \mathbf{x}^H C_s (C_s + \sigma_w^2 I_2)^{-1} \mathbf{x} \\ &= \mathbf{x}^H V V^H C_s V V^H (C_s + \sigma_w^2 I_2)^{-1} V V^H \mathbf{x} \\ &= \mathbf{y}^H \Lambda_s (\Lambda_s + \sigma_w^2 I_2)^{-1} \mathbf{y} \\ \Rightarrow T(y) &= x_{LRT} = \sum_{m=0}^1 \frac{\lambda_{sm}}{\lambda_{sm} + \sigma_w^2} y_m^2 \end{aligned} \quad 4-12$$

Consequently, the final test statistic can be considered as a decorrelator following by a weighting section as is shown in Figure 4.3. Different conditions for input signals can be considered. In the next section, the detector performance under such conditions will be evaluated.

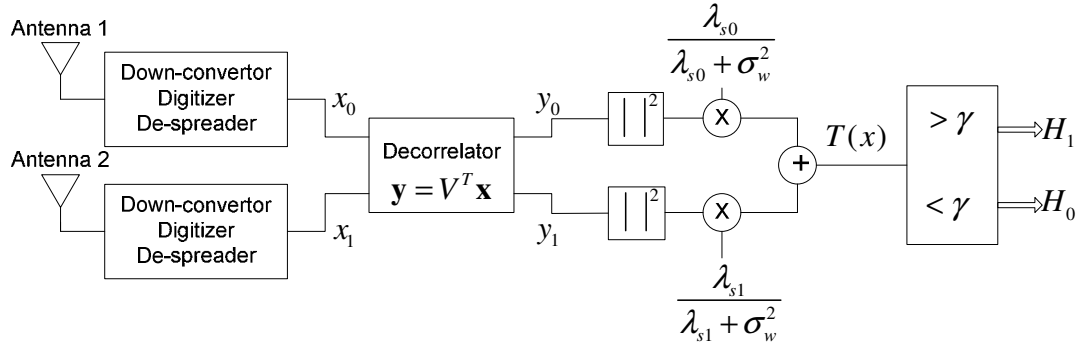


**Figure 4.3: LRT detector scheme for two antennas**

### 4.3.1 Performance evaluation

As discussed earlier, the detector performance is evaluated by the probabilities of false alarm and detection. As shown before the test statistics reduces to

$$T(y) = \sum_{m=0}^1 \frac{\lambda_{sm}}{\lambda_{sm} + \sigma_w^2} y_m^2. \quad 4-13$$

According to Equation 4-2 and 4-3, the probabilities of false alarm and detection can be shown to be

$$P_{FA}(\lambda) = \int_{y=\lambda}^{\infty} p(T(y); H_0) dy \quad 4-14$$

and

$$P_D(\lambda) = \int_{y=\lambda}^{\infty} p(T(y); H_1) dy. \quad 4-15$$

Here it is assumed that the channel is modeled by Rayleigh fading in which the decorrelated received signals components (In-phase ( $x_I$ ) and Quadrature ( $x_Q$ ) ones) carry zero mean Gaussian distributions defined as

$$\begin{aligned} x &= x_I + jx_Q \\ p(x_{I,Q}; H_0) &\sim N(0, C_w / 2) \\ p(x_{I,Q}; H_1) &\sim N(0, (C_s + C_w) / 2) \end{aligned} \quad 4-16$$

and  $x$  have the probability function stated in Equation 4-7 as

$$\begin{aligned} p(x; H_0) &\sim CN(0, C_w) \\ p(x; H_1) &\sim CN(0, C_s + C_w) \end{aligned} \quad 4-17$$

Thus, the probability function of  $y = V^T x$  is described as

$$\begin{aligned} p(y; H_0) &\sim CN(0, C_w) \\ p(y; H_1) &\sim CN(0, \Lambda_s + C_w) \end{aligned} \quad 4-18$$

since

$$E(y) = E(V^T x) = V^T E(x) = 0, \quad 4-19$$

and

$$C_y = E[yy^H] = V^H C_x V = \begin{cases} C_w & \text{under } H_0 \\ \Lambda_s + C_w & \text{under } H_1 \end{cases} \quad 4-20$$

Therefore, the quadrature components of  $y$  have zero mean Gaussian distributions and  $|y|^2$  results in central chi-squared distributions. Hence, the characteristics function of  $T(x)$  leads to the summation of two weighted central chi-squared distributions. According to Kay (1998), the probabilities of detection and false alarm for this model are quantified as

$$P_D = \int_{\gamma}^{\infty} \int_{-\infty}^{\infty} \frac{1}{(1 - j\lambda_{s0}\omega)(1 - j\lambda_{s1}\omega)} \exp(-j\omega t) \frac{d\omega}{2\pi} dt, \quad 4-21$$

and

$$P_{FA} = \int_{\gamma}^{\infty} \int_{-\infty}^{\infty} \frac{1}{(1 - 2j\alpha_0\omega)(1 - 2j\alpha_1\omega)} \exp(-j\omega t) \frac{d\omega}{2\pi} dt, \quad 4-22$$

where

$$\alpha_n = \frac{\lambda_{sn} \sigma_w^2}{\lambda_{sn} + \sigma_w^2}. \quad 4-23$$

To determine a closed form for  $P_{FA}$  and  $P_D$  in the case of distinctive eigenvalues, using a partial fraction expansion, it can be shown that (Kay 1998)

$$\prod_{m=0}^{M-1} \frac{1}{(1 - j\beta_m \omega)} = \sum_{m=0}^{M-1} \frac{B_m}{(1 - j\beta_m \omega)}, \quad 4-24$$

where

$$B_m = \prod_{\substack{k=0 \\ k \neq m}}^{M-1} \frac{1}{(1 - \frac{\beta_k}{\beta_m})}. \quad 4-25$$

Thus, for  $P_D$ , Equation 4-21 can be re-written as

$$\begin{aligned} P_D &= \int_{\gamma} \int_{-\infty}^{\infty} \frac{1}{(1 - j\lambda_{s0} \omega)(1 - j\lambda_{s1} \omega)} \exp(-j\omega t) \frac{d\omega}{2\pi} dt \\ &= \int_{\gamma} \int_{-\infty}^{\infty} \sum_{m=0}^1 \frac{B_m^D}{(1 - j\lambda_{sm} \omega)} \exp(-j\omega t) \frac{d\omega}{2\pi} dt \\ &= \int_{\gamma} \sum_{m=0}^1 \frac{B_m^D}{\lambda_{sm}} \exp\left(-\frac{t}{\lambda_{sm}}\right) dt \\ &= \sum_{m=0}^1 B_m^D \exp\left(-\frac{\gamma}{\lambda_{sm}}\right) \end{aligned}, \quad 4-26$$

where

$$B_0^D = \frac{\lambda_{s0}}{\lambda_{s0} - \lambda_{s1}}, B_1^D = \frac{\lambda_{s1}}{\lambda_{s1} - \lambda_{s0}}. \quad 4-27$$

After some manipulation, the  $P_D$  can be quantified as

$$P_D = \frac{\lambda_{s1} e^{-\frac{\gamma}{\lambda_{s1}}} - \lambda_{s0} e^{-\frac{\gamma}{\lambda_{s0}}}}{\lambda_{s1} - \lambda_{s0}}. \quad 4-28$$

Similarly, the  $P_{FA}$  can be computed as

$$P_{FA} = \frac{\alpha_1 e^{-\frac{\gamma}{\alpha_1}} - \alpha_0 e^{-\frac{\gamma}{\alpha_0}}}{\alpha_1 - \alpha_0} \quad 4-29$$

where

$$\alpha_n = \frac{\lambda_{sn} \sigma_w^2}{\lambda_{sn} + \sigma_w^2}. \quad 4-30$$

#### 4.4 Theoretical analysis of indoor environment

In this section, the performance evaluation of the LRT detector under various signal conditions in terms of correlation coefficient and the power difference between diversity branches is discussed.

##### 4.4.1 Single Antenna

In order to compare the performance of a diversity structure with a single antenna, the LRT procedure for a single antenna is explained and its probability of false alarm and detection are quantified below.

For a single antenna in a Rayleigh fading channel, the signal probability functions under  $H_1$  and  $H_0$  are expressed as

$$p(x; H_1) = \frac{1}{\pi(\sigma_s^2 + \sigma_w^2)} \exp \left[ \frac{-x^* x}{\sigma_s^2 + \sigma_w^2} \right] \quad 4-31$$

and

$$p(x; H_0) = \frac{1}{\pi\sigma_w^2} \exp \left[ -\frac{1}{\sigma_w^2} x^* x \right] \quad 4-32$$

respectively, where  $(\bullet)^*$  stands for a complex conjugate. Therefore, the likelihood ratio test is expressed as

$$L(\mathbf{x}) = \frac{p(x; H_1)}{p(x; H_0)} = \frac{\sigma_w^2}{(\sigma_s^2 + \sigma_w^2)} \exp \left[ -\frac{x^* x}{\sigma_s^2 + \sigma_w^2} + \frac{1}{\sigma_w^2} x^* x \right] > \gamma. \quad 4-33$$

The LRT function in this case results in

$$L(\mathbf{x}) = x^* x = |x|^2 > \gamma. \quad 4-34$$

Since the input signal is composed of two zero mean Gaussian distributions, Inphase and Quadrature components, defined as

$$\begin{aligned} x &= x_I + jx_Q \\ p(x_{I,Q}; H_0) &\sim N(0, \sigma_w^2 / 2) \quad , \\ p(x_{I,Q}; H_1) &\sim N(0, (\sigma_s^2 + \sigma_w^2) / 2) \end{aligned} \quad 4-35$$

the output of the LRT detector module ( $|x|^2$ ) is a central chi-squared distribution with 2 degrees of freedom (denoted as  $\chi_2^2$ ) under both  $H_0$  and  $H_1$  conditions:

$$\begin{aligned} \text{under } H_0 : x &\sim CN(0, \sigma_w^2) \Rightarrow |x|^2 = x_I^2 + x_Q^2 \sim \frac{1}{\sigma_w^2 / 2} \chi_2^2 \left( \frac{x}{\sigma_w^2 / 2} \right) \\ \frac{T(x)}{\sigma_w^2 / 2} &\sim \chi_2^2 \Rightarrow T'(x) \sim \chi_2^2(x) \\ \text{under } H_1 : x &\sim CN(0, \sigma_w^2 + \sigma_s^2) \Rightarrow |x|^2 \sim \frac{1}{(\sigma_w^2 + \sigma_s^2) / 2} \chi_2^2 \left( \frac{x}{(\sigma_w^2 + \sigma_s^2) / 2} \right) \quad 4-36 \\ \frac{T(x)}{(\sigma_w^2 + \sigma_s^2) / 2} &\sim \chi_2^2 \Rightarrow \frac{\frac{T(x)}{\sigma_w^2 / 2}}{1 + \frac{\sigma_s^2}{\sigma_w^2}} = \frac{\sigma_w^2}{\sigma_s^2 + \sigma_w^2} T'(x) \sim \frac{\sigma_w^2}{\sigma_s^2 + \sigma_w^2} \chi_2^2 \left( \frac{\sigma_w^2}{\sigma_s^2 + \sigma_w^2} x \right) \end{aligned}$$

As a result, from Section 2.5.3, the probability of false alarm and detection based on Equation 4-2 and 4-3 can be written as

$$\begin{aligned}
P_{FA(S)} &= \int_{\gamma}^{\infty} p(x; H_0) dx \\
&= \int_{\gamma}^{\infty} \frac{1}{2} e^{\left(-\frac{x}{2}\right)} dx = e^{-\frac{\gamma}{2}}
\end{aligned} \tag{4-37}$$

and

$$\begin{aligned}
P_{D(S)} &= \int_{\gamma}^{\infty} p(x; H_1) dx \\
&= \int_{\gamma}^{\infty} \frac{\sigma_w^2}{2(\sigma_s^2 + \sigma_w^2)} e^{\left(-\frac{\sigma_w^2}{\sigma_s^2 + \sigma_w^2} \times \frac{x}{2}\right)} dx = e^{-\frac{\gamma}{2(\Theta+1)}}
\end{aligned} \tag{4-38}$$

respectively, where  $\Theta = \sigma_s^2 / \sigma_w^2$  is defined as the average input SNR. The (S) subscript represents the single antenna condition. The  $P_D$  can be formulated as a function of  $P_{FA}$  as

$$P_{D(S)} = \exp\left(\frac{1}{\Theta+1} \text{Ln}(P_{FA(S)})\right). \tag{4-39}$$

#### 4.4.2 Uncorrelated equal power signals

Different conditions for the input signals of the diversity system will now be considered and the detector performance will be evaluated.

For equal power and uncorrelated signals, the signal covariance matrix components in Equation 4-9 becomes

$$\sigma_{s1}^2 = \sigma_{s2}^2 = \sigma_s^2 \tag{4-40}$$

and

$$E(x_1 x_2^*) = E(x_1^* x_2) = 0. \tag{4-41}$$

Thus the covariance matrix reduces to a diagonal matrix given as

$$C_s = \sigma_s^2 \begin{bmatrix} 1 & 0 \\ 0 & 1 \end{bmatrix}. \tag{4-42}$$

Consequently, the eigenvalues of the signal covariance matrix will be reduced and equal to  $\sigma_s^2$ . The final test statistic function defined in Equation 4-8 for equal power uncorrelated signals simplifies to

$$T(x) = \mathbf{x}^H C_s (C_s + \sigma_w^2 \mathbf{I}_M)^{-1} \mathbf{x} = \frac{\sigma_s^2}{\sigma_s^2 + \sigma_w^2} \mathbf{x}^H \mathbf{x} = \frac{\sigma_s^2}{\sigma_s^2 + \sigma_w^2} (|x_1|^2 + |x_2|^2), \quad 4-43$$

which is known as the Equal Gain (EG) combiner, defined as

$$T(x) = x_{EG} = |x_1|^2 + |x_2|^2. \quad 4-44$$

Its scheme is shown in Figure 4.4. The final test statistic function for equal gain combining for the proposed diversity scheme is the sum of four squared independent components with zero mean Gaussian distributions and equal variances. Therefore the final test statistic has a central chi-square distribution with four degrees of freedom denoted as  $\chi_4^2$  for both  $H_0$  and  $H_1$  hypotheses described as follows:

$$\begin{aligned} \text{under } H_0 : x_m &\sim CN(0, \sigma_w^2) \Rightarrow |x_m|^2 \sim \frac{1}{\sigma_w^2/2} \chi_2^2\left(\frac{x}{\sigma_w^2/2}\right) \\ \frac{T(x)}{\sigma_w^2/2} &\sim \chi_4^2 \Rightarrow T'(x) \sim \chi_4^2(x) \\ \text{under } H_1 : x_m &\sim CN(0, \sigma_w^2 + \sigma_s^2) \Rightarrow |x_m|^2 \sim \frac{1}{(\sigma_w^2 + \sigma_s^2)/2} \chi_2^2\left(\frac{x}{(\sigma_w^2 + \sigma_s^2)/2}\right) \\ \frac{T(x)}{(\sigma_w^2 + \sigma_s^2)/2} &\sim \chi_4^2 \Rightarrow \frac{T'(x)}{\Theta+1} \sim \frac{1}{\Theta+1} \chi_4^2\left(\frac{x}{\Theta+1}\right) \end{aligned} \quad 4-45$$

where  $\Theta = \sigma_s^2 / \sigma_w^2$  is the average input SNR in each diversity branch.

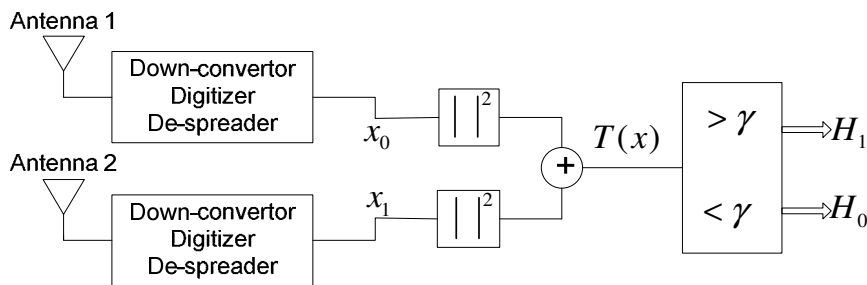


**Figure 4.4: Equal gain (EG) combiner scheme**

Consequently, according to Equations 4-2 and 4-3, the probability of false alarm and detection can be expressed as

$$\begin{aligned} P_{FA(EG)} &= \int_{\gamma}^{\infty} p(x; H_0) dx \\ &= \int_{\gamma}^{\infty} \frac{1}{4} x e^{-\frac{x}{2}} dx = \left(1 + \frac{\gamma}{2}\right) e^{-\frac{\gamma}{2}} \end{aligned} \quad 4-46$$

and

$$\begin{aligned} P_{D(EG)} &= \int_{\gamma}^{\infty} p(x; H_1) dx \\ &= \frac{1}{4(\Theta+1)^2} \int_{\gamma}^{\infty} x e^{-\frac{x}{2(\Theta+1)}} dx = \left(1 + \frac{\gamma}{2(\Theta+1)}\right) e^{-\frac{\gamma}{2(\Theta+1)}} \end{aligned} \quad 4-47$$

respectively.

#### 4.4.3 Correlated equal power signals

Assume two equal power input signals ( $\sigma_{s1}^2 = \sigma_{s2}^2 = \sigma_s^2$ ) correlated with a cross correlation of  $\rho$ . The cross correlation between received signals is quantified as

$$\rho = \frac{E(x_1 x_2^*)}{\sqrt{\text{var}(x_1) \text{var}(x_2)}} = \frac{E(x_1 x_2^*)}{\sqrt{\sigma_{s1}^2 \times \sigma_{s2}^2}} = \frac{E(x_1 x_2^*)}{\sigma_s^2}. \quad 4-48$$

Hence, the signal covariance matrix is reduced to

$$C_s = \sigma_s^2 \begin{bmatrix} 1 & \rho \\ \rho & 1 \end{bmatrix}. \quad 4-49$$

In this case, the LRT approach results in the Estimator Correlator (EC). From Section 4.3, the final test statistic function results in

$$\begin{aligned} T(x) &= \mathbf{x}^H C_s (C_s + \sigma_w^2 I)^{-1} \mathbf{x} \\ &= \sum_{m=0}^1 \frac{\lambda_{sm}}{\lambda_{sm} + \sigma_w^2} y_m^2 \end{aligned} \quad 4-50$$

and the  $\lambda_{s0}$  and  $\lambda_{s1}$  as the eigenvalues of the signal covariance matrix  $C_s$  are equal to

$$\begin{aligned}\lambda_{s0} &= \sigma_s^2(1+\rho) \\ \lambda_{s1} &= \sigma_s^2(1-\rho)\end{aligned}\quad 4-51$$

The final test statistic is the summation of two weighted chi-square functions with 2DOF and according to Section 4.3.1, the probabilities of false alarm and detection in this case can be calculated based on Equation 4-28 and 4-29 using the eigenvalues of  $C_s$ . After some manipulation, the final probabilities of detection and false alarm are expressed as

$$P_{D(EC)} = \frac{\sigma_s^2(1-\rho)e^{-\frac{\gamma}{\sigma_s^2(1-\rho)}} - \sigma_s^2(1+\rho)e^{-\frac{\gamma}{\sigma_s^2(1+\rho)}}}{2\sigma_s^2\rho} \quad 4-52$$

and

$$P_{FA(EC)} = \frac{\alpha_1 e^{-\frac{\gamma}{\alpha_1}} - \alpha_0 e^{-\frac{\gamma}{\alpha_0}}}{\alpha_1 - \alpha_0}, \quad 4-53$$

respectively, where

$$\alpha_0 = \frac{\sigma_s^2\sigma_w^2(1+\rho)}{\sigma_s^2(1+\rho) + \sigma_w^2}, \alpha_1 = \frac{\sigma_s^2\sigma_w^2(1-\rho)}{\sigma_s^2(1-\rho) + \sigma_w^2}. \quad 4-54$$

The probability of detection for a specific probability of false alarm ( $P_{FA}=0.01$ ) as a function of average input SNR ( $\Theta = \sigma_s^2 / \sigma_w^2$ ) and signal cross correlation coefficient ( $\rho$ ) is shown in Figure 4.5. For lower input SNR, the probability of detection decreases significantly by increasing the cross correlation coefficient. Besides, the diversity gain for estimator correlator as a function of cross correlation coefficient between input signals for various probabilities of detection and a fixed probability of false alarm ( $P_{FA}=0.01$ ) is shown in Figure 4.6. It goes without saying that diversity gain in estimator correlator is highly dependent on the determined design point (the target probability of detection and

false alarm) and the input signals cross correlation coefficient. A higher probability of detections and lower correlation coefficients leads to upper diversity gain.

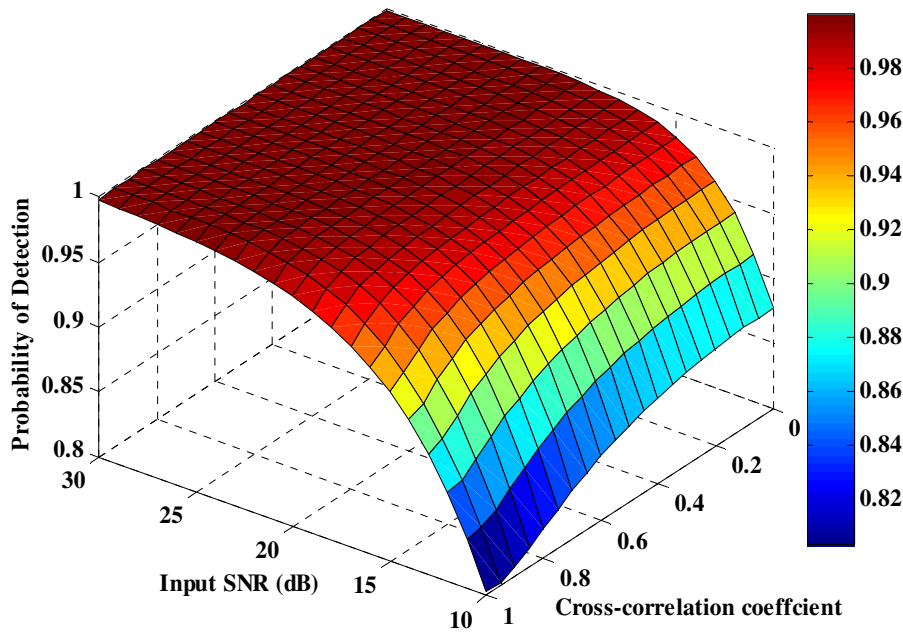


**Figure 4.5: Estimator correlator probability of detection as a function of input SNR and signal cross correlation coefficient ( $P_{FA}=0.01$ )**

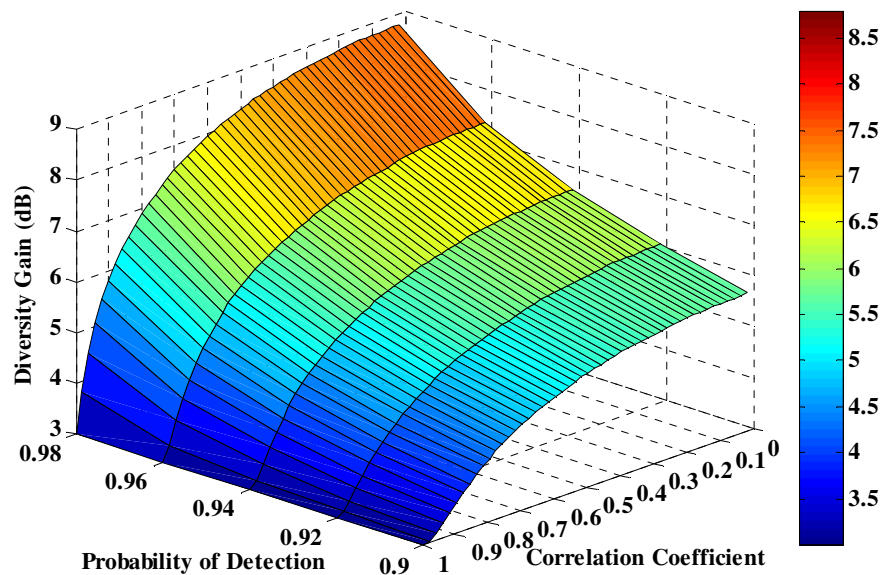


**Figure 4.6: Estimator correlator diversity gain as a function of probability of detection and cross correlation coefficient between input signals ( $P_{FA}=0.01$ )**

Let assume the case that two correlated signals are combined using the equal gain combining. In fact, since the estimator correlator implementation is more complex than the equal gain combiner and it requires prior information regarding the signal covariance matrix, combining correlated signals using an equal gain combiner and evaluating its performance is considered here. In this case the signal covariance matrix is considered as shown in Equation 4-49. The test statistic function will be an equal gain combiner as

$$x_{EG} = |x_1|^2 + |x_2|^2. \quad 4-55$$

The probability of false alarm is the same as the uncorrelated signals condition since under  $H_0$  the received signal is only noise. It can be written as

$$\begin{aligned} \text{under } H_0 : x_m \sim CN(0, \sigma_w^2) &\Rightarrow |x_m|^2 \sim \frac{1}{\sigma_w^2 / 2} \chi_2^2\left(\frac{x}{\sigma_w^2 / 2}\right) \\ T(x) = x_{EG} &\sim \frac{1}{\sigma_w^2 / 2} \chi_4^2\left(\frac{x}{\sigma_w^2 / 2}\right) \end{aligned} \quad 4-56$$

Therefore the probability of false alarm is expressed as

$$\begin{aligned} P_{FA(EG)} &= \int_{\gamma}^{\infty} p(x_{EG}; H_0) dx \\ &= \int_{\gamma}^{\infty} \frac{1}{4(\sigma_w^2 / 2)^2} x e^{-\frac{x}{\sigma_w^2}} dx = \left(1 + \frac{\gamma}{\sigma_w^2}\right) e^{-\frac{\gamma}{\sigma_w^2}} \end{aligned} \quad 4-57$$

Nielsen et al (2008) quantify the probability of detection for such combiner with described input signals as

$$P_D = \frac{\lambda_{x1} e^{-\frac{\gamma}{\lambda_{x1}}} - \lambda_{x0} e^{-\frac{\gamma}{\lambda_{x0}}}}{\lambda_{x1} - \lambda_{x0}}, \quad 4-58$$

where  $\lambda_{x0}$  and  $\lambda_{x1}$  are the eigenvalues of the  $C_x = C_s + \sigma_w^2 I_2$  and are equal to

$$\begin{aligned}\lambda_{x_0} &= (1 + \rho)\sigma_s^2 + \sigma_w^2 \\ \lambda_{x_1} &= (1 - \rho)\sigma_s^2 + \sigma_w^2\end{aligned}\quad 4-59$$

In the next section the performance of the estimator correlator and equal gain combiner will be compared under various conditions.

#### 4.4.3.1 Comparison of estimator correlator and equal gain combiner

Here, the performance of the estimator correlator (EC) and the equal gain (EG) combiners in the correlated signal case is evaluated. The ROC curves for both EC and EG combining when a pair of correlated signals with a correlation coefficient of 0.5 and 0.9 is applied on them are plotted in Figure 4.7. As shown, for 10 dB input signal power, both EC and EG combining for  $\rho = 0.5$  overlap, which shows that there is not any considerable difference between their performance in this case; however, for a higher correlation coefficient value ( $\rho = 0.9$ ), the EC combiner performance outweighs the EG one. Figure 4.8 shows that the detection performance difference of EC and EG depends on the input SNR as well. This figure shows the probability of detection difference between EG and EC for a specific probability of false alarm ( $P_{FA} = 0.001$ ) as a function of input SNR and correlation coefficient. In the case of low input SNRs (0 to 15 dB), for higher correlation coefficients the EC performs much better than the EG combiner and results in a higher probability of detection. According to this graph, for very low input SNRs, lower than 0 dB, the EC and EG combiner leads to the same performance, due to signal degradation caused by a very low SNR. Besides, Figure 4.9 shows the probability of detection as a function of input SNR for both EC and EG combiners, with a single antenna. Figure 4.9 shows the same performance for both EG and EC for defined design points.

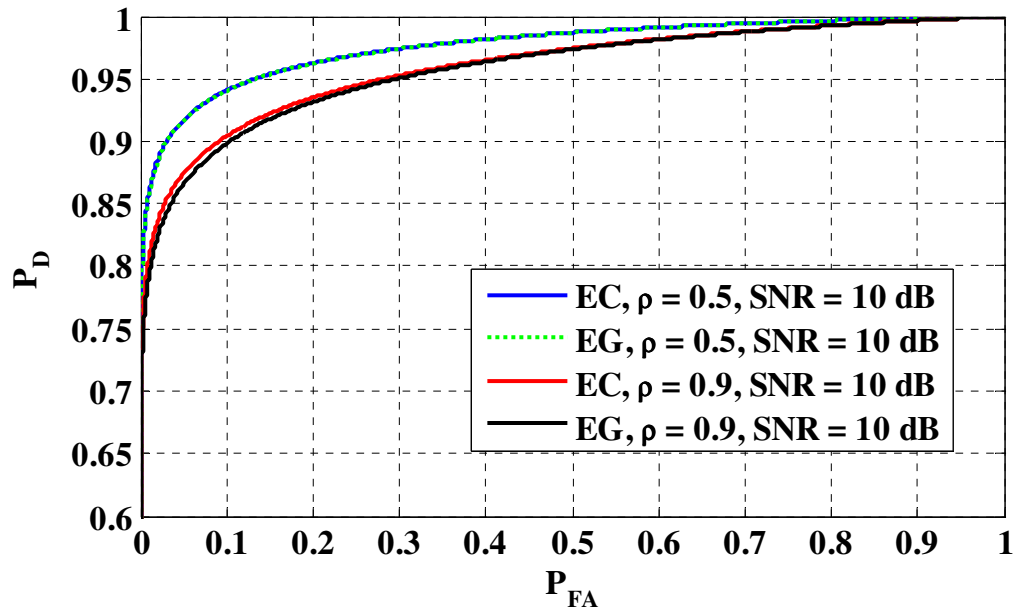


Figure 4.7: ROC curves for EC and EG with a correlated input signals, SNR = 10 dB

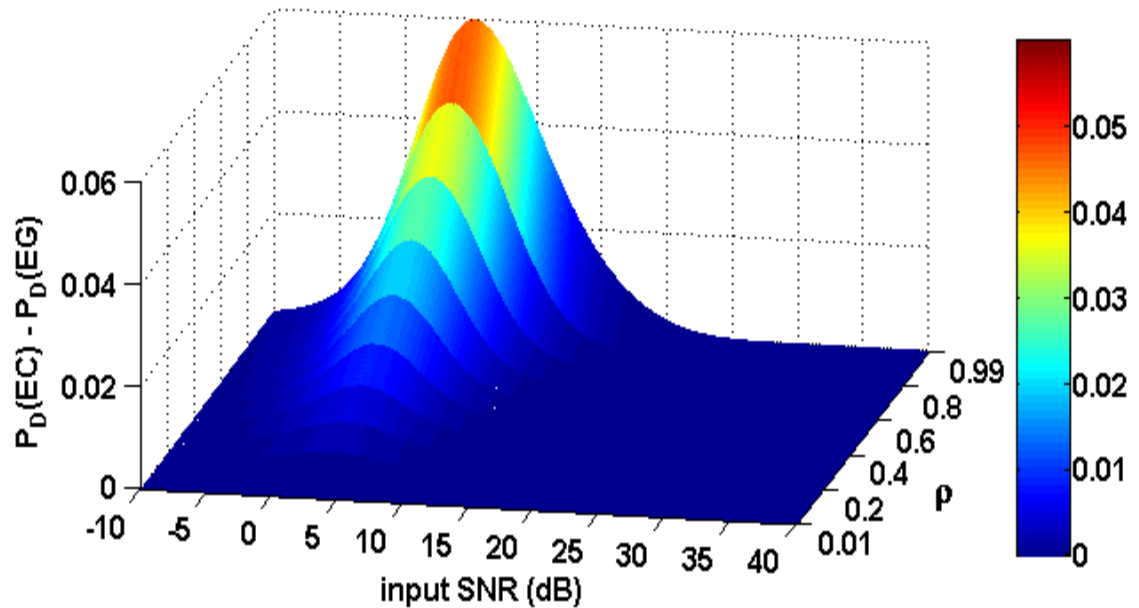
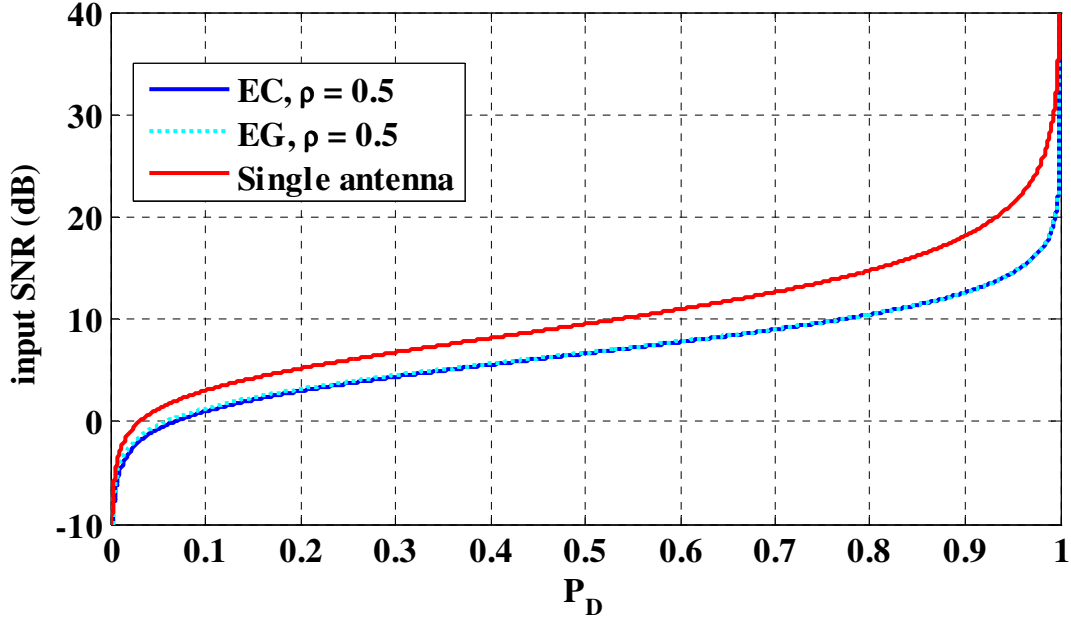


Figure 4.8: Probability of detection difference between EG and EC combiners for uncorrelated inputs ( $P_{FA}=0.001$ )



**Figure 4.9: Required input SNR vs. probability of detection for  $P_{FA}=0.001$**

In the final stage, the correlation coefficient versus diversity gain for a fixed probability of false alarm ( $P_{FA}=0.01$ ) and two different probabilities of detection is shown in Figure 4.10. As described, *Diversity Gain* (DG) is defined as the required input SNR for a single antenna receiver to achieve the same probability of detection as the combining scheme for a given probability of false alarm. Figure 4.10 implies that the higher correlation coefficient leads to lower diversity gain and it can be concluded that, for correlation coefficients of less than 0.3, almost full diversity gain can be achieved. In addition, it shows that the EC and EG combining methods result in the same performance for low correlation coefficients. The difference between the EC and EG combiner diversity gain is shown in Figure 4.11 as a function of correlation coefficient and design point (fixed  $P_{FA}=0.01$  and various  $P_D$ ). As it can be seen, for the defined design points, the EC and EG combiners have the same performance for correlated signals up to a cross-correlation coefficient of 0.6.

Since the estimator correlator and the equal gain combining have almost the same performance for low correlation coefficient values, the equal gain combining will be used as the combiner method due to its lower computational complexity.

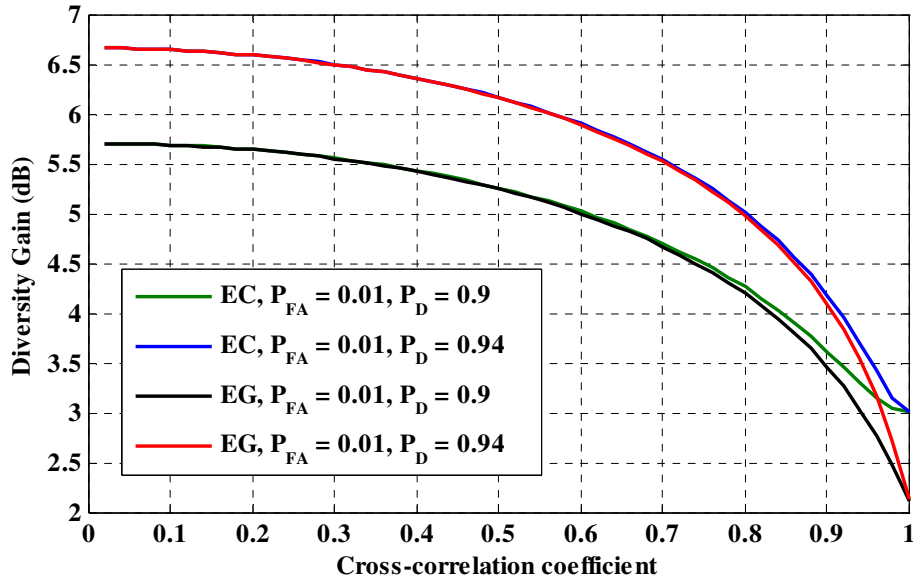


Figure 4.10: Diversity gain versus correlation coefficient for  $P_{FA}=0.01$

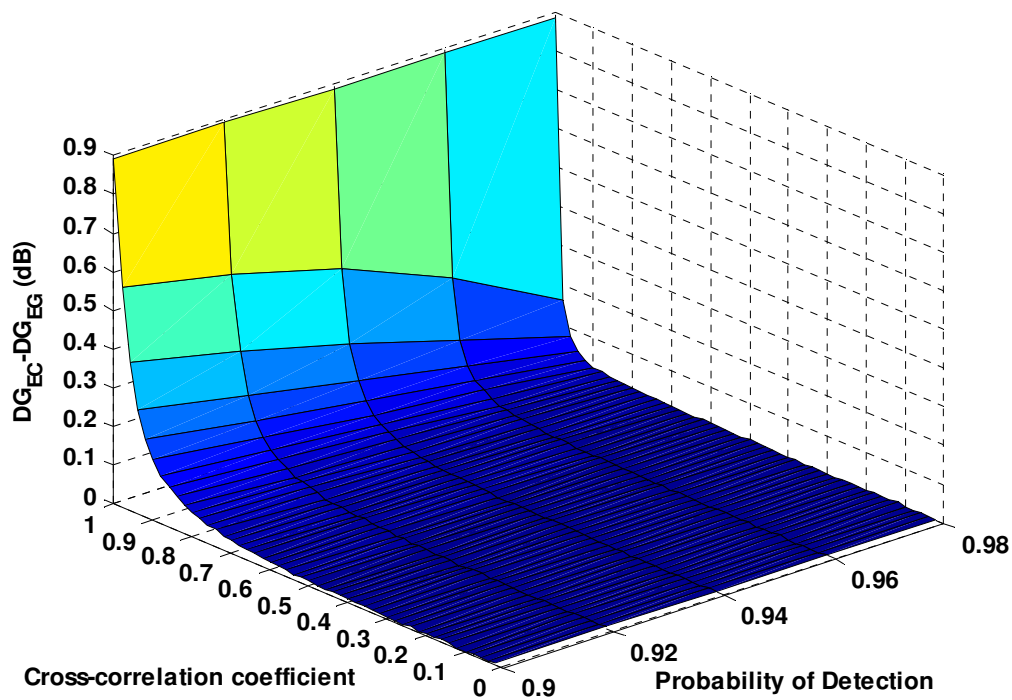


Figure 4.11: Diversity gain difference of EG and EC ( $P_{FA}=0.01$ )

#### 4.4.4 Uncorrelated and unequal power inputs

In case of uncorrelated inputs ( $E(x_1 x_2^*) = E(x_2 x_1^*) = 0$ ), the signal covariance matrix discussed in Section 4.3 reduces to

$$C_s = \sigma_s^2 \begin{bmatrix} 1 & 0 \\ 0 & r \end{bmatrix}. \quad 4-60$$

where  $\sigma_s^2 = \sigma_{s1}^2$  and  $r = \sigma_{s2}^2 / \sigma_{s1}^2$  is the power ratio of the input signals.

Since the input signals are not correlated and the signal covariance matrix is a diagonal matrix, the final test statistic function in Equation 4-8 simplifies to

$$\begin{aligned} T(\mathbf{x}) &= \mathbf{x}^H C_s (C_s + \sigma_w^2 \mathbf{I}_M)^{-1} \mathbf{x} \\ &= \frac{\sigma_s^2}{\sigma_s^2 + \sigma_w^2} x_0^2 + \frac{r \sigma_s^2}{r \sigma_s^2 + \sigma_w^2} x_1^2 \\ &= \frac{\Theta_{x0}}{\Theta_{x0} + 1} x_0^2 + \frac{\Theta_{x1}}{\Theta_{x1} + 1} x_1^2 \end{aligned} \quad 4-61$$

where  $\Theta_{x0} = \sigma_s^2 / \sigma_w^2$  and  $\Theta_{x1} = r \sigma_s^2 / \sigma_w^2$  are the average input SNR's of the diversity branches. As shown in

Figure 4.12 as well, the LRT detector weighs each input branch proportional to its average SNR. The lower input SNR leads to the lower weight and vice-versa.

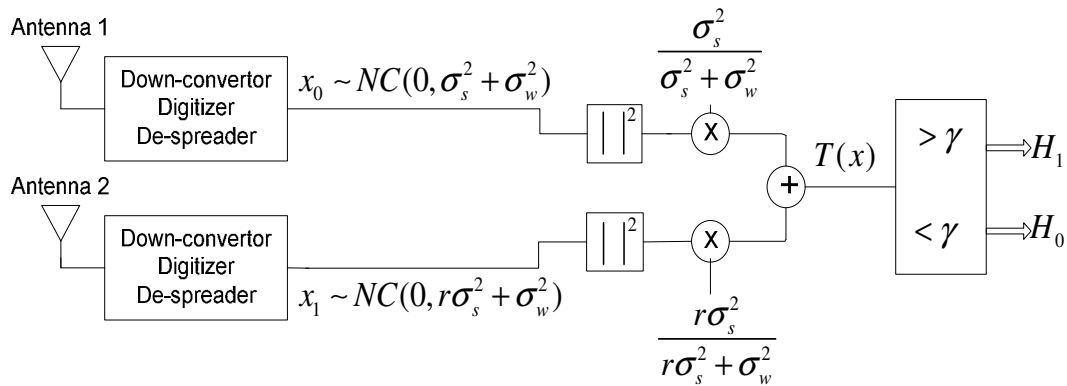


**Figure 4.12: Combining two unequal power input signals**

The eigenvalues of  $C_s$  are quantified as

$$\begin{aligned}\lambda_{s0} &= \sigma_s^2 \\ \lambda_{s1} &= r\sigma_s^2;\end{aligned}\tag{4-62}$$

therefore, according to Equation 4-28 to 4-30 the probabilities of detection and false alarm under such condition based on the mentioned eigenvalues results in

$$P_{D(EC,r)} = \frac{r\sigma_s^2 e^{-\frac{\gamma}{r\sigma_s^2}} - \sigma_s^2 e^{-\frac{\gamma}{\sigma_s^2}}}{(r-1)\sigma_s^2}\tag{4-63}$$

and

$$P_{FA(EC,r)} = \frac{\alpha_1 e^{-\frac{\gamma}{\alpha_1}} - \alpha_0 e^{-\frac{\gamma}{\alpha_0}}}{\alpha_1 - \alpha_0},\tag{4-64}$$

respectively, where

$$\alpha_0 = \frac{\sigma_s^2}{\sigma_s^2 + \sigma_w^2}, \alpha_1 = \frac{r\sigma_s^2}{r\sigma_s^2 + \sigma_w^2}.\tag{4-65}$$

The probability of detection of the LRT for the general condition as a function of input SNR ( $\Theta_{x0}$ ) and the signal power difference ( $r$ ) is shown in Figure 4.13. Here, the probability of false alarm is fixed to 0.01. Besides, the diversity gain is quantified as a function of probability of detection and input signals power difference and shown in Figure 4.14 for a specific design point of  $P_{FA}=0.01$ . This graph shows a zero diversity gain for a diversity structure with a power difference of 30 dB between input branches. This graph also shows that a 5-10 dB power difference between the diversity branches reduces the diversity gain significantly (almost 2 to 4 dB).

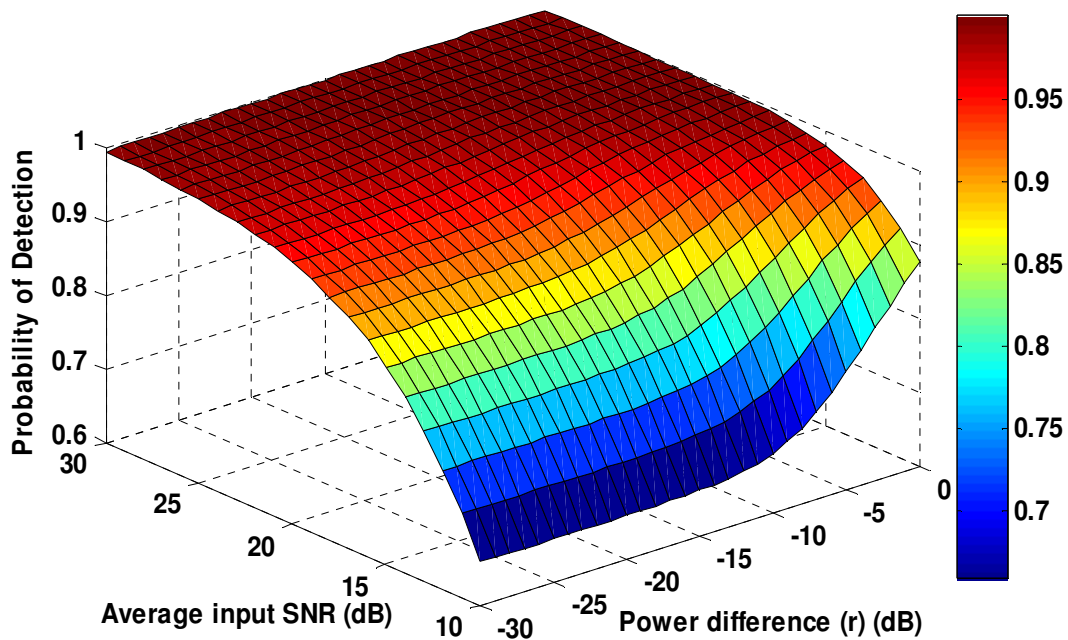


Figure 4.13: Probability of detection for unequal power and uncorrelated inputs

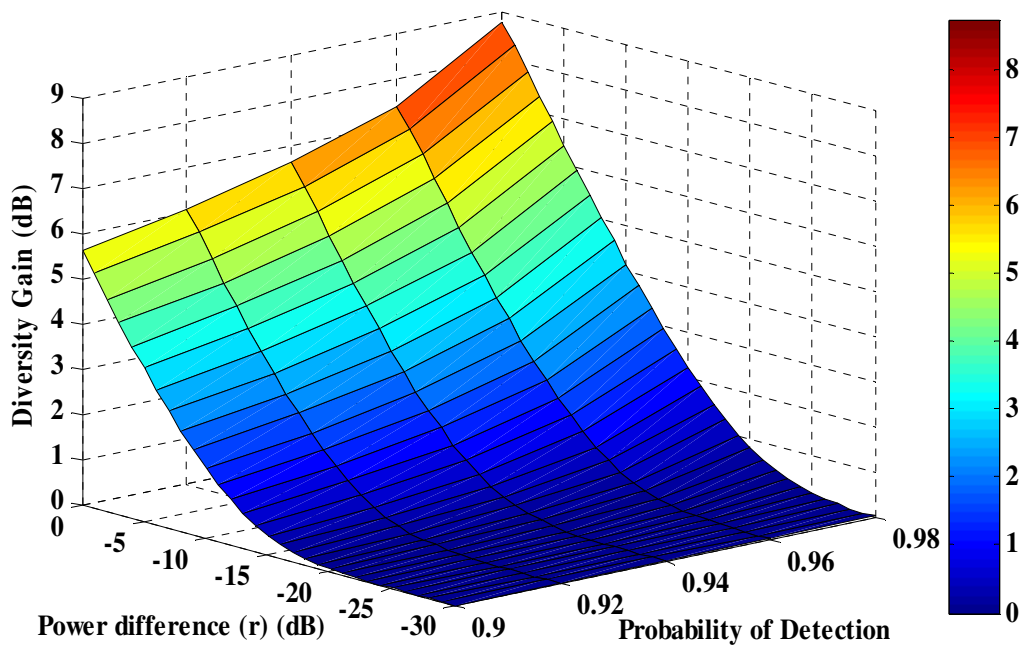


Figure 4.14: Diversity gain for unequal power and uncorrelated inputs

Combining these uncorrelated unequal power signals using the equal gain (EG) combiner, the probability of false alarm will be similar to the uncorrelated and equal power condition since under  $H_0$  the signal does not exist and there is only uncorrelated Gaussian noise. Therefore the probability of false alarm, as expressed in Equation 4-57, is quantified as

$$P_{FA(EG)} = \left(1 + \frac{\gamma}{\sigma_w^2}\right) e^{-\frac{\gamma}{\sigma_w^2}}. \quad 4-66$$

According to Equation 4-58, the probability of detection is evaluated as

$$P_{D(EG,r)} = \frac{\lambda_{x1} e^{-\frac{\gamma}{\lambda_{x1}}} - \lambda_{x0} e^{-\frac{\gamma}{\lambda_{x0}}}}{\lambda_{x1} - \lambda_{x0}} \quad 4-67$$

where  $\lambda_{x0}$  and  $\lambda_{x1}$  are the eigenvalues of the  $C_x = C_s + \sigma_w^2 I_2$  and equal to

$$\begin{aligned} \lambda_{x0} &= \sigma_s^2 + \sigma_w^2 \\ \lambda_{x1} &= r\sigma_s^2 + \sigma_w^2 \end{aligned} \quad 4-68$$

The diversity gain difference between the EC and EG combiners as a function of input signals power difference for different design points (fixed  $P_{FA}=0.01$  and various probability of detection) is shown in Figure 4.17. Up to a 10 dB power difference between input signals, the EC and EG carry almost the same performance and lead to almost equal diversity gain. By increasing the power difference between them, the diversity gain outweighs the EG combiner and leads to higher diversity gain.

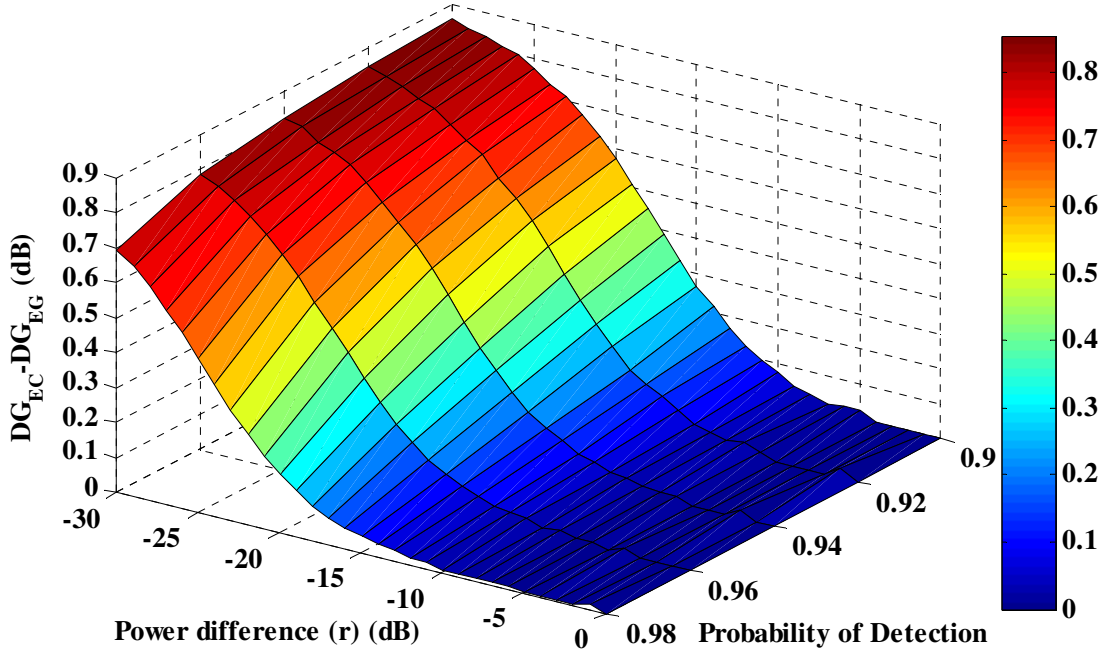


**Figure 4.15: EC and EG diversity gain difference for unequal power and uncorrelated inputs**

#### 4.4.5 Correlated unequal power inputs

Two correlated and unequal power inputs is the general condition for diversity system branches will be discussed herein. In this case, the covariance matrix of the received signals is defined as

$$C_s = \begin{bmatrix} \sigma_{s_1}^2 & E(x_1 x_2^*) \\ E(x_2 x_1^*) & \sigma_{s_2}^2 \end{bmatrix}. \quad 4-69$$

To simplify the general equation for the signal covariance matrix, without loss of generality, let us assume that

$$\sigma_{s_1}^2 = \sigma_s^2 \quad \text{and} \quad \sigma_{s_2}^2 = r \sigma_s^2, \quad 4-70$$

where  $r = \sigma_{s_2}^2 / \sigma_{s_1}^2$  is the power ratio of the input signals. In addition, the cross correlation coefficient ( $\rho$ ) between received signal is quantified as

$$\rho = \frac{E(x_1 x_2^*)}{\sqrt{\text{var}(x_1) \text{var}(x_2)}} = \frac{E(x_1 x_2^*)}{\sqrt{\sigma_s^2 \times r \sigma_s^2}} = \frac{E(x_1 x_2^*)}{\sigma_s^2 \sqrt{r}}. \quad 4-71$$

Therefore, the signal covariance matrix is rephrased as

$$C_s = \sigma_s^2 \begin{bmatrix} 1 & \rho\sqrt{r} \\ \rho\sqrt{r} & r \end{bmatrix}. \quad 4-72$$

As mentioned before, the final test statistic function results in

$$T(x) = \sum_{m=0}^1 \frac{\lambda_{sm}}{\lambda_{sm} + \sigma_w^2} y_m^2, \quad 4-73$$

where  $\lambda_{s0}$  and  $\lambda_{s1}$  are the eigenvalues of  $C_s$  quantified here as

$$\begin{aligned} \lambda_{s0} &= \frac{\sigma_s^2}{2} \left[ (r+1) + \sqrt{(1-r)^2 + 4r\rho^2} \right] \\ \lambda_{s1} &= \frac{\sigma_s^2}{2} \left[ (r+1) - \sqrt{(1-r)^2 + 4r\rho^2} \right] \end{aligned} \quad 4-74$$

The probability of detection and false alarm for this general condition are expressed in Section 4.3 as

$$P_D = \frac{\lambda_{s1} e^{-\frac{\gamma}{\lambda_{s1}}} - \lambda_{s0} e^{-\frac{\gamma}{\lambda_{s0}}}}{\lambda_{s1} - \lambda_{s0}} \quad 4-75$$

and

$$P_{FA} = \frac{\alpha_1 e^{-\frac{\gamma}{\alpha_1}} - \alpha_0 e^{-\frac{\gamma}{\alpha_0}}}{\alpha_1 - \alpha_0}, \quad 4-76$$

respectively, where

$$\alpha_n = \frac{\lambda_{sn}}{\lambda_{sn} + \sigma_w^2}. \quad 4-77$$

The probability of detection for a fixed probability of false alarm ( $P_{FA}=0.01$ ) as a function of signal cross correlation coefficient and input power difference is shown in Figure 4.16. Lower performance results from a higher power difference and cross correlation coefficient between input branches. Besides, the diversity gain for this general condition is quantified and shown in Figure 4.17 for a specific design point of  $P_{FA} = 0.01$  and  $P_D = 0.9$ . This shows at least 3 dB diversity gain for highly correlated yet equal power inputs, as it was expected. However, by increasing the power difference between input signals, the diversity gain reduces to 0 dB even for uncorrected input signals, which is due to signal degradation in one of the branches.

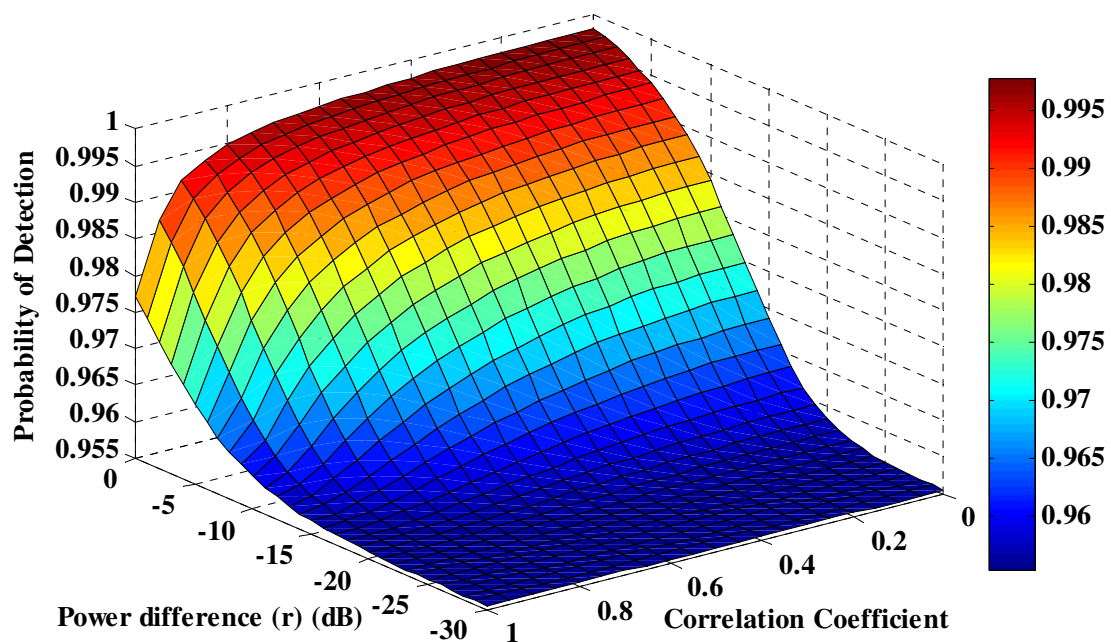


**Figure 4.16: The probability of detection for a fixed probability of false alarm ( $P_{FA} = 0.01$ ) for the general condition**

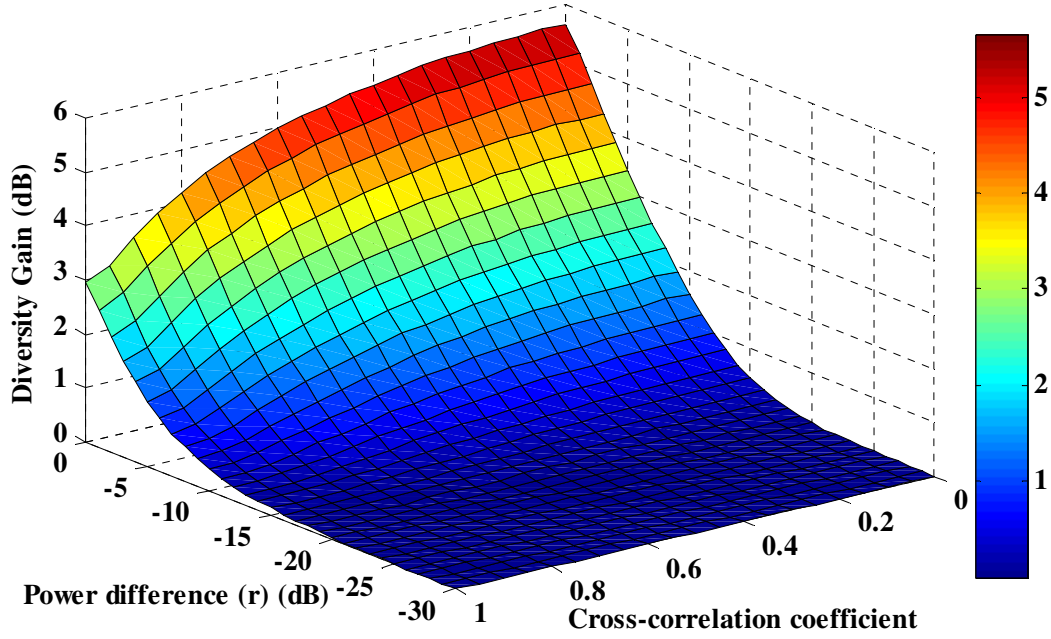


**Figure 4.17: The diversity gain for the general condition as a function of signals cross correlation coefficient and input power difference**

Combining these correlated unequal power signals by the equal gain (EG) combiner results in the same probability of false alarm as that noted in Equation 4-57 and the probability of detection (according to Equation 4-58) is then given by

$$P_{D(EG,r)} = \frac{\lambda_{x1} e^{-\frac{\gamma}{\lambda_{x1}}} - \lambda_{x0} e^{-\frac{\gamma}{\lambda_{x0}}}}{\lambda_{x1} - \lambda_{x0}} \quad 4-78$$

where  $\lambda_{x0}$  and  $\lambda_{x1}$  are the eigenvalues of the  $C_x = C_s + \sigma_w^2 I_2$  and are equal to

$$\begin{aligned} \lambda_{x0} &= \frac{1}{2} \left[ \sigma_s^2 (r+1) + 2\sigma_w^2 + \sigma_s^2 \sqrt{(1-r)^2 + 4r\rho^2} \right] \\ \lambda_{x1} &= \frac{1}{2} \left[ \sigma_s^2 (r+1) + 2\sigma_w^2 - \sigma_s^2 \sqrt{(1-r)^2 + 4r\rho^2} \right] \end{aligned} \quad 4-79$$

In Figure 4.18, the diversity gain difference between the estimator correlator and equal gain combiner is shown as a function of power difference and cross-correlation

coefficient between received signals. Here, the design point is determined as  $P_{FA} = 0.01$  and  $P_D = 0.9$ . According to this graph and based on Figure 4.17, and contrary to estimator correlator, the equal gain combiner results in negative diversity gain by combining two signals with a significant power difference.

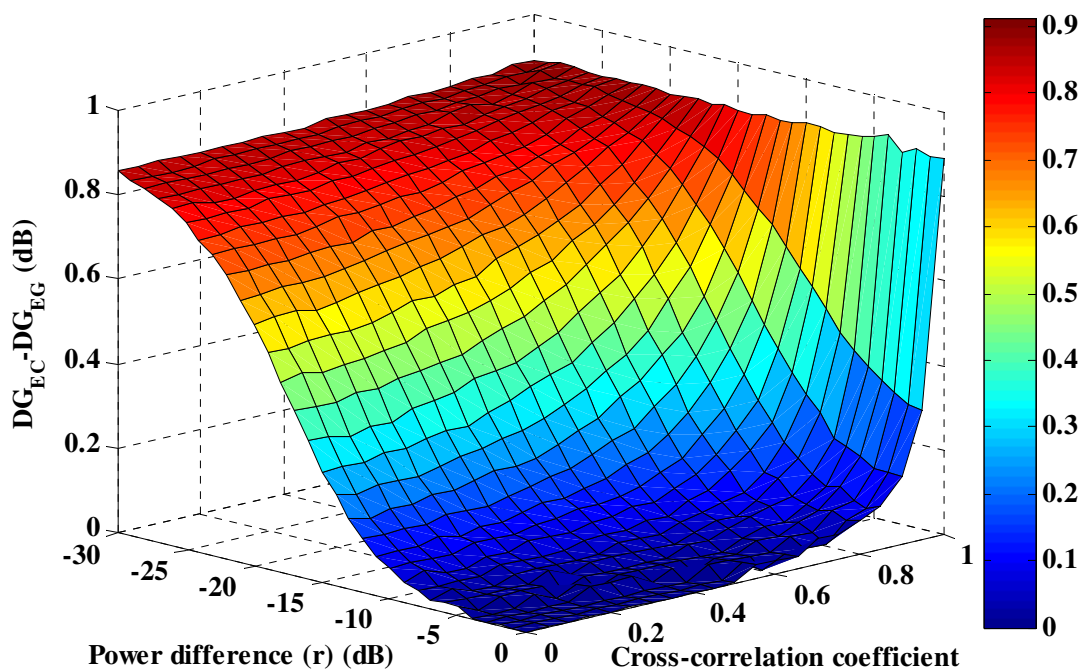


**Figure 4.18: EC and EG diversity gain difference for the general condition as a function of signal cross correlation coefficient and input power difference**

#### 4.5 Summary

In this chapter, the ROC curve and diversity gain as two important metrics to evaluate a detector were introduced and different combining methods were described. Using known evaluation metrics, the performance of the EC and the EG combiners were examined under various situations in terms of input signal covariance matrix. It has been concluded that the EG and EC combiners carry the same performance for low correlation coefficients (less than 0.6) and low input level difference up to 10 dB for the selected

design point of  $P_{FA}=0.01$  and  $P_D=0.9$ . Therefore, since the estimator correlator is more complex to implement rather than the equal gain combiner, the latter has been selected as the sub-optimum combiner for practical tests. In the next chapter, the test setup and the collected data sets will be explained and empirical results of the target diversity gain structures will be presented.

## **Chapter Five: Test Setup and Experimental Results**

In the previous chapters, the theoretical diversity gain of a dual polarized diversity system relative to a single polarized antenna was described based on the idealized Rayleigh fading model which led to usable expressions for the relative diversity gain. The experimental measurements described in this chapter attempt to partially validate the application of these assumptions in the context of the dual polarized diversity system for indoor GNSS applications.

In order to examine the performance of the proposed method for combining two received GPS signals by a dual polarized GPS antenna, various experiments were performed. First of all, the performance of combining received RHCP and LHCP signals in indoor environments is examined and the improvement on detectability of GPS L1C/A signal is quantified.

In addition, other experiments are designed to compare the performance of polarization diversity with spatial diversity in indoor environments. The polarization diversity structure examined in this section includes both circular and linear antenna sets. Since indoor environments are usually modeled as rings of scatters and a signal arrives at the antenna from different directions, in addition to RHCP/LHCP antennas, a dual polarized linear antenna consisted of vertical and horizontal antennas is utilized to compare its performance with its circular polarization structure. The test descriptions and details along with the empirical results are explained in this chapter.

### **5.1 Circular polarization diversity**

#### ***5.1.1 Test Setup***

The data collection set up consisted of a commercial dual-polarized antenna connected to a synchronized triple port down-converter/digitizer. Thus, synchronous raw

IF samples were collected in the L1 band for both LHCP and RHCP antennas. Two bias-tees were used to provide the required power for the pre-amplifiers inside the antenna for each individual channel. The collected signals were passed through an external filter and an amplifier prior to the down conversion procedure. The antenna and associated signal conditioning components are illustrated in Figure 5.1. Data were also simultaneously collected from an additional reference RHCP antenna, located at a site with an unobstructed view of the sky. The reference antenna was kept within 30 m of the dual polarized indoor antenna.

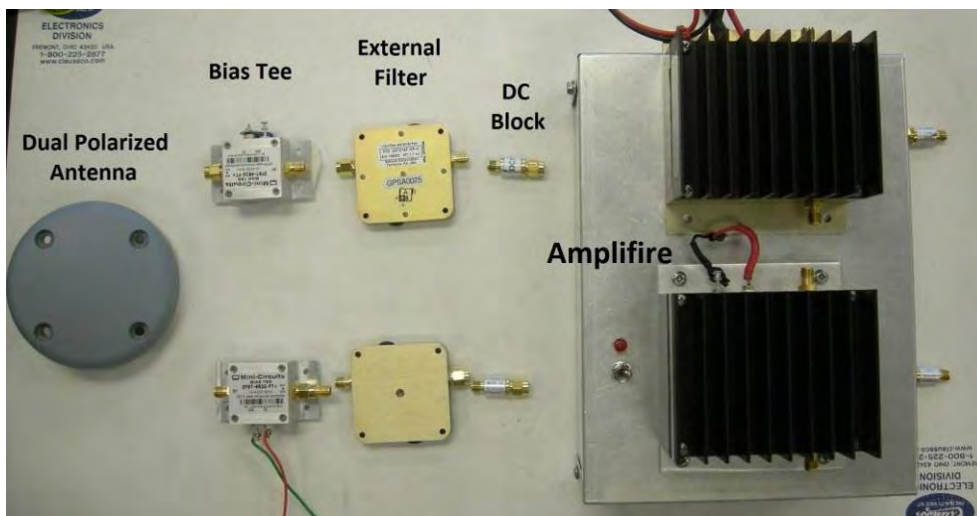


**Figure 5.1: Antenna and associated hardware used in the data collections**

Five data sets in four different indoor environments were collected to investigate the performance of the circular polarization diversity method using real GPS signals. To conveniently obtain independent samples from a variety of locations, a linear motion table was used. In each measurement set, the dual polarized antenna was mounted on the linear motion table (Figure 5.2) which was placed in a random orientation in the middle of the data collection site. The antenna moved 2.8 m (2 x 1.4 m) during each lap. As will be discussed in the next section, the coherent integration time defining the sampling rate

should be considered for determining the speed of the moving antenna. In these experiments, the coherent integration time was set to 100 ms resulting in reasonable SNR in the data collection environments. The speed of the table will be determined in the next section to be commensurate to the coherent integration time.

The first data set was collected on 19 January 2009 starting at 6:54pm in a laboratory room of the CCIT building in the University of Calgary with concrete external walls and roof and metallic covering on the building walls (Figure 5.2). This data set was gathered over 20 minutes with a sampling rate of 10 Mega-samples Per Second (MSPS) and an intermediate frequency (IF) of 3.42 MHz. There were some window panes in the east and south sides of the data collection site. According to the sky plot shown in Figure 5.3, several space vehicles (SV) on the eastern side of the building were examined and after a pre-analysis PRN14 and PRN22 were selected for further analysis for this work since they carry higher SNR among the space vehicles.

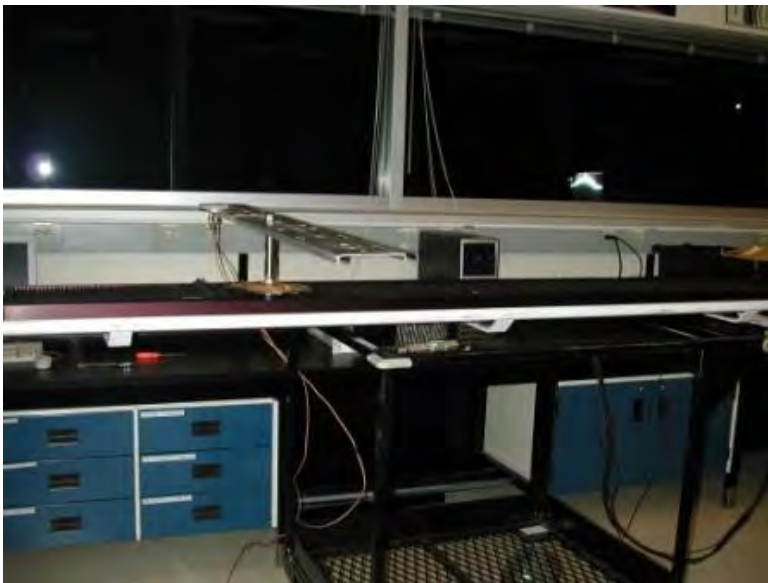


**Figure 5.2: Dual polarized antenna mounted on the linear motion table in NavLab, CCIT building**

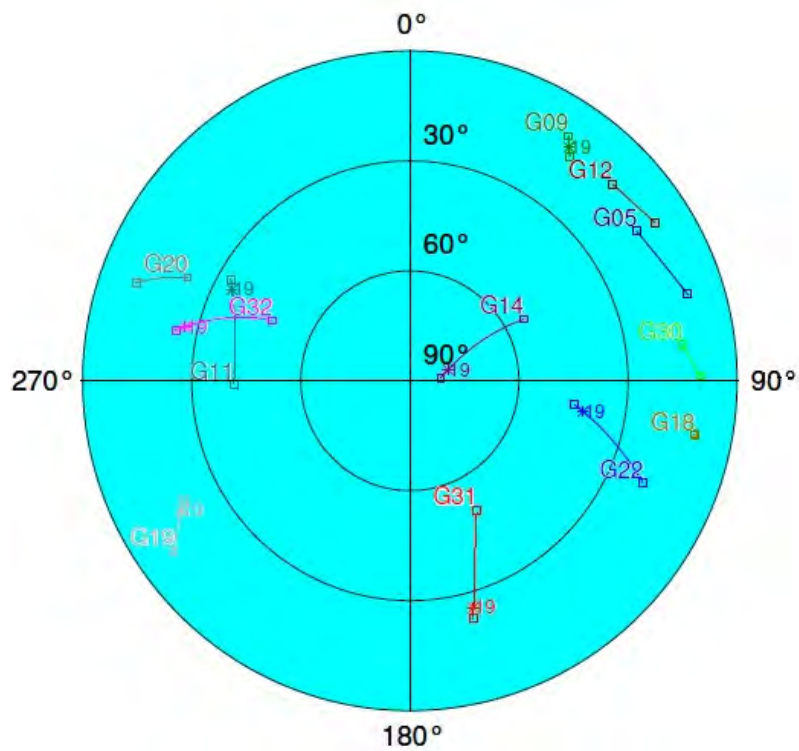


**Figure 5.3: Corresponding sky plot for the data set collected on 19 January 2009**

The second and third data sets were collected in a meeting room in the same building, which has window panes in the south and west sides, on March 6<sup>th</sup> 2009 (Figure 5.4). The windows are covered with a conductive film which results in about 20-30 dB penetration loss of the received GPS signals. The data collection for the second and third data sets was started at 4:00 p.m. for 30 minutes and 7:00 p.m. for 25 minutes, respectively. Since the window panes are located in the south and west side of this room, the satellite vehicles located near to 180 and 270 degree azimuth are selected according to the sky plot shown in Figure 5.5.

The fourth and fifth data sets were collected on May 20<sup>th</sup> 2009. The former was performed in a laboratory with a high metallic ceiling (Figure 5.6), at 3 p.m. and the latter was gathered in the campus student centre, a large hall with a partly glass roof (Figure 5.7), at 6 p.m. The selected IF frequency and sampling rate for these data sets were 0.42

MHz and 10 MSPS respectively. According to their corresponding sky plots (Figure 5.8 and Figure 5.9), appropriate GPS satellite vehicles are selected from each data set as tabulated in Table 5.1.



**Figure 5.4: Room 326 in CCIT building**

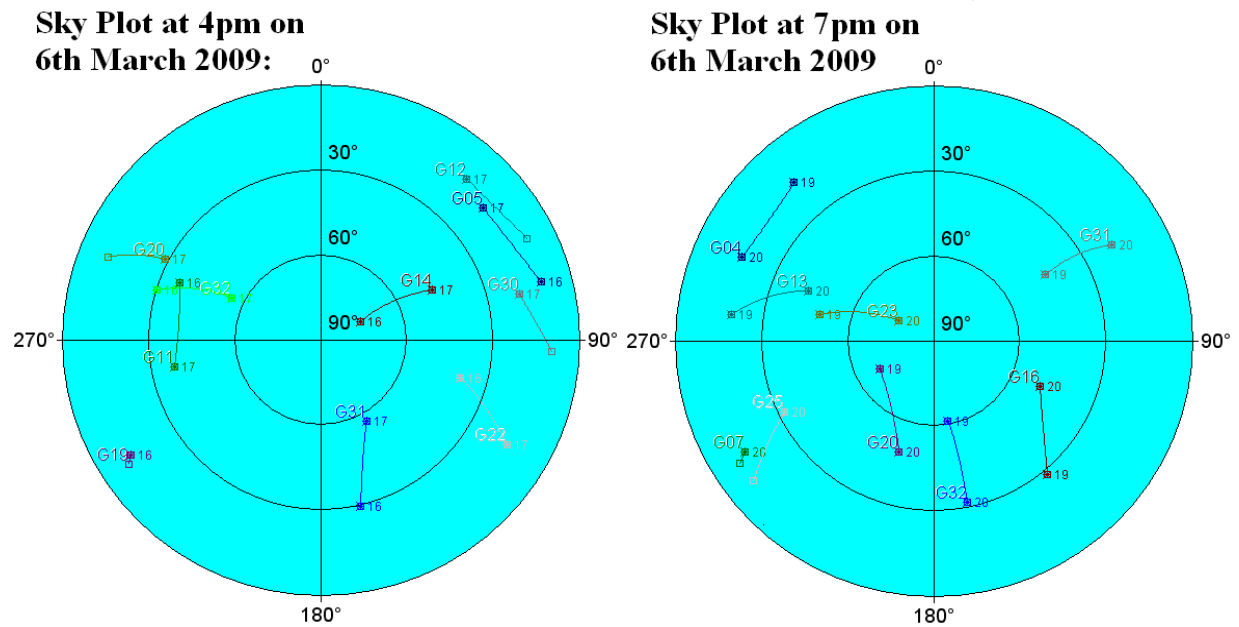


**Figure 5.5: Sky plots for collected data on 6 March 2009**



**Figure 5.6: Energy High Bay in CCIT building, University of Calgary**



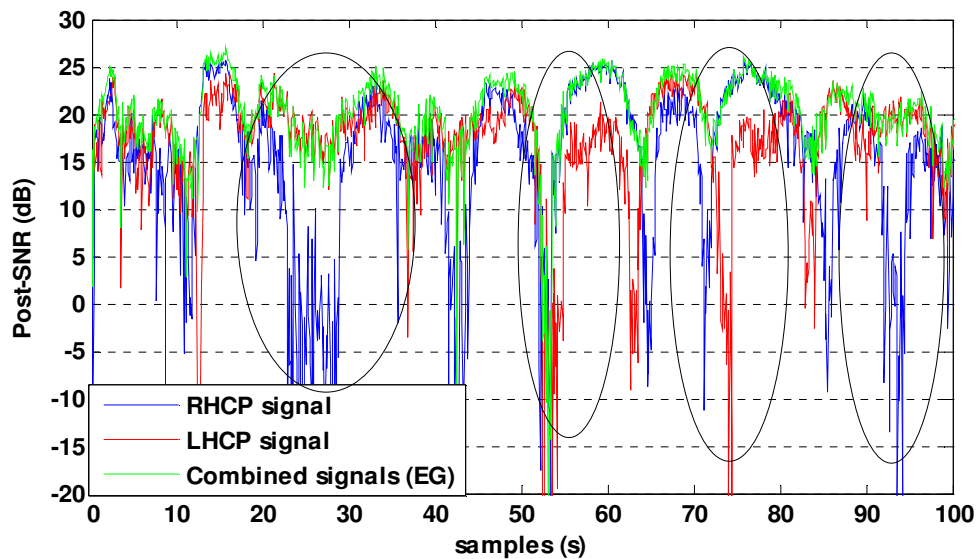
**Figure 5.7: MacEwan Hall in University of Calgary**



**Table 5.1: Data sets and selected vehicle satellites for each set**

Set#	Date and time of collection	Location	Selected SV's
1	19 Jan 2009 at 18:54	Navlab	14, 22
2	6 Mar 2009 at 16:00	CCIT 326	11, 22, 31, 32
3	6 Mar 2009 at 19:00	CCIT 326	16, 20, 23, 32
4	20 May 2009 at 15:00	Energy High Bay	13, 23
5	20 May 2009 at 18:00	MacEwan Hall	7, 25, 8

It should be noted that, in order to evaluate the effectiveness of a diversity system, a minimum average SNR power in the received signals is required. In Chapter 4, it was shown theoretically that for very low input SNR the detector performance for both single antenna and estimator correlator goes to zero (see Figure 4.9). As shown in Figure 5.10, a diversity system removes the signal level fluctuations by combining different branches. When the signal in one of the branches fades, the other branch with higher SNR keeps the diversity output SNR in a reasonable level. In this work, the satellite vehicles selection procedure was based on the mean level SNR.

**Figure 5.10: Post-SNR output in a diversity system**

## 5.1.2 Coherent integration time selection

### 5.1.2.1 Channel coherence time

As defined in Chapter 2, the channel coherence time,  $T_c$ , is the maximum time duration over which two received signals are highly correlated. Using a well-known rule of thumb, the channel coherence time is defined as (Rappaport 2002)

$$T_c = \frac{0.423}{f_m}, \quad 5-1$$

where  $f_m$  is maximum Doppler shift given by  $f_m = v / \lambda$ . In other words, the channel coherence time implies that two signals arriving through a channel with a time delay greater than  $T_c$  seconds are affected differently by the channel. Therefore, the maximum coherent integration time for received GPS signals is limited by the channel coherence time. For the GPS L1C/A code ( $\lambda \approx 19.029$  cm) and an average relative velocity of the GPS antenna and the scatters equals to 2.5 cm/s, the maximum recommended coherent integration time is 3.2 seconds.

### 5.1.2.2 Channel phase rate

Fading is a spatial phenomenon, which causes the received signal in sufficiently separated spatial positions to be independent. Hence, to capture statistically independent signal samples, a dual polarized antenna was mounted on a linear moving table. In a fading channel, when the receiver antenna moves, the apparent frequency of the signal varies with time in a random manner and the signal exhibits random frequency modulation (Jakes 1974). The expression for the probability density function of the channel phase rate, called instantaneous frequency,  $\dot{\theta}$ , as given by Jakes (1974) is

$$p(\dot{\theta}) = \frac{1}{\omega_m \sqrt{2}} \left[ 1 + 2 \left( \frac{\dot{\theta}}{\omega_m} \right)^2 \right]^{-3/2}, \quad 5-2$$

where  $\omega_m = \omega_c v / c$  is the maximum Doppler shift in radians per second,  $v$  is the mobile antenna speed in m/s,  $c$  is the speed of light, and  $\omega_c$  is the carrier angular frequency in radians per second. Figure 5.11 shows the PDF for  $f_c = 1575.42$  MHz, the L1 C/A code frequency, and an antenna speed of 2.5 cm/s. The confidence level ( $\kappa$ ) for a specific sampling rate ( $f_s$ ) guaranteeing that the signal remains within the Nyquist interval is quantified based on this Doppler frequency PDF as (Narayanan et al 2004)

$$\kappa = \int_{\dot{\theta} = -f_s/2}^{\dot{\theta} = +f_s/2} p(\dot{\theta}) d\dot{\theta}. \quad 5-3$$

It is computed through this equation that for the given conditions that a sampling rate of 10 samples per second is sufficient to guarantee that 99.6% of the signal remains unaliased or within the Nyquist interval. Having considered this condition on sampling rate, minimal errors occur due to under-sampling. This sampling rate (10 Hz) results in a maximum 100 ms pre-integration time (PIT) in the acquisition procedure. To increase the PIT limitation, the antenna speed must be reduced. In this work, according to this PIT limitation and channel coherence time, the speed of antenna in the performed tests was maintained at a value less than 2.5 cm/s and the signals are coherently integrated over 100 ms.

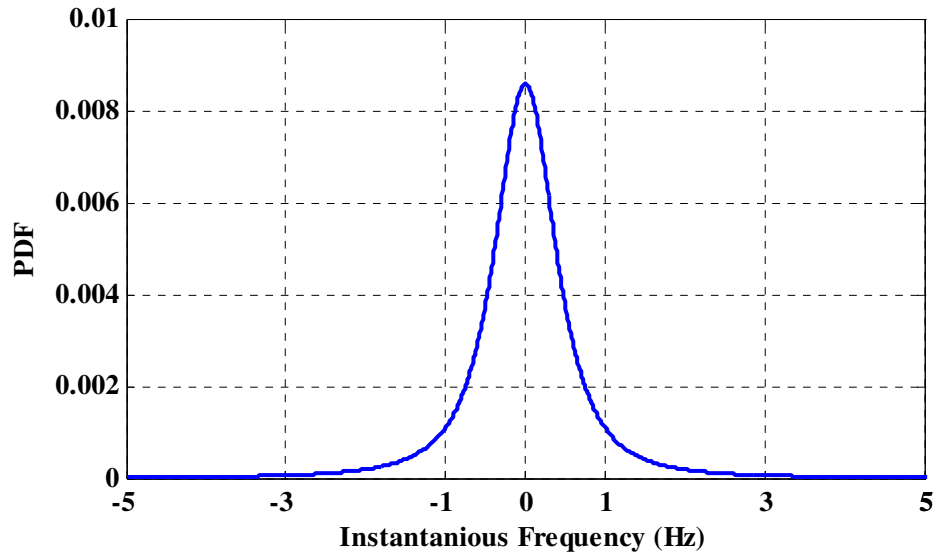


**Figure 5.11: The instantaneous frequency PDF for GPS L1 frequency and an antenna speed of 2.5 cm/s**

### *5.1.3 Developed software*

The reference antenna signal was analyzed with the University of Calgary GNSS Software Navigation Receiver called GSNRx<sup>TM</sup> (O’Driscoll et al 2009). The resulting outputs were then used to wipe off the navigation data in the collected indoor signals through another program developed in MATLAB.

The average Doppler frequency for each 100 ms coherent integration time was also derived from the reference antenna. A common rule of thumb for selection of the Doppler frequency bin size in acquisition is  $2/3T$ , where  $T$  is the pre-detection integration time (Kaplan & Hegarty 2006). Here,  $T$  is equal to 100 ms, hence the Doppler bins of the Doppler search space should be about 6.66 Hz. The antenna speed is 2.5 cm/s, which leads to a maximum Doppler frequency of 0.13 Hz, this being the maximum difference between the Doppler at the reference antenna and that at the dual polarized one. Therefore, the Doppler frequency estimated from the reference antenna is sufficient

enough and no more Doppler search is required. Having calculated the Doppler frequency from the reference antenna, a one dimensional search space remains for the acquisition procedure. This search space is covered using an FFT based correlation technique to correlate the received signal with the locally generated PRN code.

In the next stage, the signals are combined through an appropriate combining scheme, chosen according to the signal characteristic and correlation coefficient. The empirical distribution functions are obtained directly from the correlator outputs. A single sample point is chosen as the “true” delay based on the information from the reference antenna. This represents the  $H_1$  condition. The  $H_0$  condition is assumed to hold for all correlator outputs which are more than 1 full chip (approximately 10 samples) away from the  $H_1$  correlator (correlator outputs within 1 full chip of the  $H_1$  bin are discarded). Thus, for each FFT output there is one  $H_1$  bin and thousands of  $H_0$  bins, as shown in Figure 5.12. The correlation between  $H_0$  bins is avoided by down-sampling (only every 10<sup>th</sup>  $H_0$  bin is retained). The empirical density functions are obtained by the histogram method over thousands of successive 100 ms correlator outputs.

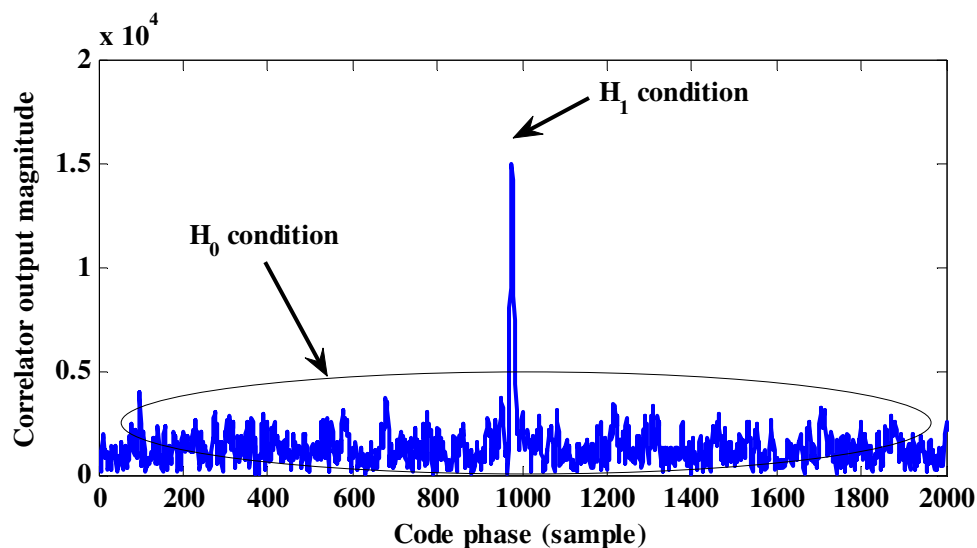


**Figure 5.12: Correlator output under  $H_1$  and  $H_0$  conditions**

### 5.1.4 Results

#### 5.1.4.1 Channel Measurement:

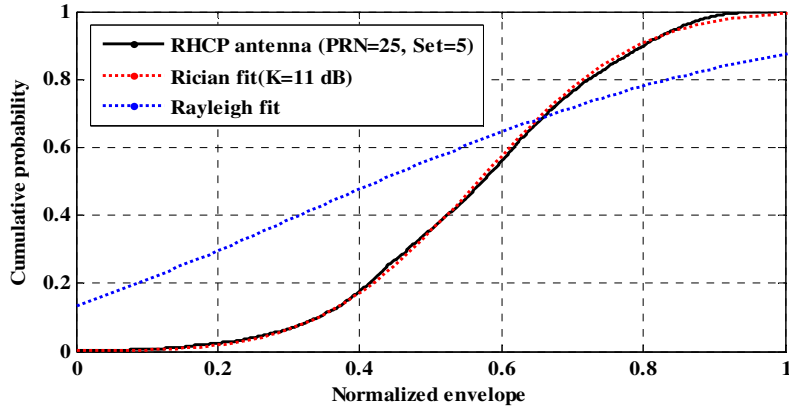
As discussed before, the Rician and Rayleigh distributions can be distinguished by defining the  $K$  factor which shows the dominant to multipath power ratio in the received signal. It is quantified as (Colburn et al 1998)

$$K = \frac{\text{LOS component power}}{\text{Multipath component power}} = \frac{\mu^2 / 2}{\sigma^2}, \quad 5-4$$

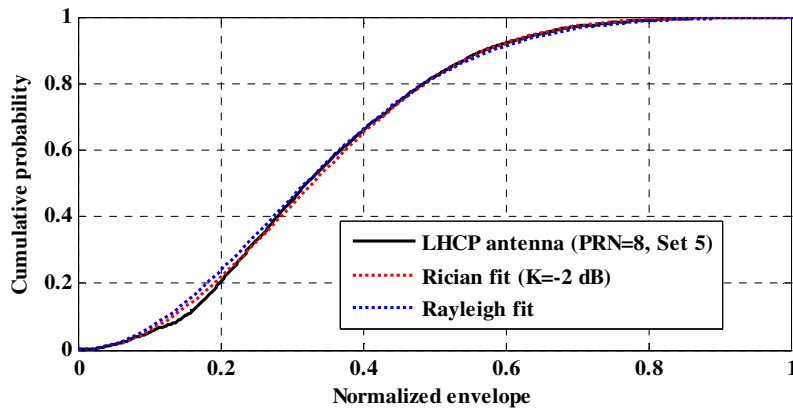
where  $\mu^2$  and  $\sigma^2$  are the mean and variance of the Rician distributed signal.

As discussed in Chapter 2, for small  $K$  factors, the Rician distribution agrees with that of the Rayleigh distribution. In order to examine the fitness of various distributions practically, the “distribution fit function” in MATLAB has been used. This toolbox uses the maximum likelihood estimator to estimate the parameters of the signal such as its variance and mean. In Figure 5.13 the fitted Rician and Rayleigh distributions on the RHCP and LHCP signals with different  $K$  factors are plotted. It is obvious that for  $K = -2$  dB (Figure 5.13(b)) and even  $K = 0.08$  (Figure 5.13(c)), the Rayleigh and Rician characteristics are almost equal.

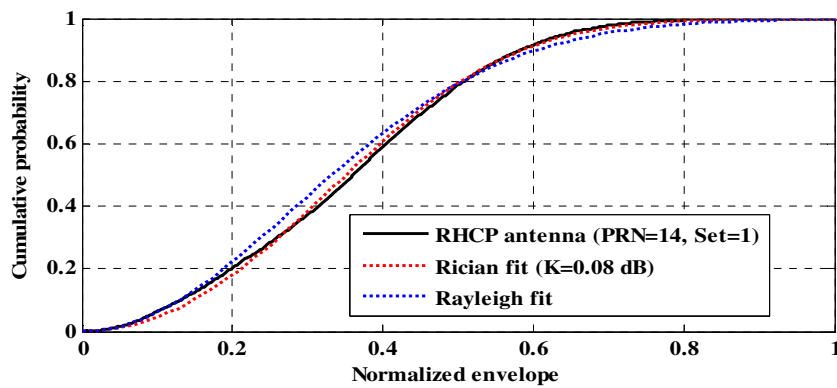
In Table 5.2 the  $K$  factors for all selected satellites are tabulated. It is evident from the table that in most cases the indoor channel for both RHCP and LHCP GNSS signals is very close to Rayleigh fading channel (small  $K$  factors). Therefore, the estimator correlator combining method can be at least empirically considered as an optimum method for combining received signals. For higher values of the  $K$  factor, such as PRN 25 in dataset 5, the Rayleigh model is not accurate any more (see Figure 5.13(a)) and the estimator correlator architecture is no longer optimal.



(a) PRN 25 from dataset 5



(b) PRN 8 from dataset 5



(c) PRN 14 from dataset 1

**Figure 5.13: Cumulative probability of received signals and fitted Rician Rayleigh distribution**

**Table 5.2:  $K$  factor measurements for received signals in different indoor environments**

PRN# (set#)	$K$ factor (dB)	
	RHCP	LHCP
14(1)	0.08	- 45
22(1)	- 59	- 57
11(2)	-71	-3.8
22(2)	-62	-71
31(2)	-63	-73
32(2)	-58	-67
16(3)	-63	-63
20(3)	-13	-61
23(3)	-65	-70
32(3)	-66	-61
13(4)	-3.1	-2.6
23(4)	-3	-4.9
7(5)	-1.3	-60
25(5)	11	-0.07
8(5)	-2.2	-2

#### 5.1.4.2 Correlation Coefficient

As discussed previously, in order to achieve diversity gain from combining a diverse array of branches, the correlation between received signals should be sufficiently low (Narayanan et al 2004). The correlation coefficient between two received signals can be characterized using either the envelope or complex forms of the input signals as (Colburn et al 1998)

$$\rho_e = \frac{E[\sqrt{S_1}\sqrt{S_2}]}{\sqrt{E[\sqrt{S_1}\sqrt{S_1}]E[\sqrt{S_2}\sqrt{S_2}]}} \quad 5-5$$

and

$$\rho_c = \frac{E[x_1x_2^*]}{\sqrt{E[x_1x_1^*]E[x_2x_2^*]}} \quad 5-6$$

respectively. Here,  $E[\bullet]$  is the expected value operator,  $V_1$  and  $V_2$  are zero mean complex values of the correlator output of each branch, and  $S_1$  and  $S_2$  are their zero-meaned received power, i.e. (Colburn et al 1998)

$$S_i = x_i x_i^* - E[x_i x_i^*] \quad 5-7$$

Assuming that the received signals have a Rayleigh distributed envelope and randomly distributed phase, the envelope and complex correlation coefficient are associated with each other as (Gao 2007)

$$|\rho_c|^2 = \rho_e \quad 5-8$$

However, Narayanan et al (2004) quantify both complex and envelope correlation coefficients based on the experimental results and concluded that the value of the complex correlation coefficient is constant from run to run and, hence, a more reliable metric. Since in the likelihood ratio test the complex correlation is used to define the input signals correlation matrix, herein the complex correlation coefficient between RHCP and LHCP signals in indoor situations will be evaluated by processing the measured GPS signals. In Table 5.3, the absolute value of the complex correlation coefficient ( $|\rho_c|$ ) between the received signals is tabulated. According to these coefficients, the correlation between received signals in two RHCP and LHCP branches

is less than 0.5 in indoor environments. In this table, all values are less than 0.36 except for a value of 0.47, while the average of the calculated correlations is only 0.21. In this table, the total samples column shows the number of samples that are used to calculate correlation coefficient as a statistical variable.

**Table 5.3: Measured correlation coefficient between received signals**

<b>PRN# (set#)</b>	<b>Total Samples</b>	<b>Correlation coefficient</b>
14(1)	12220	0.20
22(1)	12190	0.17
11(2)	17990	0.22
22(2)	17980	0.10
31(2)	17980	0.24
32(2)	17990	0.20
16(3)	14990	0.14
20(3)	14990	0.17
23(3)	14990	0.36
32(3)	14990	0.17
13(4)	6050	0.26
23(4)	6060	0.24
7(5)	5450	0.14
25(5)	5450	0.47
8(5)	5450	0.14
<b>Average</b>		<b>0.21</b>

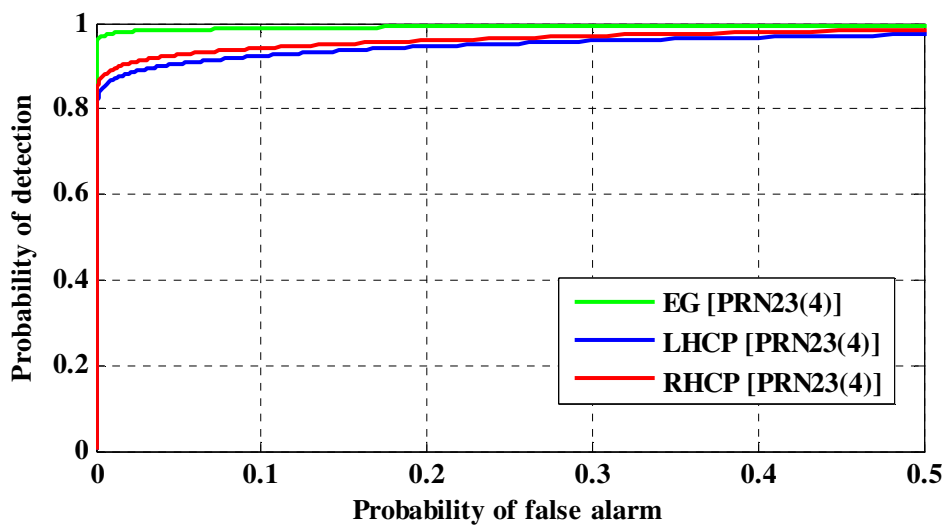
These results show a sufficiently low correlation between RHCP and LHCP signals in indoor situations. As discussed, the estimator correlator and equal gain combining have the same performance for low correlated signals; therefore, since the EG combiner has less computational cost, the RHCP and LHCP signals will be combined

using the equal gain combiner. Additionally, a full diversity performance can be expected from the polarization diversity scheme since in most of the times it carries sufficiently low correlation coefficient (less than 0.3)(see Figure 4.6).

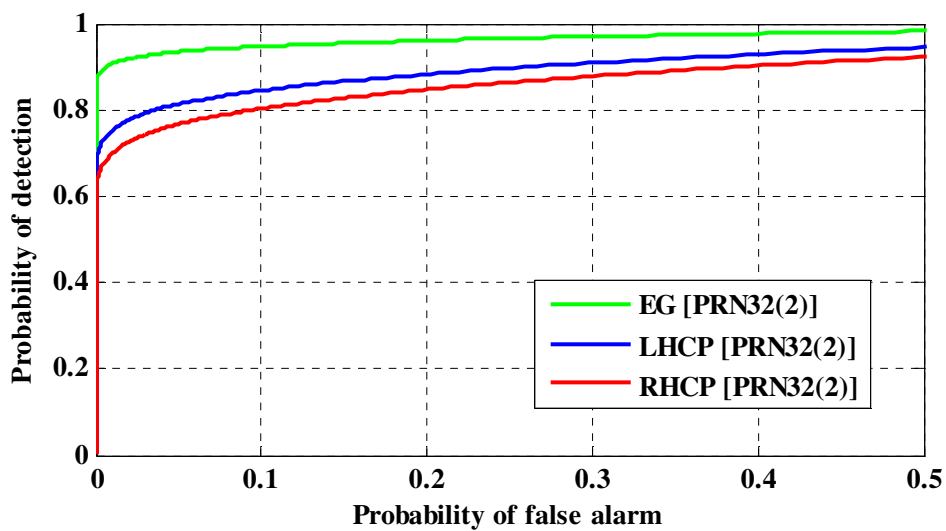
#### 5.1.4.3 Empirical ROC curve

Having calculated the probability distribution function (PDF) of each individual branch and the combined signal under  $H_0$  and  $H_1$ , the ROC curves can be plotted using a threshold as an intermediate variable (Kay 1998). Figure 5.14 shows the empirical ROC curves based on the received signals in indoor environments for two selected satellites (PRN 32 from data set 2 and PRN 23 from data set 4). As it can be seen in Figure 5.14(b) the probability of detection of LHCP signals is higher than that of the RHCP signals. By combining them using the EG combiner, the receiver utilizes the advantages of LHCP signals to improve the detectability of the GNSS signals. In addition, the probability of detection of all selected satellites for a specific probability of false alarm ( $P_{FA}=0.01$ ) is shown in Figure 5.15. The interesting point is that LHCP signals have a better detectability in some cases such as PRN 11 in set 2 and PRN 13 in set 4.

The improvement in the probability of detection of combined signals shown in Table 5.4 is compared to the single signal received by the RHCP antenna. According to this table, the probability of detection after combining RHCP and LHCP signals is enhanced compared to that of the RHCP signal in all cases, which shows the improvement in the detectability of GNSS signals by the proposed scheme.



(a) PRN 23 from data set 4



(b) PRN 32 from data set 2

Figure 5.14: Empirical ROC curves for two selected satellites: (a) PRN 23 from data set 4 (b) PRN 32 from data set 2

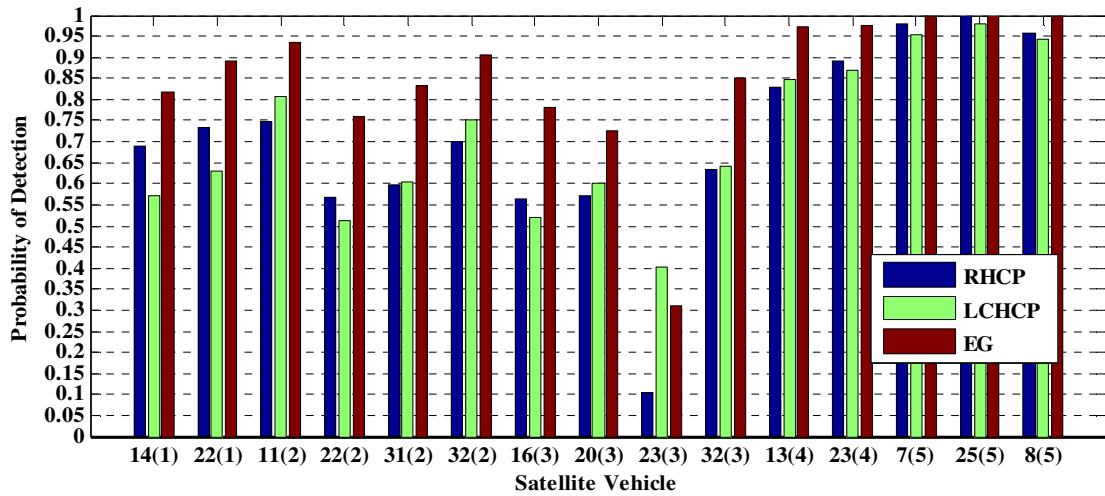


Figure 5.15: Probability of detection for a specific design point ( $P_{FA}=0.01$ )

Table 5.4: Probability of detection for a specific probability of false alarm (0.01)

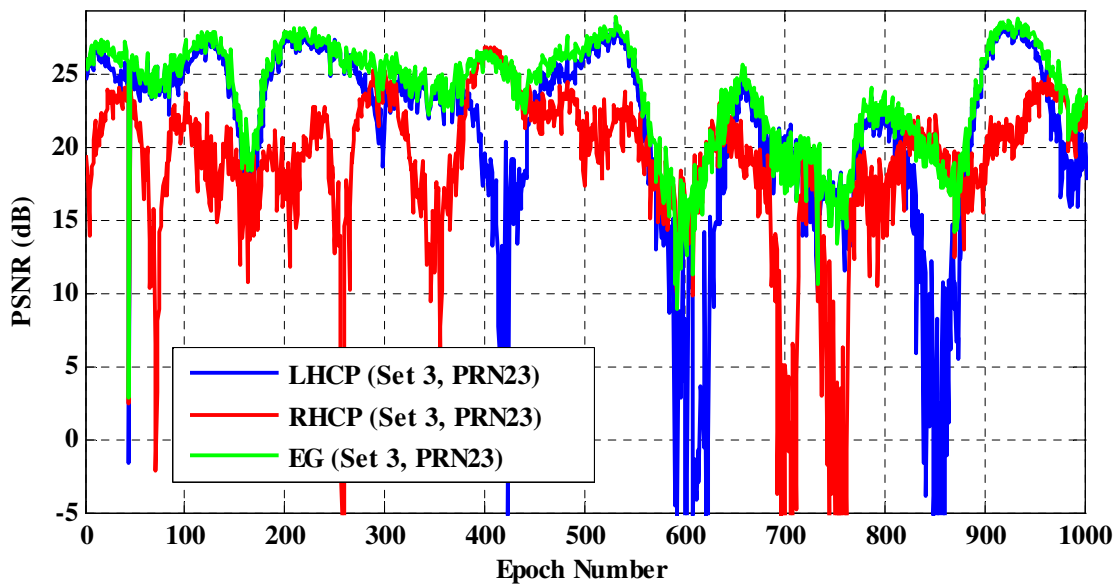
PRN# (set#)	$P_D$ (LHCP)	$P_D$ (RHCP)	$P_D$ (EG)	Improvement (Ave = 0.15)
14(1)	0.56	0.68	0.77	<b>0.09</b>
22(1)	0.62	0.73	0.83	<b>0.1</b>
11(2)	0.81	0.75	0.91	<b>0.16</b>
22(2)	0.51	0.56	0.7	<b>0.14</b>
31(2)	0.6	0.6	0.76	<b>0.16</b>
32(2)	0.75	0.7	0.87	<b>0.17</b>
16(3)	0.54	0.58	0.73	<b>0.15</b>
20(3)	0.61	0.6	0.76	<b>0.16</b>
23(3)	0.53	0.07	0.37	<b>0.3</b>
32(3)	0.63	0.63	0.81	<b>0.18</b>
13(4)	0.84	0.82	0.97	<b>0.14</b>
23(4)	0.86	0.89	0.97	<b>0.08</b>
7(5)	0.95	0.97	0.99	<b>0.02</b>
25(5)	0.98	1	1	<b>0</b>
8(5)	0.94	0.95	0.99	<b>0.04</b>

#### 5.1.4.4 Fading mitigation

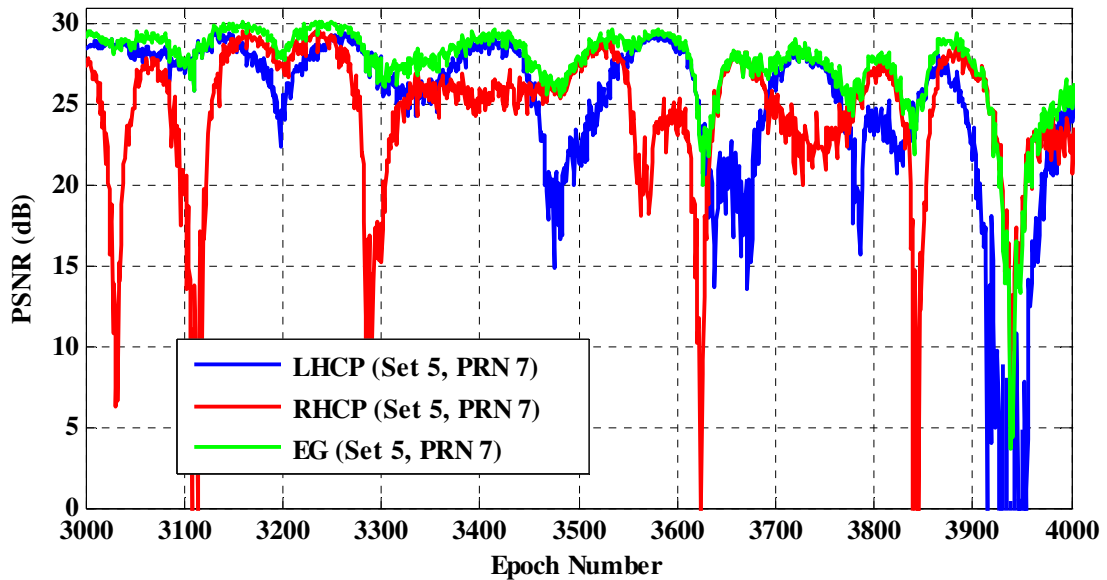
By combining independent samples and utilizing the diversity system, signal fading will be reduced and the output SNR will have a smoother curve. In order to compare the received signal fades with the combined ones, the *Deflection Coefficient* at each epoch is quantified. In statistical detection signal processing, this can be accomplished by (Kay 1998)

$$d^2 = \frac{(E(x; H_1) - E(x; H_0))^2}{\text{var}(x; H_0)} . \quad 5-9$$

Here, the deflection coefficient is quantified as the signal post-correlation SNR (PSNR) and is utilized to depict the ability of the proposed method for signal fading mitigation. Figure 5.16 shows a part of the quantified PSNR for two different satellites. As it can be seen, the final combined signals carry smoother SNR and experience less fading.



(a) PRN 23 from data set 3



(b) PRN 7 from data set 5

**Figure 5.16: Signal fading mitigation at the output of EG combiner**

#### 5.1.4.5 LCR and AFD analysis

In the GPS communication link, due to the motion of the transmitter (satellites) and/or the receivers, the envelope fading varies and the fading rate and envelope amplitude are function of time. In order to obtain at the quantitative level a description of the fading occurring in the channel, the level crossing rate (LCR) and average fade duration (AFD) are quantified as two statistical parameters of the channel (Blaunstein & Andersen 2002).

LCR is quantified as the expected rate at which the received signal envelope crosses a specific level, in either the positive or negative going direction. In Figure 5.17, the number of times that the signal envelope crosses the level  $X$  in the positive direction in  $T$  second is 4 and the LCR is equal to  $4/T$  times per second.

The AFD is the average duration of a fade below any given depth. In other words, AFD is quantified as the average period of time for which the received signal envelope is below a specific level. As an example, in Figure 5.17, the average time that the signal is below the level  $X$  provides the AFD for the given signal and is quantified as

$$AFD = \frac{T_1 + T_2 + T_3 + T_4}{4}. \quad 5-10$$

The theoretical equations of LCR and AFD for Rayleigh fading channels are provided in the literature such as Blaunstein a& Andersen (2002).

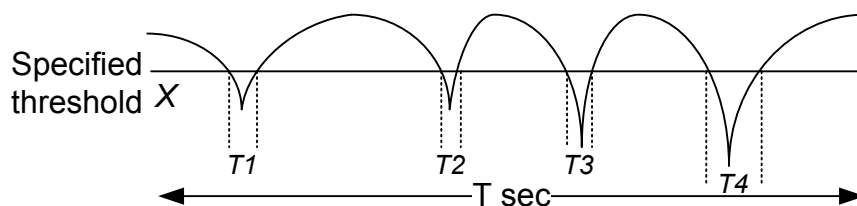


**Figure 5.17: An example for illustration of definition of LCR and AFD**

The threshold for the LCR and AFD quantification procedure can be defined based on the level (signal envelope) or signal SNR. Since in GPS applications signal SNR comparison is use extensively in this work, the signal PSNR is utilized for LCR and AFD quantification and the thresholds are determined based on that.

Both AFD and LCR plots for PRN 22 in the first data set are shown in Figure 5.18 and Figure 5.19. The LCR is shown using a logarithmic scale to depict the signal SNR in dB. For example, this graph shows that the combined signal (EG) crosses the -10 dB threshold much less than the RHCP and LHCP signals. In addition, the LCR curve peaks in the RHCP and LHCP signals are around the threshold of -10 dB while that of combined signals is located at around -6 dB lower than the signal rms. This graph implies

lower fading for the combined signal in overall. The AFD plot shows improvement in combined signal compared to both RHCP and LHCP signals. This graph shows that the combined signal (EG) stay less than single antennas in the fading zone.

In order to show the fading mitigation in the combined signal rather than the single antenna for all data sets, the AFD and LCR are quantified for all PRNs and data sets for a specific threshold which is 10 dB less than the signal rms. These are plotted in Figure 5.20. The lower AFD in the combined signals shows that the proposed method results in lower average fading duration in the combined signal and it can be implied that the signal can be tracked and analyzed for navigation data extraction with smaller fades. In addition, the LCR in the received signal is reduced which represent lower fading in combined signal (EG) for all datasets and PRNs.

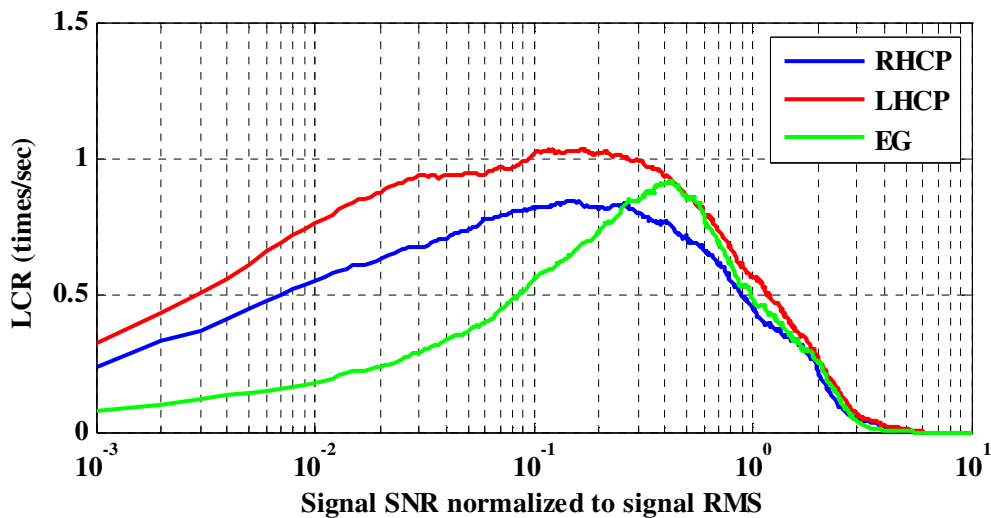


Figure 5.18: The LCR for PRN 22, set 1

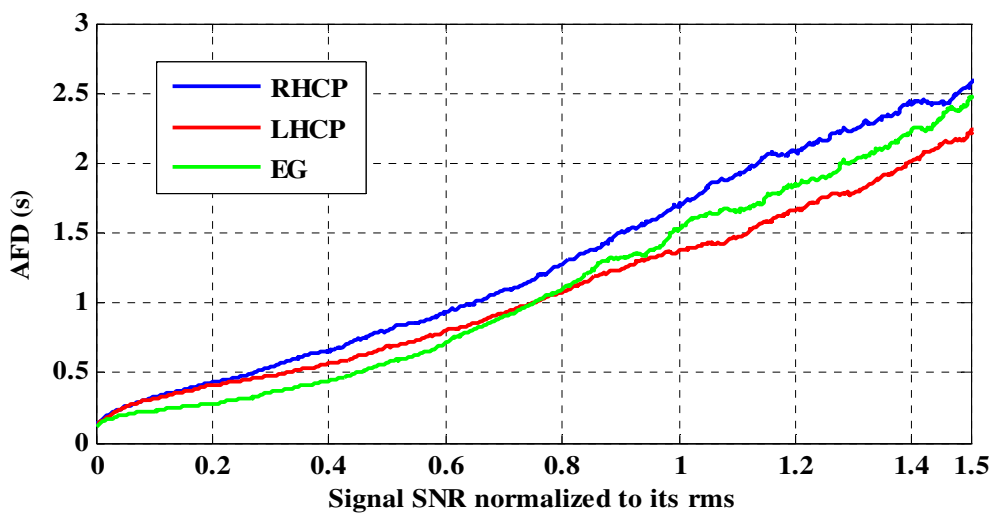


Figure 5.19: The AFD for PRN 22, set 1

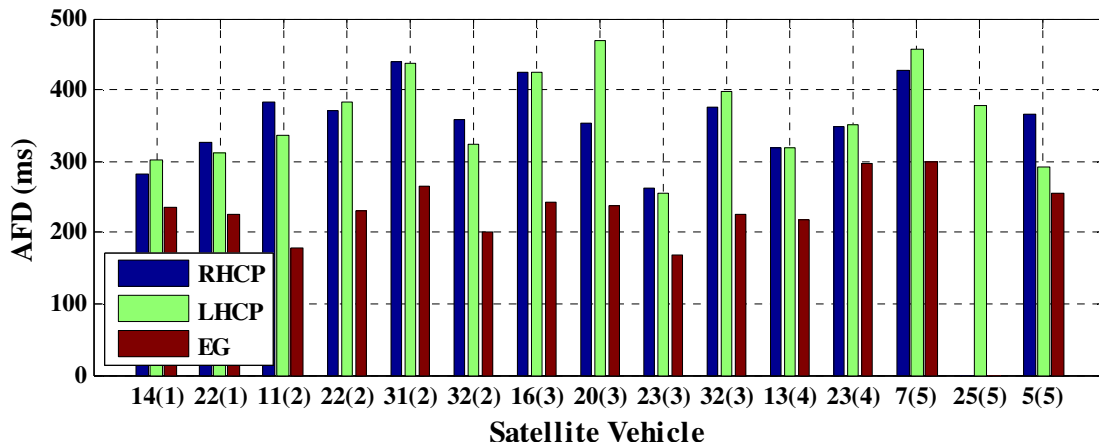
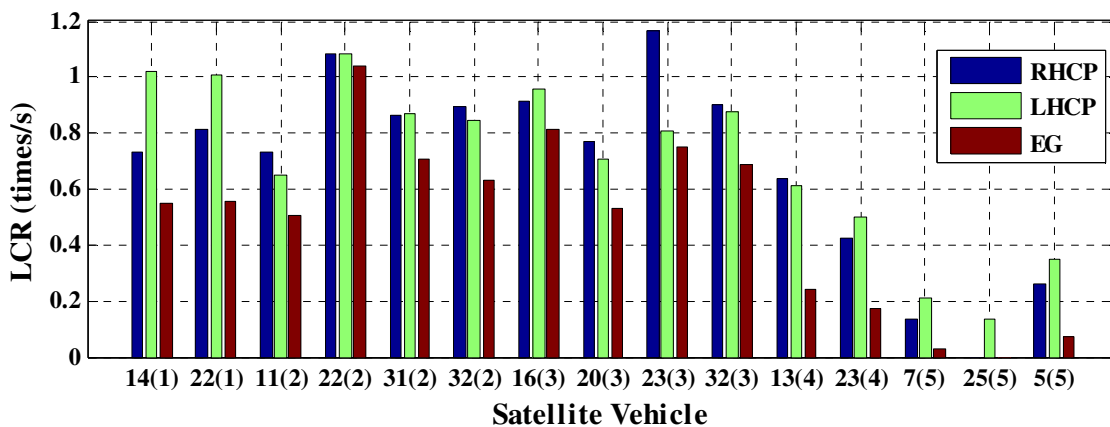
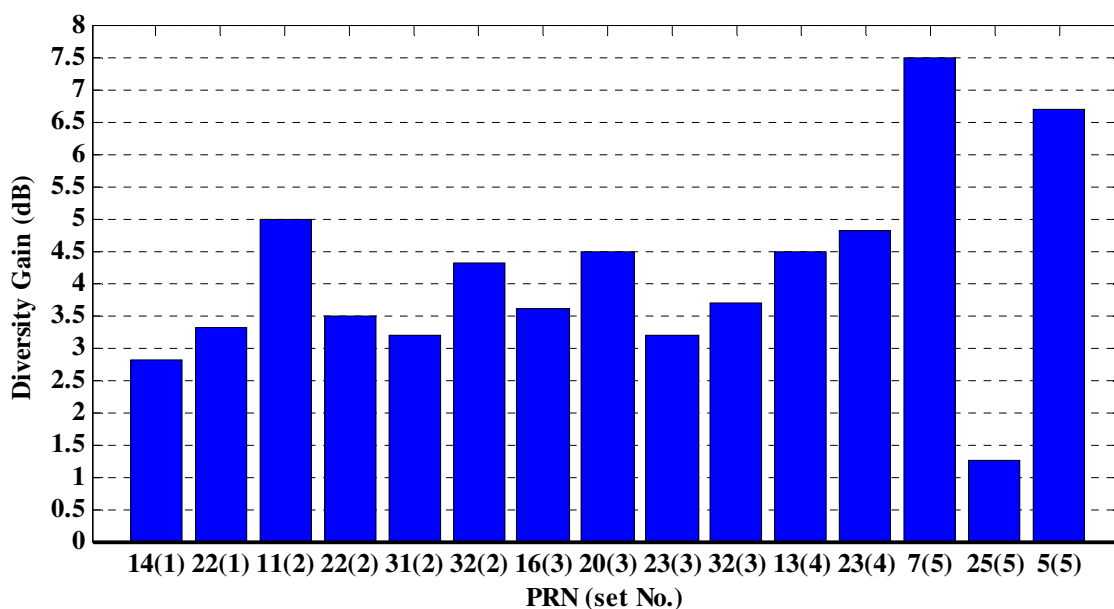


Figure 5.20: AFD and LCR for all satellites for a threshold of 10 dB less than each signal rms

#### 5.1.4.6 Diversity Gain

The diversity gain for a specific probability of false alarm was quantified using the method proposed in the previous chapter and is presented in Figure 5.21. As discussed previously, the diversity gain depends on the specified target values in the ROC curve. Here, the diversity gain is measured for the target probability of false alarm of 0.01. In addition, the diversity gain is a function of the correlation coefficient and the signal probability of detection as well. Here, the highest diversity gain belongs to PRN 7 in data set 5. According to Table 5.3, the cross correlation coefficient of received signals of this satellite is only 0.14. Besides, based on the Figure 5.15, both received signals carry a relatively high probability of detection. To the contrary, PRN 25 in this data set carries the lowest diversity gain since one of the branches (RHCP one) carries the Rician distribution (see Table 5.2) and also there is a relatively high cross correlation coefficient (0.47) between received signals of this satellite (see Table 5.3).



**Figure 5.21: Diversity gain of proposed circular polarization diversity system**

Overall and as expected, a reasonable diversity gain (between 3 to 5 dB) has been achieved by combining two low correlated RHCP and LHCP signals in an indoor situation for most satellites.

## **5.2 Comparison of polarization and spatial diversity**

The next set of experiment is dedicated to the comparison of two forms of polarization diversity, namely circular and linear polarization, with the spatial diversity structure. The spatial diversity is established by two spaced apart RHCP antennas. As previously explained, the fading of received signals in a high multipath environment is a random function of antenna location (Rappaport 2002). Moreover, a dual polarized antenna consisting of two linear antennas located perpendicular relative to each other, called vertical and horizontal antenna, is utilized to create a linear polarization diversity structure. The principle of this diversity structure is based on the fact that the amplitude and the phase of the vertical and horizontal components of the reflected signals vary independently (Rappaport 2002). In the next section, the test setup used to accomplish this experiment is described.

### ***5.2.1 Test setup***

In order to achieve the objectives, three data sets in two different indoor locations were collected. The data collection specifications are addressed in Table 5.5. Each data set consisted of three consecutive data collections with different diversity schemes including spatial, circular polarization (CP) and linear polarization (LP) structures. In each case, the diversity branches output along with a reference antenna were connected to a synchronized triple port down-converter/digitizer to collect synchronous raw IF samples in the GPS L1 band for all inputs.

A reference antenna was located in an un-obstructed view of the sky and within 30 metres of the indoor diversity structures. It was used to remove the navigation data bit from the received signals to increase the coherent integration time up to 100 ms. The spatial diversity scheme consisted of two RHCP GPS L1 antennas spaced apart 1.5 wavelength (30 cm). Two Commercial dual polarized antennas were utilized to create polarization diversity structures. One of them includes RHCP and LHCP GPS L1C/A signal antennas and the other one is formed from two orthogonal linear GPS L1C/A antennas called the horizontal and vertical antenna (Figure 5.22).

**Table 5.5: Data sets and selected satellites**

Set#	Date	Location	Diversity scheme	Start time	Selected SV's
1	22Oct2009	Energy high Bay	CP	3:27 p.m.	2, 4, 12
			LP	3:42 p.m.	2, 4, 12
			Spatial	4:05 p.m.	2, 4, 12
2	4Dec2009	ICT corridor	CP	9:20 p.m.	31
			Spatial	9:29 p.m.	31
			LP	9:37 p.m.	31
3	7Dec2009	Energy high Bay	CP	11:43 a.m.	2, 12, 30
			LP	11:56 a.m.	2, 12, 30
			Spatial	12:08 p.m.	2, 12, 30

The indoor antennas were mounted on a linear motion table to create moving scatters in an indoor GNSS channel. The table traversed a 2.8 m (2x1.4 m) distance during each lap. As discussed previously, its speed was chosen to be 2 cm/s for 100 ms pre-integration time to guarantee that more than 99% of the signal remained unaliased or within the Nyquist interval.

The first and third data set collections were performed in a laboratory with a high metallic ceiling called the Energy High Bay in the CCIT building of the University of Calgary shown in Figure 5.23. The first data collection was started at 3:20 p.m. on 22 October 2009 and the third one was collected at 11:40 a.m. on 7 December 2009. The second data set was carried out in the corridor of another University of Calgary building (called ICT) having large window panes in both the south and north direction and a concrete ceiling as shown in Figure 5.24. This test was started at 4:10 p.m. on 4 December 2009. These data collections lasted roughly 45 minutes and consisted of three consecutive data collection with various diversity structures. According to the corresponding sky plots showed in Figure 5.25, appropriate GPS satellites with a reasonable SNR output are selected from each data collection, as tabulated in Table 5.5. Using the software program described in Section 5.1.3, the results for this experiment are analyzed and explained in the next section.

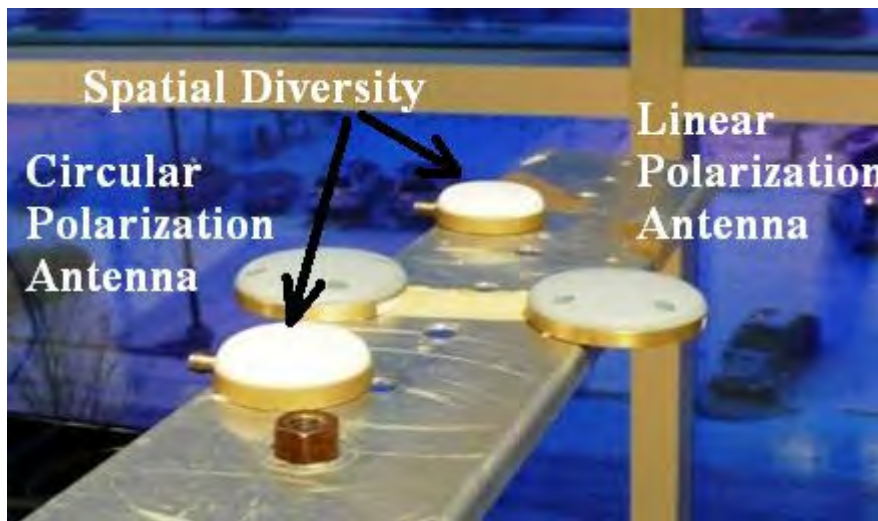


**Figure 5.22: Antenna mounts on linear moving table**



**Figure 5.23: Energy High Bay, CCIT building, University of Calgary**

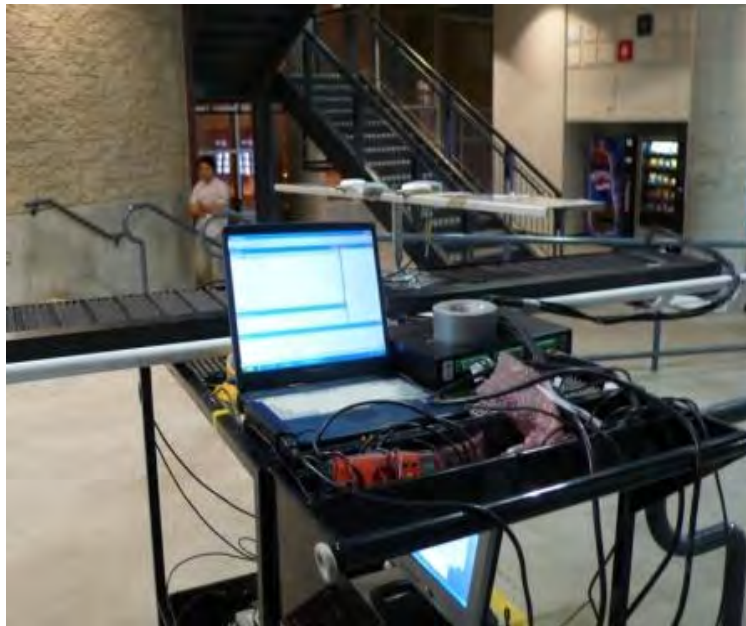
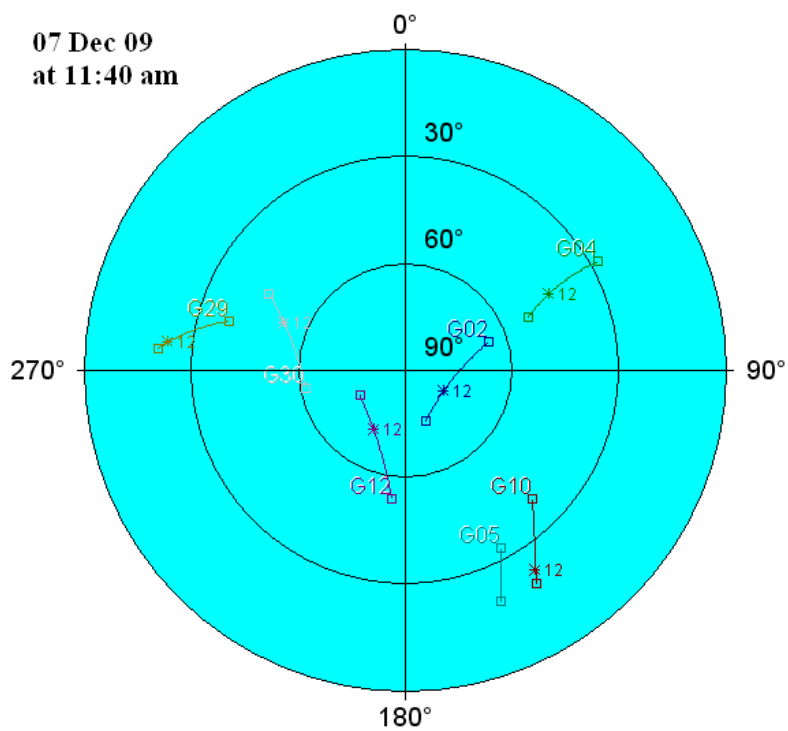
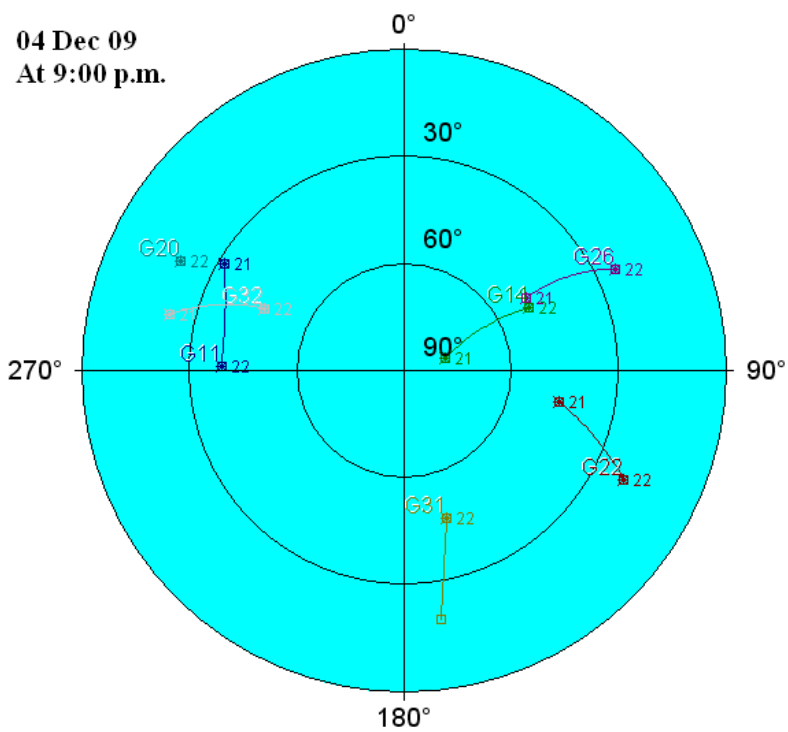


**Figure 5.24: ICT corridor, spatial diversity structure**

07 Dec 09  
at 11:40 am



04 Dec 09  
At 9:00 p.m.



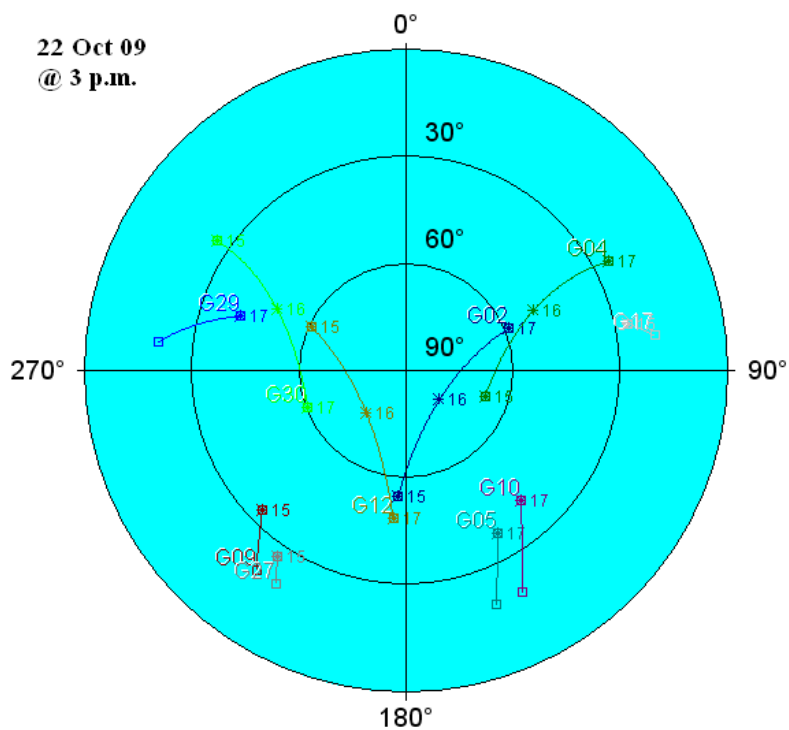


**Figure 5.25: Test sky plots - Polarization versus spatial diversity comparison**

## 5.2.2 Experimental results

### 5.2.2.1 Channel Measurement

In Figure 5.26, fitted Rician and Rayleigh distributions on measured signal amplitudes for linear polarized antennas (vertical and horizontal) are plotted. In this figure, the  $K$  factor for Rician distributions are close to zero and it can be seen that the Rician distribution roughly overlap the Rayleigh one. In addition, Table 5.6 shows the estimated  $K$  factors for all selected satellites. As discussed, small  $K$  factors represent Rayleigh fading distribution and, hence, the EC and EG combining methods can be considered as optimal detection approaches.

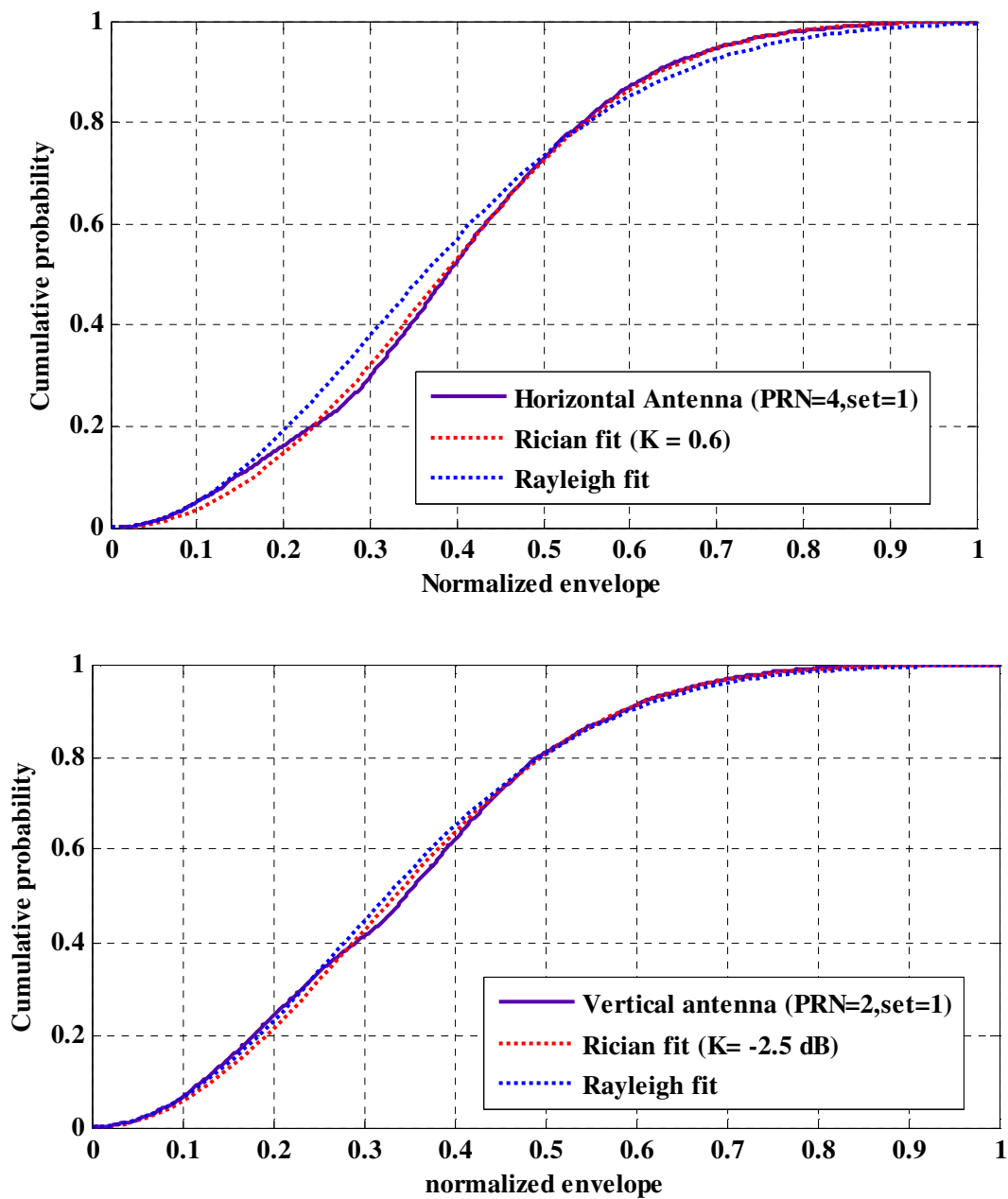


Figure 5.26: Cumulative probability of received signals and fitted Rician Rayleigh distribution

**Table 5.6: K factors for received signals in indoor situation**

PRN# (set#)	K factors (dB)					
	RHCP	LHCP	Vertical	Horizontal	RHCP1	RHCP2
2(1)	-66	-9.6	-2.4	-62	-64	-60
4(1)	-3.8	-0.64	-42	0.64	-3.8	-1.4
12(1)	-60	-4.7	-44	-52	-11	-3.7
31(2)	-3	-2.2	-61	-57	-67	1.88
2(3)	-59	-63	-6	-59	-60	-58
12(3)	-63	-48	-5	-58	-60	-52
30(3)	-14	0	0.5	-0.46	-7.7	-17

#### 5.2.2.2 Correlation Coefficient

Herein, the complex correlation coefficient between received signals in each diversity branches is empirically evaluated and presented in Figure 5.27. In the spatial diversity case the correlation coefficient value may increase up to 0.6 under some circumstances (data set 2, PRN 31). According to Table 5.6, the received signal in this set of data (31(2)) is totally Rayleigh distributed for the RHCP1 branch and close to Rician for the RHCP2 branch. This shows reception of a dominant signal through the RHCP2 antenna and it can lead to higher correlation between these two branches.

According to the above results, the correlation coefficient for the majority of the data sets is less than 0.3, which results in a reasonable diversity gain.

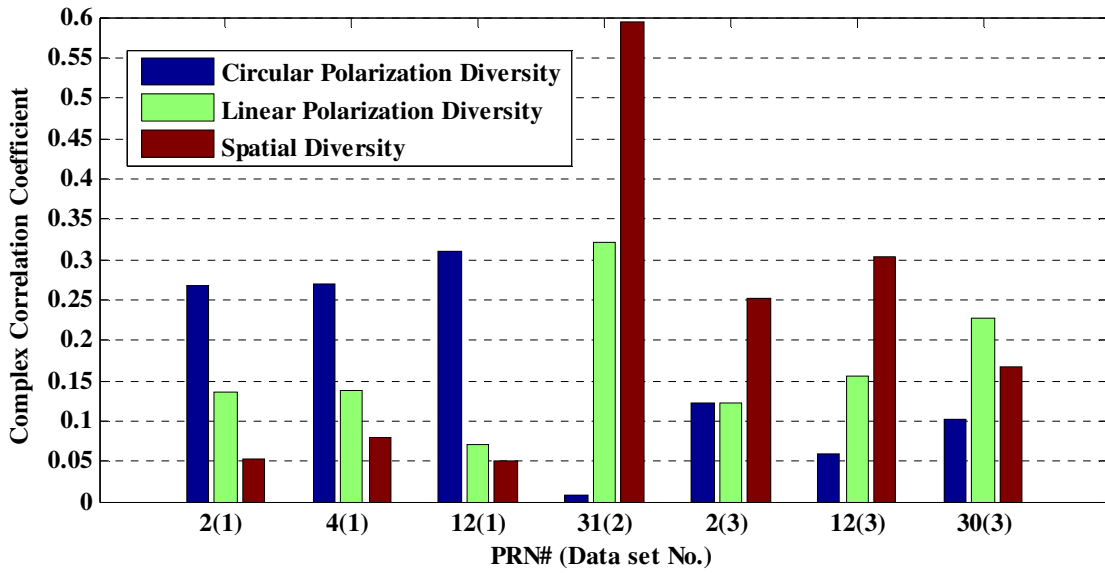


**Figure 5.27: Correlation coefficients between received signals**

#### 5.2.2.3 Average input SNR:

As mentioned, the average input SNR plays a crucial role in the efficiency of a diversity system. The average input SNR is quantified as

$$SNR = \frac{\sigma_s^2}{\sigma_w^2}, \quad 5-11$$

where  $\sigma_s^2$  and  $\sigma_w^2$  are the signal and additive noise variance. Practically, the received signal amplitude under  $H_1$  and  $H_0$  can be distinguished and collected. The received signal envelope is formulated as a function of Inphase and Quadrature components as

$$|x_m|^2 = x_I^2 + x_Q^2, \quad 5-12$$

where

$$\begin{aligned} p(x_I; H_0) &= p(x_Q; H_0) \sim N(0, \sigma_w^2 / 2) \\ p(x_I; H_1) &= p(x_Q; H_1) \sim N(0, (\sigma_s^2 + \sigma_w^2) / 2) \end{aligned} \quad 5-13$$

In a Rayleigh channel, since the input signal components have zero mean Gaussian distributions, by applying the expectation value operator on the received signals under  $H_1$  and  $H_0$ , according to the Equation 5-12, one obtains

$$E\left[|x_m|^2\right]\Big|_{H_1} = E\left[x_I^2\right]\Big|_{H_1} + E\left[x_Q^2\right]\Big|_{H_1} = \sigma_s^2 + \sigma_w^2 \quad 5-14$$

and

$$E\left[|x_m|^2\right]\Big|_{H_0} = E\left[x_I^2\right]\Big|_{H_0} + E\left[x_Q^2\right]\Big|_{H_0} = \sigma_w^2 \quad 5-15$$

respectively. As a result, the mean SNR for a single antenna can be calculated using the expected value of the input signal power as follows:

$$\frac{E\left[x^2\right]\Big|_{H_1}}{E\left[x^2\right]\Big|_{H_0}} = \frac{\sigma_s^2 + \sigma_w^2}{\sigma_w^2} = SNR + 1 \quad 5-16$$

The average input SNR values for different diversity structures are shown in Figure 5.28. According to these plots, the circular polarization and spatial diversity systems consist of equal input powers in different branches, whereas the linear polarization diversity carries the highest level of SNR difference among the rest of the systems. This phenomena results from variation in the polarization loss factor (PLF) for linear antennas, as described in Chapter 3. The antennas were fixed to the linear table and the signals carry almost a fixed angle of arrival during the data collection. As shown in Figure 3.6 to Figure 3.8, the total polarization loss for vertical and horizontal antennas vary significantly under the same azimuth and elevation angle.

As discussed earlier, the unequal average power in received signals by two orthogonal linear antennas can lead to lower diversity gain in this structure rather than the spatial and circular polarization systems.

### 5.2.2.4 Detection performance

Having analyzed the probability distribution function (PDF) of each individual branch and the combined signal under  $H_0$  and  $H_1$ , the ROC curves can be plotted using a threshold as an intermediate variable. Figure 5.29 shows the probability of detection of all selected satellites for each diversity system at a specific probability of false alarm ( $P_{FA}=0.01$ ). The probability of detection specifies the input branches efficiency.

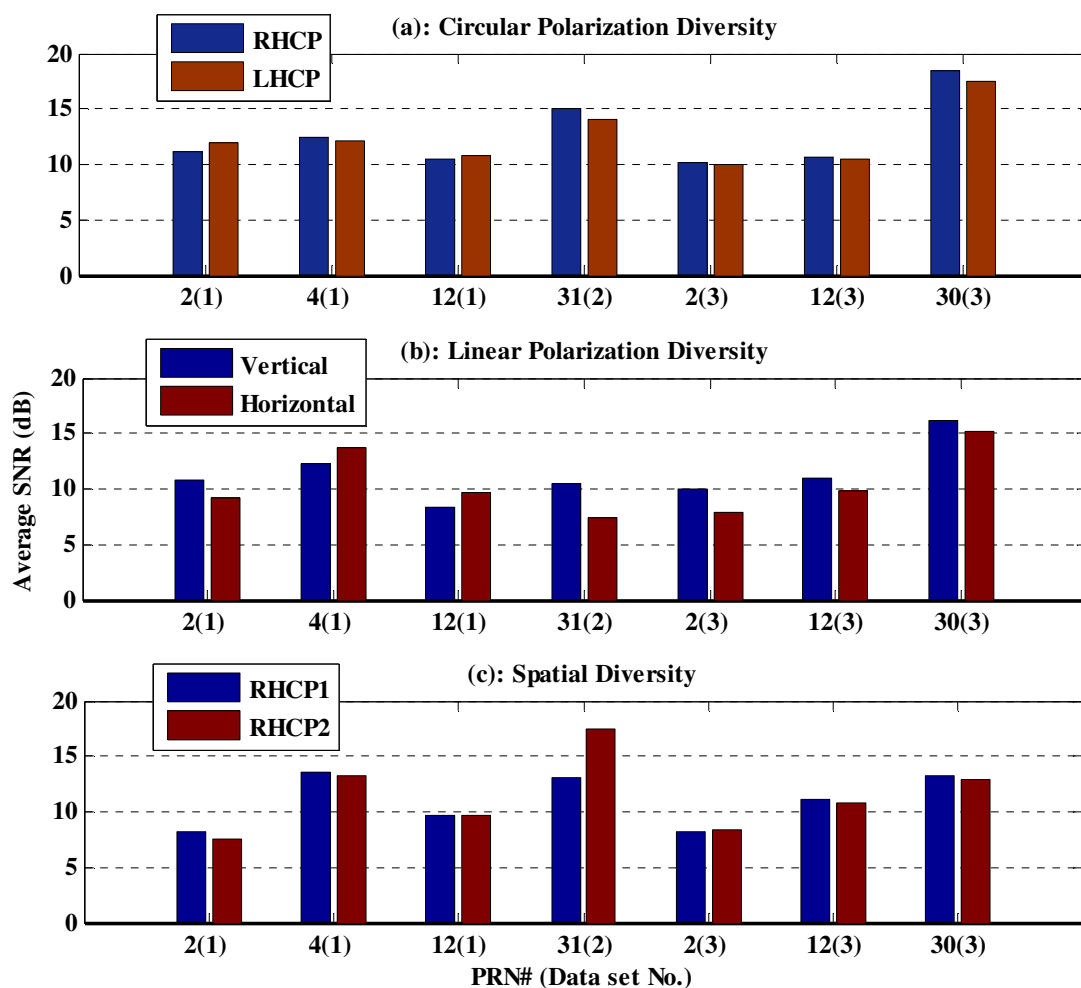


Figure 5.28: Average input SNR

As shown, the polarization and the spatial diversity systems utilizing the circularly polarized antenna have higher detection performance than the polarization diversity utilizing the linear polarized antenna. This is due to the existence of unequal received signal power in different diversity branches of the linearly polarized system and it can lead to lower overall diversity gain in this structure.

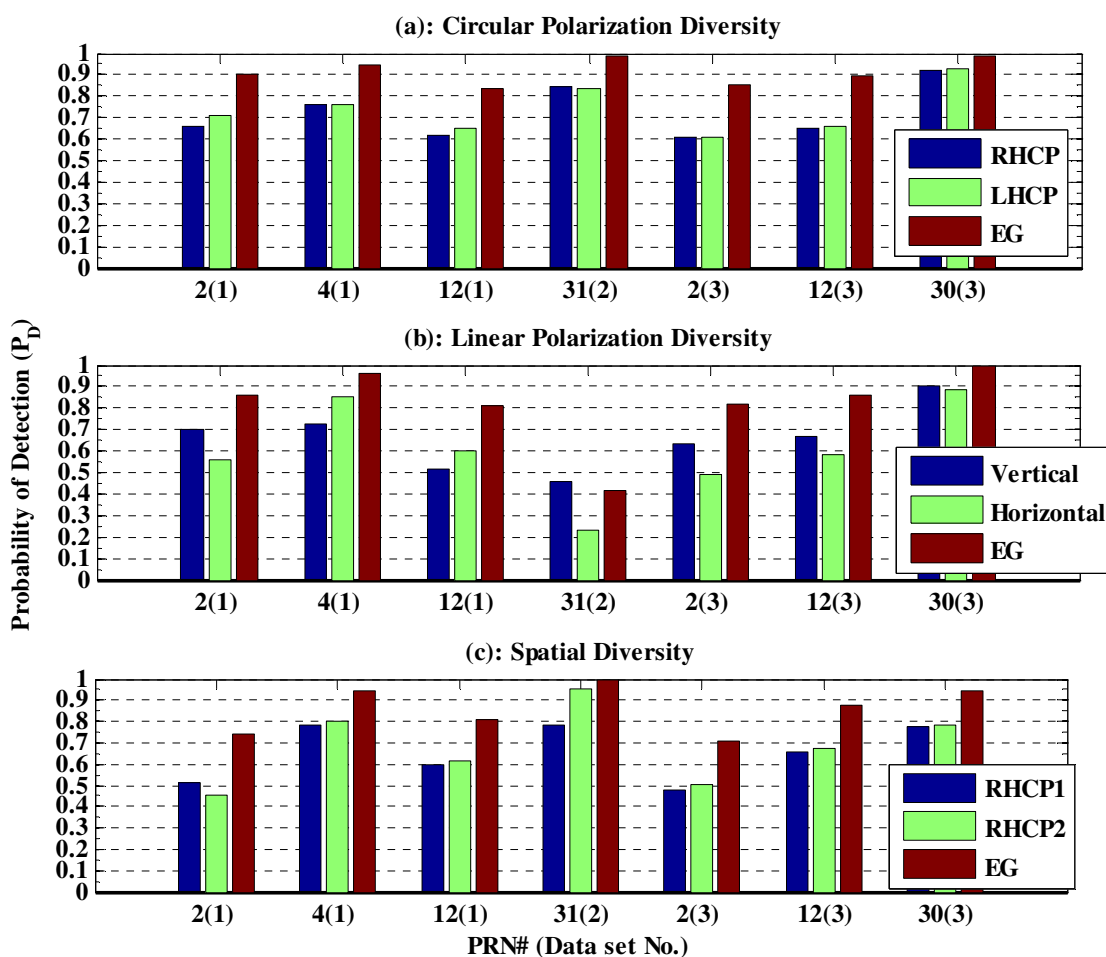


Figure 5.29: Probability of detection for various diversity schemes in  $P_{FA}=0.01$

### 5.2.2.5 LCR and AFD analysis

Herein the analysis of the AFD and LCR is performed on signal SNR as well. Figure 5.30 shows the LCR analysis for received signals on all data sets. The combined signals in all diversity structures show less fading compared to the single antennas. Figure 5.31 represents the AFD of the received signals and the combined ones. This represents the improvement in combined signals in all diversity structures. According to the provided results, overall all diversity structures result in the same improvement in fading mitigation.

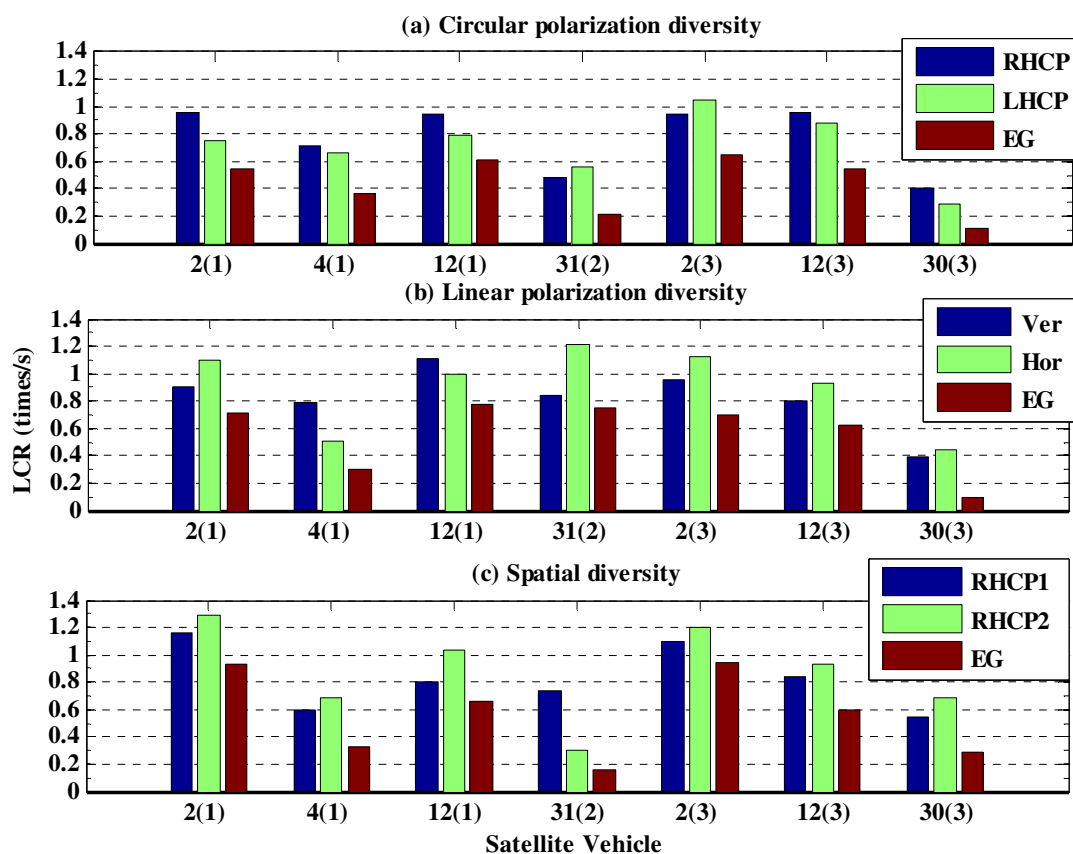
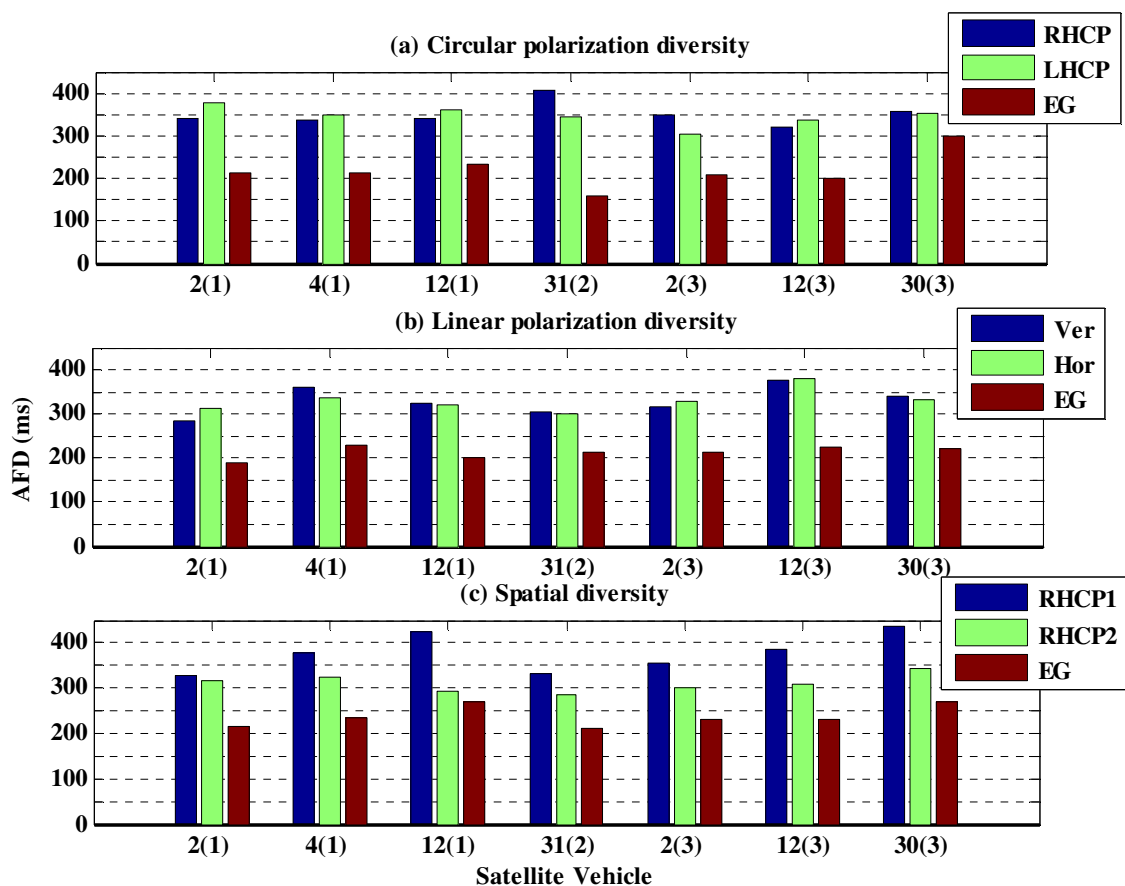


Figure 5.30: LCR analysis for -10 dB lower than signal rms



**Figure 5.31: AFD analysis for -10 dB lower than signal rms**

#### 5.2.2.6 Diversity Gain

The diversity gain for a specific design point ( $P_{FA}=0.01$ ) is quantified as the reduction in the input average SNR utilizing a diversity system. The measured diversity gains for different diversity systems are plotted in Figure 5.32. Here, the diversity gain is measured for a probability of false alarm equal to 0.01. The average diversity gain for CP, LP and spatial structure is 4.3 dB, 2.6 dB and 3.25 dB, respectively. As shown, circular polarization leads to higher diversity gain (up to 6.3 dB) and consequently higher performance in overall. According to the provided analyses, the lower correlation coefficient in spatial diversity between two RHCP and LHCP received signals rather than

two RHCP ones can explain the higher performance in circular polarization diversity. In addition, as discussed thoroughly in Chapter 3, since in indoor environments the GNSS signal is reshaped to elliptically polarized waves including RHCP and LHCP signals, circular polarization diversity employs the advantages of LHCP waves to improve GNSS signal detectability. However, spatial diversity systems take only the power of the RHCP component of the received signals, which leads to lower processing gain. On the other hand, power level differences in the linear polarization system branches caused lower diversity gain in such a system.

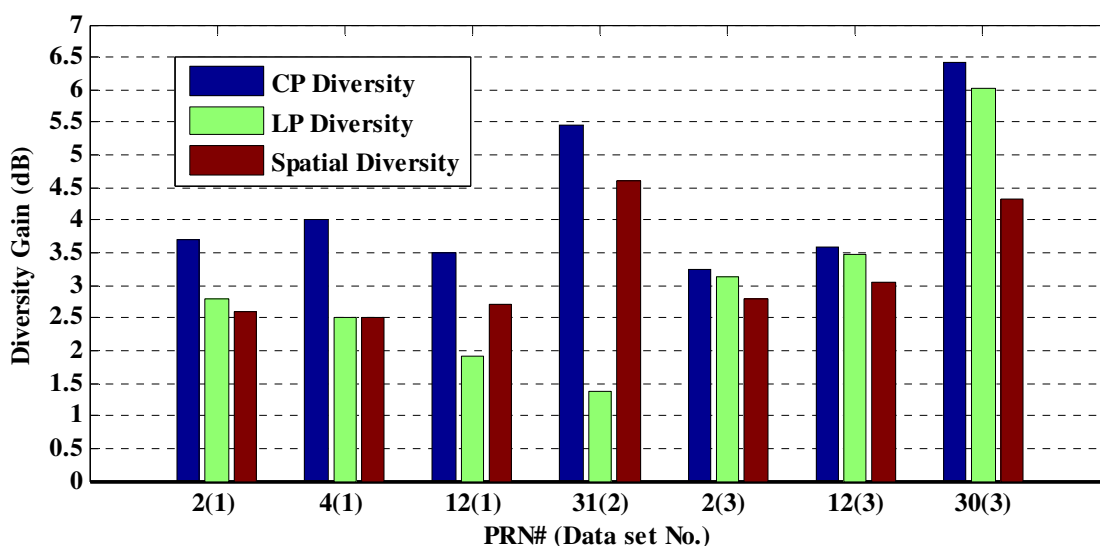


**Figure 5.32: Diversity gain for various diversity schemes**

### 5.3 Summary

In this chapter the polarization diversity and its performance for GPS signals in indoor and high multipath environments were examined. Two different experiments have been described and the results analyzed comprehensively. In the first test, the polarization diversity has been analyzed individually. It was shown that in indoor environments a reasonable diversity gain can be captured from polarization diversity in GPS applications.

In the second experiment setup the polarization diversity utilizing two different orthogonal polarized antennas namely the linear and circular polarization diversity was compared with the spatial diversity. According to the provided results the polarization diversity leads to higher diversity gain and detection performance.

## Chapter Six: Conclusion and future works

In this chapter, conclusions pertaining to using polarization diversity on GPS signals in indoor environments are discussed. This is followed by a discussion of the limitations of this approach along with the recommendations for future work.

### 6.1 Conclusions

According to the assumptions for the channel model, the likelihood ratio test function as both detector and combiner has been analyzed theoretically for various signal branches situations in term of the correlation coefficient and average input power. It was shown that the Equal Gain (EG) combiner results in the same performance as the estimator correlator (EC) for low cross correlation coefficient between input signals (less than 0.6) and low power difference between received signals (less than 10 dB difference). According to the provided results for the correlation and power difference between received RHCP and LHCP signals in indoor environments, EG was utilized as the detector and combiner for the rest of the experiments since it is less computationally intense.

In order to analyze the proposed method experimentally, a large number of data sets have been collected in various indoor environments. An analysis of the distribution of received signals showed that the indoor channel for both RHCP and LHCP signals follows the Rayleigh distribution for most cases. This confirms the assumptions made for the distribution of received signals in the theoretical analysis.

Complex cross correlation coefficient measurements between received signals were quantified in the next step. These showed that the received RHCP and LHCP signals in indoor areas have sufficient low correlation to result in a high diversity gain.

The majority of measurements showed a magnitude of complex correlation coefficient of less than 0.3. Examining the probability of detection of the received signals for a target probability of false alarm showed that both RHCP and LHCP signals carry the same detectability and efficiency in indoor environments. Besides, the average input SNR for the circular polarization diversity scheme represents the power balance in input branches of this diversity structure.

By combining the received signals using the equal gain combiner, it was observed that the signal detectability is significantly improved. The measured probability of detection of combined signals for the target probability of false alarm showed 15% improvement in probability of detection in average on the satellites analyzed. Using deflection coefficients, the post-SNR for both single antennas and combined signals were quantified. The results show smoother PSNR for the combined signals and lower fading in received signals. Besides, average fade duration (AFD) and level crossing rate (LCR) measurements show lower fading duration and LCR in the combined signals compared to the single antennas. The diversity gain for the proposed diversity structure was quantified as well. It showed up to 7.5 dB gain for the polarization diversity for a specific design point ( $P_{FA} = 0.01$ ). On the average, for the determined design point, almost 4 dB diversity gain was observed on the satellites analyzed.

In addition to examining the circular polarization diversity individually, some experiments were performed to compare the circular polarization diversity with the spatial and linear polarization diversity. All diversity structures resulted in sufficiently low cross correlation coefficient between received signals. While the circular polarization and spatial diversity led to a very low power difference between input branches,

according to the results obtained, the linear polarization diversity resulted in unbalanced input average SNR. The diversity gain for all aforementioned diversity structures was quantified as well. According to the results analyzed for the target design point, the circular polarization diversity leads to higher diversity gain in indoor environments, compared to spatial and linear polarization diversity.

Since the GPS signals polarization in dense multipath environments transforms to the elliptical polarization including both RHCP and LHCP signals, using two RHCP and LHCP antennas results in absorbing more signal power in indoor areas. It was observed that in some cases the average SNR received through the LHCP antenna is higher than that of the RHCP antenna.

## **6.2 Limitations and future works**

As a novel diversity structure in GPS application, the research presented herein focused on justification of polarization diversity for GPS signals in indoor environments. Considering the theoretical and experimental results in this research, polarization diversity improves the GPS signals detectability in indoor environments. However, more research and future work are required in order to practically resolve the indoor localization problems. Some recommendations for future works are listed below.

### ***6.2.1 More analysis under various wireless channel assumptions***

The assumption utilized herein was based on Rayleigh fading where there is not a Line Of Sight (LOS) signal component. In some situations LOS signals are available indoors. Besides, a receiver may be utilized in both indoor and outdoor situation, therefore considering the Rician type fading and optimizing the detector for both the Rayleigh and the Rician situations might be an interesting research topic.

### ***6.2.2 Combining with other diversity structures***

The main limitation of polarization diversity is the limited number of branches. As discussed, to establish the polarization diversity, orthogonally polarized antennas are required. Therefore, a polarization diversity structure forms with only two branches, namely RHCP and LHCP antennas. In order to overcome this limitation and increase the number of branches in the diversity structure, the polarization diversity needs to be combined by other diversity structures. Two dual polarized antennas separated by half a wavelength can form a combination of spatial and polarization diversity and result in a diversity structure with four input branches.

### ***6.2.3 Implementation of the diversity system in parameter estimation level***

Having detected the available satellites, the navigation data should be extracted from the received signals. Defining an appropriate tracking method to utilize the information of both RHCP and LHCP signals as observations to estimate code and frequency Doppler and GPS navigation data bits of received signals might be an interesting research area. In order to design a tracking method properly, the input signal properties should be identified accurately. In addition, the relation between the RHCP and LHCP signal properties such as code and frequency Doppler should be evaluated. This can be accomplished by analyzing the collected GPS data in high multipath environments.

**References**

- Aguire, S., L. H. Loew, and Y. Lo (1994) "Radio Propagation Into Buildings at 912,1920, and 5990 MHz Using Microcells" Proceedings Third ICUPC, 129-134.
- Balanis, C. A. (2001) "Antenna Theory: Analysis and Design" John Wiley & Sons, 2nd edition.
- Balanis, C. A. (1989) "Advanced Engineering Electromagnetics" New York: John Wiley & Sons.
- Bancroft, J.B., G. Lachapelle, M.E. Cannon, and M.G. Petovello (2008) "Twin IMU-HSGPS Integration for Pedestrian Navigation" Proceedings of GNSS08 (Savannah, GA, 16-19 Sep, Session E3), The Institute of Navigation, 11 pages.
- Blaunstein, N., and J. B. Andersen (2002) "Multipath Phenomena in Cellular Networks" Artech House, ISBN 1-58053-185-7
- Bolcskei, H., D. Gesbert, C.B.Papadias, and A-J van der Veen (2006) "Space-Time Wireless Systems – From Array Processing to MIMO Communications" Cambridge University Press, UK, July
- Broumandan, A. (2009) "Enhanced Narrowband Signal Detection and Estimation with a Synthetic Antenna Array for Location Applications" PhD Thesis, published as

Report No 20292, Department of Geomatics Engineering, The University of Calgary, Canada.

Cannon, M. E., G. Lachapelle, G. MacGougan, P. Boulton, and A. Read (2003) "Mobile Telephony: Testing a High Sensitivity GPS Receiver in Weak Signal Environments," GPS World, March

Clarke, R. (1968) "A statistical theory of mobile radio reception," Bell System Technical Journal, no. 2, pp. 957-1000

Colburn J. S., Y. Rahmat-Samii, M. A. Jensen, and G. J. Pottie, (1998) "Evaluation of personal communications dual-antenna handset diversity performance," IEEE Trans. Veh. Technol., vol. 47, pp. 737-744, Aug.

Gao, J. (2007) Development of a Precise GPS/INS/On-Board Vehicle Sensors Integrated Vehicular Positioning System, PhD Thesis, published as UCGE Report No. 20255, Department of Geomatics Engineering, University of Calgary, Canada.

Gao, G., and G. Lachapelle (2008) "A Novel Architecture for Ultra-Tight HSGPS-INS Integration" Journal of Global Positioning Systems, 7, 1, 46-61.

Haykin, S. (2000) "Communication Systems" 4th Edition, 2000, John Wiley & Sons, Inc.

Horikoshi, J., K. Tanaka, and T. Morinaga (1986) "1.2GHz Band wave propagation measurements in concrete Buildings for indoor Radio communications" IEEE Transactions on Vehicular Technology, Vol.VT-35, no.4, 146-152

Hu, T. (2006) Controlled Indoor GPS Signal Simulation, MSc Thesis, Department of Geomatics Engineering, University of Calgary, Canada, (Available at <http://plan.geomatics.ucalgary.ca>)

Hyeon, S.,Y. Yun, H. Kim, and S. Choi (2008) "Phase Diversity for an Antenna-Array System With a Short Interelement Separation" IEEE TRANSACTIONS ON VEHICULAR TECHNOLOGY, VOL 57; NUMB 1, pages 206-214

Ioannides, R. T., L. E. Aguado, and G. Brodin (2007) "Diverse Signals Combinations for High-Sensitivity GNSS" Journal of Navigation, Cambridge University Press, 60, 3, 497-515.

Izadpanah A. (2009) "Parameterization of GPS L1 multipath using a dual polarized RHCP/LHCP antenna" MSc Thesis, published as Report No. 20280, Department of Geomatics Engineering, University of Calgary, Canada.

Jakes, W. C. (1974) "Microwave Mobile Communications" IEEE pres 1974.

Kaplan, E. D. and C. Hegarty, Understanding GPS Principles and Applications. Artech

House, UK, 2006.

Kay, S. M. (1998) "Fundamentals of Statistical Signal Processing" Part-2, Detection Theory, Prentice Hall PTR, NJ

Kazemi, P.L., and C. O'Driscoll (2008) "Comparison of Assisted and Stand-Alone Methods for Increasing Coherent Integration Time for Weak GPS Signal Tracking" Proceedings of GNSS08 (Savannah, GA, 16-19 Sep, Session C4), The Institute of Navigation, 11 pages.

Klukas, R., O. Julien, L. Dong, M. E. Cannon, and G. Lachapelle (2004) "Effects of Building Materials of UHF Ranging Signals," GPS Solutions, Vol. 8, No. 1, pp. 1-8, Springer Verlag, April 2004

Lachapelle, G., H. Kuusniemi, D. T. H. Dao, G. MacGougan, and M. E. Cannon (2003) "HSGPS Signal Analysis and Performance under Various Indoor Conditions," in Proceedings of ION GPS/GNSS, 9-12 September, Portland, OR, pp. 1171-1184, U.S. Institute of Navigation, Fairfax VA

Lee, W. C. Y. (1998) "Mobile Communications Engineering" McGraw Hill Book Co., second edition

- Lemieux, J., M. El-Tanany and H. M. Hafez (1991) "Experimental Evaluation of Space/Frequency/Polarization Diversity in the Indoor Wireless Channel" IEEE Trans. on Vehicular Technology, Vol. VT-40, No. 3, August, pp. 569-574.
- Lim, D.W., S.W. Moon, C. Park, and S.J. Lee (2006) "L1/L2CS GPS Receiver Implementation with Fast Acquisition Scheme" Position, Location, And Navigation Symposium, IEEE/ION, 25-27 April, pp 840- 844.
- MacGougan, G. D. (2003) "High Sensitivity GPS Performance Analysis in Degraded Signal Environments" MSc Thesis, Department of Geomatics Engineering, University of Calgary, Canada, (Available at <http://plan.geomatics.ucalgary.ca>)
- Mahfuz, M. (2008) "Enhanced Detection of GNSS Signals Based on Spatial Combining" MSc thesis, Department of Geomatics Engineering, University of Calgary, Canada
- Misra, P. and P. Enge (2006) "Global Positioning System", 2nd Edition, Ganga-Jamuna Press, MA
- Naguib, A. F. (1996) "Adaptive antenna for CDMA wireless network," Ph.D. dissertation, Stanford Univ., Palo Alto, CA, Aug. 1996.

- Narayanan, R. M., K. Atanassov, V. Stoiljkovic, and G. R. Kadambi (2004) "Polarization diversity measurements and analysis for antenna configurations at 1800 MHz". *IEEE Trans. on Antennas Propagat.*, 52(7): 1795-1810.
- Nielsen, J., S. K. Shanmugam, M. U. Mahfuz, and G. Lachapelle (2008) "Enhanced Detection of Weak GNSS Signals Using Spatial Combining" submitted to *International Journal of Navigation and Observation (IJNO)*, August
- Park, C. K. and K. S. Min (2005) "A study on spatial correlation characteristic of array antenna for multi antenna system," in *Proceedings of IEEE Asia-Pacific Microwave Conference (APMC 2005)*, 4-7 December 2005
- Parsons, J. D. (2000) *The Mobile Radio Propagation Channel*, John Wiley & Sons LTD, 2nd ed.
- Psiaki, M. L. (2004) "FFT-Based Acquisition of GPS L2 Civilian CM and CL Signals" in *Proceedings of the ION GNSS 2004*, Long Beach, September, Institute of Navigation.
- Stavrou, S. and S.R. Saunders (2003) "Factors Influencing Outdoor to Indoor Radio Wave Propagation", in *Proceedings of 12th International Conference on Antennas and Propagation (ICAP 2003)*, Vol. 2, 31 March - 3 April 2003 pp. 581 – 585

Rappaport, T. S. (2002) "Wireless Communications: Principles and Practice" Prentice Hall PTR, 2nd Edition

Salz J. and J. H. Winters (1994) "Effect of fading correlation on adaptive arrays in digital mobile radio," *IEEE Trans. Veh. Technol.*, vol. 43, pp. 1049–1057, Nov. 1994.

Schwartz, M., W. R. Bennett and S. Stein (1966) "Communication Systems and Techniques" McGraw-Hill, New York

Shanmugam, S. (2008) "New Enhanced Sensitivity Detection Techniques for GPS L1 C/A and Modernized Signal Acquisition" PhD Thesis, published as Report No. 20264, Department of Geomatics Engineering, The University of Calgary.

Singer, A. (1998) "A comparison of space diversity and polarization diversity receive systems for cellular and PCS systems" Available at:  
<http://www.rfsworld.com/index.php?indexVal=2&p=183>

Stavrou, S. and S.R. Saunders (2003) "Factors Influencing Outdoor to Indoor Radio Wave Propagation" in Proceedings of 12th International Conference on Antennas and Propagation (ICAP 2003), Vol. 2, 31 March - 3 April 2003 pp. 581 - 585.

Tanis, W.J., Pilato, G.J., 1993, 'Building Penetration characteristics of 880MHz and 1922 MHz Radio waves', *IEEE Trans., Vehicular Technology*, Vol.43, 206-209.

Turkmani, A. M. D., A. A. Arowojolu, P. A. Jefford and C. J. Kellett (1995) "An experimental evaluation of the performance of two-branch space diversity schemes at 1800MHz," *IEEE Trans Veh Tech*, Vol VT-44 No 2, May 1995, pp 318–326.

Watson, R., G. Lachapelle, R. Klukas, S. Turunen, S. Pietil and I. Halivaara (2006) Investigating GPS Signals Indoors with Extreme High-Sensitivity Detection Techniques. *Navigation, Institute of Navigation*, 52, 4, 199-213.

Yang, C., and A. Porter (2005) "Frequency GPS Multipath Estimation and Mitigation via Polarization Sensing Diversity: Parallel Iterative Cross Cancellation" *Proceedings of ION GNSS 2005 (San Diego, January 24-26)*, U.S. Institute of Navigation, 9 pages.

Zaheri, M., A. Broumandan, C. O'Driscoll and G. Lachapelle (2009) Enhanced GNSS Indoor Signal Detectability Using Polarization Diversity. *Proceedings of GNSS09 (Savannah, GA, 22-25 Sep, Session D1)*, The Institute of Navigation, in preparation.

"IEEE standard definitions of terms for antennas," *IEEE Trans. Antennas Propagat.*, pt. II, vol. AP-31, p. 15, Nov. 1983.